Buckling of Open Cross-Section Deployable Composite Thin Shells with Manufacturing Imperfections

Thesis by

Meital Oshrit Carmi

In Partial Fulfillment of the Requirements for the
Degree of
Doctor of Philosophy in Space Engineering

CALIFORNIA INSTITUTE OF TECHNOLOGY
Pasadena, California

2026
Defended April 29, 2026

Meital Oshrit Carmi
ORCID: 0009-0000-7837-2910

ACKNOWLEDGEMENTS

I am deeply grateful to the many people whose help and support made this success possible. I am especially grateful to the Caltech community. Caltech's friendly and collaborative environment is one of the reasons that I decided to come here for grad school, and I have grown to love our community more and more every year.

First and foremost, I would like to thank my advisor, Professor Pellegrino, for guiding and pushing me to achieve the best of my ability. I have learned so much from you over the past six years. In a way, my research trajectory was similar to a longeron's equilibrium curve. Having had relatively little research experience before starting grad school, I initially continued the work of former students. Though this led to my first conference paper, it yielded few meaningful results and was ultimately not worth including in this thesis. At this point, my work reached its first bifurcation. With your continuous advice and guidance, I learned how to develop my own research ideas in the context of the published literature. This was the stable post-buckling path for my research, where I continued on, much past the first critical buckling load, to create a body of work that is uniquely mine. Thankfully, the buckling analogy ends here, since my Ph.D. ended in success and buckling failure was never reached. Professor Pellegrino, thank you so much for your patience as I went through these learning curves. I also appreciate the high standards of work that you expect from and teach to your students, and I am grateful for the truly wonderful community of current and former students that you have fostered over the years. In addition to everything I have learned about space structures, I know that these broader skills and working relationships will benefit me far into the future.

Next, I would like to thank the members of my candidacy and defense committees for their insightful questions and comments that helped shape this work. These include Professors Nadia Lapusta, Daniel Meiron, Guruswami Ravichandran, Ares Rosakis and Angkur Shaikeea. I especially want to thank Professor Meiron for his guidance on the method for quantifying the parameters of local imperfections.

I would like to acknowledge the National Science Foundation's Graduate Research Fellowship Program and the Caltech Space Solar Power Project for providing the financial support for this research. I would also like to thank the Caltech Space Solar Power Project for providing a meaningful application for my research.

This work would not have been possible without the wonderful Aerospace Department administrators, Christine Ramirez, Jamie Meighen-Sei, Sarah Pontes, and especially Liza Bradulina and Paula Mark, who were always available to help when I needed something. I am also want to thank Petros Arakelian for helping with anything I needed in the lab.

I am especially grateful to all of the current and former members of the Space Structures Laboratory. This includes Charlie Dorn, Michael Marshall, Armanj Hasanyan, Wen Luo, Terry Gdoutos, Riccardo Augello, Uba K. Ubamanyu, Harsha Reddy, Alex Wen, Gianfranco Canales, Sahangi Dassanayake, John Pederson, Brayden Aller, Chinthaka Mallikarachchi, Divesh Soni, George Popov, Federico Benazzo, Maria Kechri, Seiji Yoshihara, Afonso Mesquita, Tara Venkatadri, Jaden Suh, Eyal Baruch, Flavia Palmeri, Charles Sommer and Alan Truong. I am so fortunate to be part of such a wonderful, tight-knit lab group, and each one of you have contributed in some way to the success of my Ph.D. Our friendship and camaraderie have made my time at Caltech so much fun.

I particularly want to thank Alan Truong, Maria Kechri, Eyal Baruch and Chinthaka Mallikarachchi for manufacturing the longerons for me, which made the experimental portions of this thesis possible. I also would like to thank Charles Sommer for writing the MATLAB script that controlled the bending machine and simultaneously collected data from the load cells and motor. Next, I want to thank Fabien Royer for showing me how to use the bending machine and teaching me how to perform buckling simulations in Abaqus, and Christophe Leclerc whose buckling research laid the foundation for mine. I am also grateful to Sage Cooley, who worked with me as a summer student on a project that helped show the viability of varying the longeron cross-sectional geometry.

I would also like to thank the members of my first-year cohort: Alex Acosta, Benjamin Bernhard, Scott Bolt, Branson Davis, Sean Devey, Meredith Hooper, Nina Mohebbi, Federico Rios Tascon, Alejandro Stefan Zavala, Michael Stramenga and Amanda Toledo Barrios. We helped each other through our first-year classes and even managed to make Zoom classes fun. Beyond our first year, I am so grateful for your continued friendship and all of the fun times we have had together. I want to thank Amanda for becoming a particularly close friend through the many classes we took together, as the only two students in our cohort whose research interests were in solid mechanics. I also want to thank Meredith and Lauren Conger for being great roommates and even better friends.

I am fortunate to have had many great mentors who encouraged me to pursue higher education. I would like to thank Professors Eckart Meiburg and Paolo Luzzatto-Fegiz at UCSB for providing me with my first undergraduate research experience. Though my research interests evolved away from fluid dynamics, my experience in your labs taught me many research fundamentals and that I enjoy doing research. I would also like to thank UCSB Chancellor Emeritus Henry Yang for his strong encouragement, which was one of the main factors that led me to pursue a Ph.D. Additionally, I would like to thank my managers during my internships at The Aerospace Corporation, Julie White, Mike Hilton and Michael Lee, who introduced me to people and taught me to ask them about their career paths, and made me realize that I want to study space structures. It was through talking to people in the Mechanical Systems Department at Aerospace that I first heard about the Pellegrino Lab, for which I will always be grateful.

Most importantly, I would like to thank my family. I want to thank my grandparents for teaching me to be strong and work hard. I strive to have even a fraction of the strength and work ethic that your generation has. I also want to thank my younger brother and best friend, Ziv, for the countless fun times we have had together. I could not have asked for a better friend to grow up with, cheer me up when I am sad and continue having good times with. I especially want to thank my parents, Aura and Avi. Thank you for introducing me to the Mars rovers, Spirit and Opportunity, for taking me to the JPL open houses and for watching countless Space Shuttle launches with me as I was growing up. Then, once I realized that I want to build spacecraft when I grew up, thank you for always encouraging me to pursue my dream. More recently, thank you for listening to the daily ups and downs of my research and classes over the past six years, for your sound advice, and for encouraging me to keep going whenever I hit a particularly low point. Words cannot capture all of the things that you have taught me and done for me, so suffice it to say, thank you and I really do appreciate everything.

ABSTRACT

Thin composite shells are increasingly being used to support large area space systems due to their high strength to mass ratio and ability to withstand tight packaging for launch and then deploy once in space. This thesis specifically focuses on long, slender composite shells (longerons) with an open cross-section consisting of two circular arc flanges bonded along one edge. They are useful components of lightweight space structures, including the Caltech Space Solar Power Project spacecraft. The flanges of the longerons are less than 100 µm thick, and these extremely thin composite shells are prone to manufacturing imperfections and local buckling. Therefore, the primary objective of this thesis is to better understand the buckling behavior of open cross-section, ultra-thin composite shells that contain manufacturing imperfections, with the goal of informing the design of future space structures that are more resistant to buckling.

The first step towards understanding a structure's imperfection sensitivity is to measure its imperfections. Thus, the thesis begins by characterizing the geometric imperfections present in experimental composite longerons. A method to measure and quantify the parameters of both local and global imperfections in thin shells is developed and applied. Results show that the longerons contain local imperfections as large as five to ten times the shell thickness, which can have serious implications for local buckling.

Once the imperfections were measured, both numerical and experimental studies are performed to study the effects of these imperfections on the buckling behavior and knockdown factor of longerons loaded in pure bending. In the numerical study, a finite element analysis is used to characterize the effect of a single imperfection, created using a simplified model based on the shape of the experimentally measured imperfections, with a wide range of geometric parameters. Then, experiments are performed to measure the buckling behavior of actual longerons, whose random manufacturing imperfections were characterized. The results of these studies show that imperfections, especially ones with large amplitudes, significantly reduce the longeron's critical buckling load and bending stiffness. Good agreement between the experimental and numerical results was achieved, particularly for higher quality longerons with a single, dominant imperfection.

Motivated by the imperfections and their detrimental effects found in the earlier parts

of the thesis, key parameters of the longeron's cross-section are varied with the goal of increasing its stability. The subtended angle of the longeron's flanges is varied in both experiments and numerical simulations of longerons loaded in bending. The results show good agreement between the experiments and simulations, with both showing a trend of increasing critical buckling load and bending stiffness with increasing flange subtended angle. Then, based on these promising results, the radius at the edge of the flange is decreased, which is shown to significant improve the longeron's stability and imperfection sensitivity without increasing its mass.

Finally, the effect of length on the buckling behavior of longerons loaded in bending is studied numerically with the goal of extending the current work to longer longerons. For lengths varying from 0.5 m to 5 m, both perfect and imperfect longerons with realistic geometric imperfections are studied. It is shown that for longer longerons, the critical buckling moment and imperfection sensitivity remain almost constant with increasing length, which is promising for future large space structures.

PUBLISHED CONTENT AND CONTRIBUTIONS

[1] Carmi, M. O., and Pellegrino, S., “Manufacturing Imperfections of Open Cross-Section Deployable Thin-Shell Composite Structures,” (Journal paper in preparation).
M.O.C. performed the shape measurements, developed the method to analyze the results, and wrote the manuscript.

[2] Carmi, M. O., and Pellegrino, S., “Stability of Open Cross-Section Composite Thin Shells in Pure Bending: Experimental and Numerical Studies of the Effects of Imperfections,” (Journal paper in preparation).
M.O.C. performed the experiments and numerical simulations, and wrote the manuscript.

[3] Carmi, M. O., and Pellegrino, S., “Effects of Varying Cross-Sectional Parameters on the Stability of Ultra-Thin Composite TRAC Longerons,” (Journal paper in preparation).
M.O.C. performed the experiments and numerical simulations, and wrote the manuscript.

[4] Carmi, M. O., and Pellegrino, S., “Effects of Length on the Stability of Open Cross-Section Composite Thin Shells,” (Journal paper in preparation).
M.O.C. performed the numerical simulations and wrote the manuscript.

[5] Carmi, M. O., and Pellegrino, S., “Manufacturing Imperfections of Open Cross-Section Deployable Thin-Shell Composite Structures,” *AIAA SciTech 2025 Forum*, 2025. https://doi.org/10.2514/6.2025-0189,
M.O.C. performed the shape measurements, developed the method to analyze the results, and wrote the manuscript.

[6] Carmi, M. O., Cooley, S., and Pellegrino, S., “Effects of Varying Geometric Design Parameters on the Stability of Deployable Thin-Shell Composite Space Structures,” *AIAA SciTech 2024 Forum*, 2024. https://doi.org/10.2514/6.2024-0606,
M.O.C. performed most of the experiments, mentored the student who manufactured some of the test samples and assisted with experiments, performed all of the numerical simulations, and wrote the manuscript.

TABLE OF CONTENTS

Chapter 1

INTRODUCTION

1.1 Buckling of Thin-Shell Structures

Thin-shell structures are widely used in engineering due to their high stiffness and load bearing capacity to mass ratio. This high structural efficiency makes thin shells ideal for use in aerospace applications where minimizing mass is critical. Examples of these applications include airplane fuselages, rockets and fuel tanks. Despite their excellent structural properties, buckling is known to be one of the main failure modes of thin-shell structures. For this reason, understanding the buckling behavior of thin-shells in order to design structures that are robust to buckling failure has been a prominent research topic since the early twentieth century.

Due to the long history of shell buckling research, there is extensive literature in the field. This section discusses a few noteworthy examples and thorough reviews can be found in the published literature [1–5]. One of the first major contributions to shell buckling research was made in 1941 by Von Karman and Tsien [6], who performed analytical calculations of cylinders under axial compression and showed that initial geometric imperfections can significantly decrease a structure's critical buckling load. In parallel, Koiter, in his 1945 doctoral thesis [7], developed a general theory for the stability of thin shells and showed that a geometric imperfection with the shape of the shell's first buckling eigenmode can substantially decrease the critical buckling load. Then, in 1950, Donnell and Wan [8] analytically calculated the critical buckling load of cylinders loaded in axial compression with an initial geometric imperfection and showed that the buckling load decreases with increasing imperfection amplitude. Similarly, in an analytical study of columns with thin-walled flanges loaded in bending, van der Neut [9] showed that the bending stiffness and critical buckling load of the flanges in compression decreases significantly as the imperfection amplitude increases. In 1962, Babcock [10] studied electroformed thin cylinders with extremely high tolerances under axial compression with carefully controlled boundary conditions. By creating a single axisymmetric imperfection on the otherwise nearly perfect cylinder, Babock experimentally validated the analytical predictions that geometric imperfections decrease a shell's critical buckling load.

Once the effect of geometric imperfections had been widely accepted, buckling research shifted towards measuring the initial imperfections in experimental shells before conducting buckling experiments. Knowing the initial imperfections present in a given shell allows the buckling results to be presented in the context of these imperfections. Additionally, the measured imperfections can be used in analytical or numerical models to account for the actual imperfections in buckling predictions and design shells that avoid buckling failure. Significant efforts to experimentally characterize geometric imperfections in closed cross-section metal shells, such as cylinders and spheres, took place in the 1960s and 1970s [4]. A notable example is the work of Arbocz and Babcock [11] who measured the manufacturing imperfections in copper cylinders before performing axial compression buckling tests. Arbocz and Babcock then used the measured imperfections in analytical buckling load calculations, which they compared to their experimental results.

A commonly used metric to quantify the effect of imperfections on a structure's stability is the knockdown factor, which is the ratio of the critical buckling load of an actual imperfect structure to the buckling load of the theoretical perfect structure [4]. For many years, the knockdown factor has been used to compute a lower bound on the critical buckling load of thin-shell structures to be used as a design criteria for designing shells that are resistant to buckling [12]. For design purposes, the knockdown factor is estimated either by experimentally measuring the critical buckling load of a large set of structures or by modeling a structure with imposed imperfections and using that to represent the actual imperfect structure.

Despite decades of study, understanding the imperfection sensitivity of thin shells and finding an accurate, yet not overly conservative, method for determining the knockdown factor is still an ongoing research area. In 2020, NASA released a revised set of buckling guidelines [12] for designing thin-walled cylinders used in space vehicles, updated from the original 1968 guidelines [13], which provide less conservative buckling load estimates by accounting for modern numerical analysis tools, materials and design methods. The updated guidelines highlight that a structure's mass can be reduced by performing high fidelity numerical simulations to obtain a less conservative knockdown factor [12], since imperfection sensitivity studies are more accurate when using the structure's actual imperfections rather than traditional eigenmode based imperfections [14, 15]. However, a structure's typical imperfections must first be characterized in order to create a high fidelity model of the structure. For this reason, imperfection characterization continues to be an important research topic. A recent example is Fan's work [16] where the imperfections in aluminum cans were measured to create a finite element model of a can with the actual imperfections.

The other prominent portion of modern research in this field is studying the effects of imperfections on the knockdown factor. For example, Gerasimidis et al. [15] studied cylindrical shells with geometric dimple imperfections under axial compression both experimentally and numerically, and their results suggest that local dimple imperfections can be used to obtain a less conservative knockdown factor for unstiffened cylinders. They also numerically studied dimple imperfections of varying amplitude and length and showed that the knockdown factor decreases significantly with increasing imperfection amplitude and is lower for axisymmetric dimple imperfections than for shorter, more localized, imperfections [15]. In another recent paper, Lee et al. [17] experimentally studied the effects of imperfections on hemispherical elastomeric shells under pressure loading, which could be manufactured with precisely controlled imperfections, and found a clear trend of decreasing knockdown factor with increasing defect amplitude, similar to the trend seen for cylinders. This work was continued by Abbasi, Derveni and Reis [18] who numerically compared the effect of a single dimple or bump on the knockdown factor of hemispherical elastomeric shells. They showed that dimples have a lower knockdown factor than bumps with the same amplitude and size, and that bumpy shells are less imperfection sensitive than dimpled shells [18]. A final example is the work of Derveni et al. [19]. These authors studied hemispherical shells with a probabilistic distribution of imperfections aiming to compute the knockdown factor by modeling shells with more realistic imposed imperfections [19].

1.2 Thin Composite Space Structures

Another application of thin shells is in large area space structures. Specifically, composite shells are increasingly being used to support large aperture space systems, such as solar arrays, antennas and solar sails, due to their high strength to mass ratio and ability to withstand tight packaging for launch and then deploy once in space [20–26]. An example of a space structure that uses lightweight composite shells is the Roll-Out Solar Array (ROSA) [27], in which two deployable composite booms are used to tension a photovoltaic blanket. Two ROSAs were used on the DART spacecraft and newer versions, iROSAs, currently provide power to the International Space Station [28]. Another recent spacecraft that used composite structures is the Advanced Composite Solar Sail System [29, 30], which uses four composite booms to hold an 80 m^2 solar sail in tension.

An application of particular interest to this work is the Caltech Space Solar Power Project (SSPP), which aims to generate solar power in space and wirelessly transmit the energy to Earth [31]. In the SSPP spacecraft, a thin-shell composite structure supports a tensioned membrane containing the photovoltaic and power transmission elements, as seen in Fig. 1.1a. A system-level study of the SSPP architecture [31] has shown that the target size for the final structure is a square with a side length of 60 m in its deployed configuration, and that bending is the main load expected for the structure.

The load-bearing elements for the SSPP structure are open cross-section, triangular rollable and collapsible (TRAC) [32, 33] longerons. The longeron cross section consists of two circular arc flanges connected by a straight web region, as shown in Fig. 1.1b, which results in the flanges being about half the thickness of the web region. This cross-section was chosen for the structural members since it has a high stiffness to mass ratio and the flanges can be flattened and coiled around a central hub, resulting in a smaller packaged volume for a given deployed bending stiffness than most traditional closed cross-section booms [32]. In the current prototype of the SSPP structure, the composite longeron's flanges are less than 100 µm thick [34, 35]. This small thickness reduces the mass of the structure and enables it to withstand the high strains of being coiled around a smaller radius hub, providing better packaging efficiency [31]. However, these ultra-thin composite shells are prone to manufacturing imperfections, which are often observed in experimental longerons, as well as local buckling. Indeed, longerons with qualitatively larger local imperfections were observed to have a lower bending stiffness and critical buckling load than longerons with smaller imperfections [36].

Though the stability and imperfection sensitivity of closed cross-section shells, like cylinders and spheres, have been extensively studied, relatively little work has been done for open cross-section shells, which have the added complexity of a weak unsupported edge where local buckling is likely to occur [36–39]. One noteworthy work on the buckling behavior of open cross-section, composite shells is that of Leclerc and Pellegrino [38], who studied longerons loaded in bending, both experimentally and numerically. They found that longerons have a stable post-buckling regime where bending moments significantly higher than the initial critical buckling moment can be achieved before buckling collapse. Leclerc and Pellegrino measured the cross-sectional parameters of experimental samples to include in the numerical model but local geometric imperfections, which are the most likely to

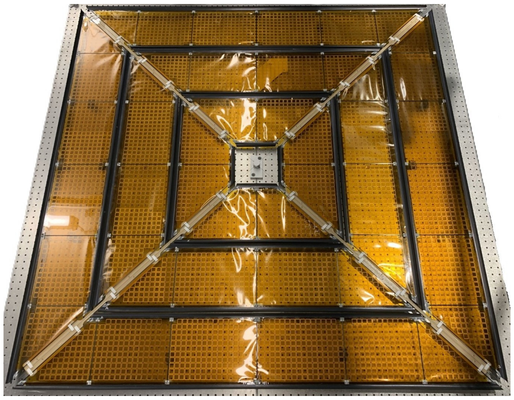

(a)

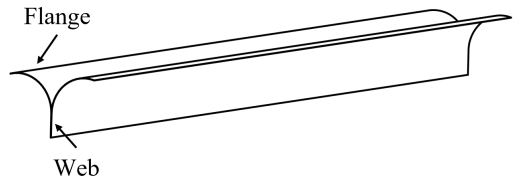

(b)

Figure 1.1: (a) SSPP prototype containing a composite structure supporting a tensioned membrane. (b) Schematic of a longeron, which is the load bearing element for the SSPP structure.

cause local buckling, were not considered. They also performed numerical buckling analyses on longerons with varying length and found that the critical buckling load is mostly constant with increasing length [38]. Another notable work is that of Royer and Pellegrino [36] who numerically studied the stability of ladder-type composite longeron strips under bending, mainly using a probing technique to compute the strip's stability landscape. A final work is that of Fathi and Royer [40] who recently performed a numerical analysis of open cross-section, cylindrical composite shells with a single Gaussian dimple loaded in bending, and quantified the imperfection's effect by probing at the location of the imperfection and measuring the buckling energy barrier. Though the probing method can provide useful insights to a shell's stability, it lacks the clarity and certainty of loading the structure to buckling and directly measuring its critical buckling load.

1.3 Problem Statement and Research Objective

While there has been work done on the stability of open cross-section composite shells and substantial literature on closed shells, before this project, little to no research had been done to measure the local geometric imperfections in open cross-section, ultra-thin composite space structures and their direct effects on these structures' buckling behavior. These extremely thin composite shells often contain large initial imperfections because manufacturing imperfections, such as defects in the laminate and thermal expansion mismatch between the composite laminate and metal mold during curing, have a greater effect on thin laminates. Additionally, many of these imperfections occur on the open cross-section's free edges, which creates the potential for interesting buckling behavior and imperfection sensitivity not present in axisymmetric closed cross-section structures, such as cylinders and spheres. This highlights the need to characterize the local imperfections in thin, open section composite shells and perform a detailed study of their buckling behavior in the context of these imperfections.

Therefore, the primary objective of this thesis is to better understand the buckling behavior of open cross-section, ultra-thin composite shells that contain manufacturing imperfections, with the goal of informing the design of future space structures that are more resistant to buckling. This work focuses on the specific case of the composite longerons used in the SSPP structures. Since the first step towards understanding a structure's imperfection sensitivity is to measure its imperfections, the first part of the thesis measures the geometric imperfections present in experimental longerons. Then, the second part of the thesis performs a detailed study of the effects of imperfections on the longerons' buckling behavior and critical buckling load. The later parts of the thesis build upon the earlier parts to investigate the effect of varying the longeron geometry, aiming to increase its stability and assess the feasibility of using longer longerons in future space structures.

1.4 Methodology and Thesis Outline

This dissertation contains six chapters including the introduction. Chapter 2 presents a characterization of the manufacturing imperfections existing in experimental composite longerons. First, a method to measure and quantify the parameters of geometric imperfections in thin shells is developed, which is challenging due to the axial twist and other large imperfections occurring in the longerons. Then, this method is applied to measure both local and global imperfections in longerons made using two different manufacturing processes, of different quality. Results show that the longerons contain significant local imperfections, as large as five to ten times the shell thickness, which can have serious implications for local buckling.

Once the imperfections were measured, both numerical and experimental studies were performed to study the effects of these imperfections on the buckling behavior and knockdown factor of longerons loaded in pure bending. These studies are presented in Chapter 3. In the numerical study, a finite element analysis is used to characterize the effect of a single imperfection on the longeron's flange, created using a simplified model based on the shape of the experimentally measured imperfections, with a wide range of geometric parameters. This study is performed numerically in order to isolate the effect of individual imperfections to see which has the greatest impact on the longeron's stability. Then, the bending and buckling behavior of experimental longerons, whose random manufacturing imperfections were characterized, is measured. The results of these studies show that imperfections, especially those with large amplitudes, significantly reduce the longerons' critical buckling load and bending stiffness. Finally, in the last part of this chapter, the experimental and numerical results are compared, and, particularly for the higher quality longerons, excellent agreement is achieved.

Motivated by the significant imperfections measured in Chapter 2 and their detrimental effects on the longeron's stability and bending stiffness seen in Chapter 3, key parameters of the longeron cross-section are varied in Chapter 4, with the goal of increasing the longeron's stability, resistance to imperfections and stiffness. In the first part of Chapter 4, the longeron's flange subtended angle is varied in both experiments and numerical simulations of longerons loaded in bending. The results show good agreement between the experiments and simulations, with both showing a trend of increasing critical buckling load and bending stiffness with increasing flange subtended angle. Then, based on these promising results, a longeron with a decreased radius at the edges of its flanges is studied numerically, with the goal of improving the longeron's stability and imperfection sensitivity without the drawback of adding material.

Next, in Chapter 5, the effect of length on the stability of longerons loaded in bending is studied numerically with the goal of extending the current work to longer longerons that can be used for future large area space structures. The longeron length is varied from 0.5 m to 5 m and the bending and buckling behavior of both perfect and imperfect longerons with realistic geometric imperfections is measured. Results show that at longer lengths, the critical buckling load remains almost constant with increasing length for both perfect and imperfect longerons.

Finally, Chapter 6 concludes the thesis by summarizing the work and discussing its main research contributions. The conclusion also presents future directions in which this research can be continued and applied to future deployable composite space structures.

Chapter 2

CHARACTERIZATION OF MANUFACTURING IMPERFECTIONS

2.1 Introduction

Thin composite shells are increasingly being used in space applications that require large, lightweight structures. Initial geometric imperfections in thin-shell structures are known to significantly decrease their critical buckling load and therefore have to be accounted for in theoretical buckling predictions [6–8]. The effect of initial imperfections is commonly quantified using the knockdown factor, which is the ratio of the buckling load of the actual imperfect structure to the buckling load of the theoretical, i.e. perfect, structure [4]. For many years, the knockdown factor has been used to compute a lower bound on the critical buckling load of thin-shell structures, to be used as a design criterion for building shells that are resistant to buckling [12]. For design purposes, the knockdown factor is estimated either by experimentally measuring the critical buckling load of a large set of structures or by numerically modeling a structure with imposed imperfections.

Despite decades of study, understanding the imperfection sensitivity of thin shells and finding an accurate, yet not overly conservative, method for determining the knockdown factor is still an ongoing research area. For example, cylindrical shells with geometric dimple imperfections loaded in axial compression were studied both experimentally and numerically as recently as 2018, and the results suggested that local dimple imperfections could be used to obtain a less conservative knockdown factor for unstiffened cylindrical shells [15]. In 2020, NASA released a revised set of buckling guidelines for designing thin-walled cylinders used in space vehicles, updated from the original 1968 guidelines, which provide less conservative buckling load estimates by accounting for modern numerical analysis tools, materials and design methods [12]. Another example is a 2023 study of hemispherical shells with a probabilistic distribution of imperfections, which aimed to compute the knockdown factor by modeling shells with more realistic imposed imperfections [19].

Imperfection sensitivity studies are more accurate when using the structure's actual imperfections rather than traditional eigenmode based imperfections [14, 15]. The updated NASA guidelines highlight that a structure's mass can be reduced by performing high fidelity numerical simulations to obtain an accurate but less conservative knockdown factor [12]. However, a structure's typical imperfections must first be characterized in order to create such a high fidelity model of the structure. Furthermore, the knockdown factor is highly dependent on the amplitude, length and aspect ratio of the imperfections in a structure [8, 15, 17], which suggests that the imperfections used to model a structure should be as close as possible to the actual imperfections.

For this reason, imperfection characterization has been an important research topic both historically and recently. Significant efforts to experimentally characterize geometric imperfections in closed cross-section metal shells, such as cylinders and spheres, took place in the 1960s and 1970s [4, 11]. A more recent example is a 2019 work where the imperfections in aluminum cans were measured to create a numerical model of a can with the actual imperfections [16]. Imperfection characterization is especially important for composite, thin-shell structures since they are particularly prone to geometric imperfections, which are introduced during the composite manufacturing process. As part of an ESA study in 2007, the geometric imperfections of ten composite cylinders were measured at DLR to obtain a statistical database of common imperfections to be used in a finite element model for probabilistic knockdown factor computations [41]. Additionally, the cross-sectional parameters and twist of open cross-section, composite booms were measured and included in numerical models of the booms [38]. However, *local* geometric imperfections in open cross-section, composite shells have not been experimentally characterized, and measuring these local imperfections is the focus of the present study.

Specifically, the study is focused on open cross-section, ultra-thin (<100 µm), composite, triangular rollable and collapsible (TRAC) [32] longerons, shown in Fig. 2.1a, which are the chosen load-bearing elements for the Caltech Space Solar Power Project (SSPP) spacecraft [31]. The TRAC longeron cross-section consists of two circular arc flanges connected by a straight web region, as seen in Fig. 2.1b. The two flanges will be refereed to as the "Front flange" and "Back flange". This design results in the thickness of the flanges being about half that of the web region, and was chosen because it increases the mass efficiency of the SSPP structure and maximizes the volume available for the functional elements. In addition, these longerons are easy to fold and coil, and can deploy by releasing their stored strain energy.

The composite longerons were manufactured in the laboratory and contained visible manufacturing imperfections. The main imperfections of interest are local radial defects in the flanges of the longerons, such as small bumps or dimples. Local imperfections are of primary concern since they are the most likely to cause local buckling, which has been found to be one of the longerons' main failure modes [38, 42]. Furthermore, since the flanges are thinner than the web region, geometric imperfections will have a greater impact on their structural performance. More global imperfections, such as the twist about the axis of the longeron and variations in the mean cross-sectional parameters, can also affect the longerons' structural behavior, and thus, are also important to measure. A thorough characterization of these imperfections will enable accurate numerical modeling of the imperfect longerons and computation of their buckling knockdown factor. At the same time, understanding the type and extent of the imperfections will help improve the manufacturing process to reduce the defects.

The chapter begins by describing the longeron manufacturing and shape measurement processes, in Section 2.2. Next, in Section 2.3, the analysis methods used to measure the longeron's axial twist and the mean web length and flange radius and subtended angle are defined. The methods used to compute the lengths, amplitudes and locations of the local imperfections are also described. Then, in Section 2.4, the results of the global and local imperfection measurements are shown and discussed. Finally, Section 2.5 concludes the chapter.

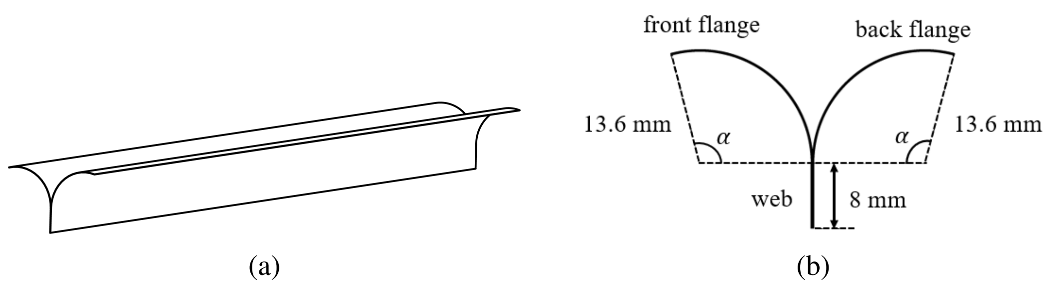

Figure 2.1: (a) TRAC longeron. (b) Longeron cross-section showing the flange subtended angle, α, and the nominal flange radius and web height.

2.2 Longeron Manufacturing and Shape Measurement

Two sets of composite longeron test samples were studied in this work. Three longerons in Set 1 were manufactured using an autoclave two-cure process and five longerons in Set 2 were made using a one-cure process. For all longerons, the flanges were 80 µm thick and had the hybrid layup $[\pm45_{GFPW}/0_{CFUD}/\pm45_{GFPW}]$. The web region had the layup $[\pm45_{GFPW}/0_{CFUD}/\pm45_{3,GFPW}/0_{CFUD}/\pm45_{GFPW}]$ and was 185 µm thick. Here CFUD represents a 30 µm thick unidirectional layer of Mitsubishi Chemical's Pyrofil MR 70 12P carbon fiber, and GFPW represents a 25 µm thick plain weave scrim glass ply. Both the carbon fiber and scrim glass plies were impregnated with North Thin Ply Technology's ThinPreg 415 resin, and the complete $[\pm 45_{GFPW}/0_{CFUD}/\pm 45_{GFPW}]$ stack was supplied by North Thin Ply Technology.

The same autoclave curing cycle was used for all cures in both manufacturing processes. First, the temperature of the autoclave was increased to 77°C at a rate of 1.67°C/min and held constant for 10 minutes. Then, the temperature was increased to 116°C and the laminate was cured for two hours before cooling to room temperature (24°C) at a rate of -1.67°C/min. During curing, the laminate was held under vacuum while the autoclave applied an external pressure of 550 kPa.

Two-Cure Process

In the first step of the two-cure manufacturing process, the three-ply preimpregnated laminates for the two flanges were placed on U-shaped aluminum molds with a radius of 12.7 mm. The two molds were vacuum bagged and cured in the same bag. After the first cure, a single ply of ±45 GFPW was added to the flat (web) region of one of the molds to provide the resin that bonded the flanges together. The two molds were then clamped together and cured for a second time to bond the flanges. After the second cure, the longeron was removed from the mold and the flanges sprang back to a nominal radius of 13.6 mm, due to residual stress from cooling at the end of the curing cycle. Finally, the flanges were temporarily flattened and cut to the arc length associated with the desired subtended angle. Excess material at the bottom of the web region was also cut to a nominal web length of 8 mm. More details about the manufacturing process are available in [38]. This two-cure process has been well characterized, and it was determined that a 12.7 mm radius mold would produce longerons with a nominal flange radius of 13.6 mm, which is desirable for flattening and coiling the longerons.

For this work, an approximately 1,500 mm long longeron was manufactured using the procedure described above. After removing the longeron from the mold, it was cut into three 500 mm long test samples. The flanges of the first shorter longeron were cut to a nominal arc length of 25 mm, which resulted in a nominal subtended angle, α, of 105°. The other two longerons were cut to arc lengths corresponding to nominal flange subtended angles of $\alpha = 120°$ and $\alpha = 135°$. These test samples were originally manufactured for bending tests studying the effects of varying the flange subtended angle, which will be described in Chapter 4. To perform these tests, the ends of each longeron were glued into acrylic plates, as shown in Fig. 2.2.

Figure 2.2: Example of longeron test sample in Set 1 glued into acrylic end plates.

One-Cure Process

The one-cure process began by cutting the laminates for the two flanges to a nominal total arc length of 36.5 mm. The two laminates were placed on the same U-shaped aluminum molds used for the two-cure process described above and aligned such that the web region was 8 mm long and the flange arc length was 28.5 mm. This arc length corresponded to a nominal flange subtended angle of 120° for the longerons manufactured using the better characterized two-cure process. To keep the material properties the same as for the two-cure longerons, a single ply of ±45 GFPW was added to the web region of one of the molds. To reduce resin flow, all exposed laminate surfaces were covered by a thin Teflon film. Then, the two molds were clamped together, vacuum bagged, and cured in an autoclave. After curing, the longeron was removed from the mold and no further processing was carried out. Five 1,700 mm long longerons were manufactured using this process.

Shape Measurement Process

The shape of the longerons was measured using a Faro Arm (Edge 14000) metrology system with a 3D laser scanner attachment (ScanArm HD), which has an accuracy of ±25 µm. The laser scanner generated a 3D point cloud of the scanned object, with a minimum point spacing of 30 µm, using the CAM2 Measure 10 software. Gravity induced deformation of the longerons was minimized during scanning by suspending them vertically from one end. The longerons in Set 1 were suspended from one of the acrylic end plates, and the longerons in Set 2 were suspended by clamping a small portion near the top of the web region, as shown in Fig. 2.3. The other end of the longerons was rested on a piece of soft foam that prevented movement during scanning while still minimizing the reaction force on the longerons.

To measure a longeron's shape, the laser scanner was slowly moved down along its length with the laser pointed at one face of the longeron. Then, the scanner was rotated around the longeron to scan it at a different angle, and the scan was repeated until a complete point cloud of the longeron was obtained. To simplify the data analysis, the front flange, back flange and web region of the longeron were scanned separately to obtain separate point clouds for each. Both the front and back faces of the web were scanned and the two point clouds were combined. Since the resulting point clouds for the two flanges and web were extremely large (about ten million points each), they were filtered using a cubic grid where a point every 0.1 mm was saved and the remaining points were deleted.

Figure 2.3: Longeron in Set 2 suspended vertically for scanning.

2.3 Analysis Methods

MATLAB scripts were used to analyze the point cloud data from the laser scanner and compute the global and local imperfections in the longerons. For the longerons in Set 1, the first 10 mm at each end of the longerons were removed to eliminate end distortions caused by the acrylic plates. This resulted in a measurement region that extended in the axial direction from z = 10 mm to z = 490 mm. For the longerons in Set 2, the first 100 mm at each end of the longerons were removed to eliminate large manufacturing defects near the ends of the mold. These defects were not an issue for the longerons in Set 1 because the regions near the ends of the mold had been cut off before the 1,500 mm long longeron was cut into the three shorter test samples. Thus, the measurement region in the axial direction for the longerons in Set 2 extended from z = 100 mm to $z = 1,600$ mm. The methods discussed in the rest of this section are the same for all test samples, in both sets.

Conversion of Flange Data to Cylindrical Coordinates

In the first step of the analysis of the flange data, the data points in the flanges of each longeron were converted from Cartesian to cylindrical coordinates. Since the z-coordinates are the same in both coordinate systems, only the x and y-coordinates were converted to r and θ-coordinates. In order to perform this conversion, the Cartesian coordinates of the central axis of each flange, which forms the z-axis of the local cylindrical coordinate system for that flange, must be determined. A simple way to find these axes for the two flanges would be to fit one cylinder to the data points in the entire front flange and another cylinder to the entire back flange. However, due to axial twist occurring in many of the longerons, fitting a single cylinder to the entire length of each flange did not provide an accurate fit. Another issue is that when a cylinder was fitted to each flange individually, the fitted cylinders were often not tangent along the flange-web boundary, which is unrealistic.

To solve these problems, instead of fitting a single cylinder to each flange, a piece-wise best fit of two 100 mm long cylinders was computed along the length of the longeron. To do this, 1 mm thick cross-sectional slices of the longeron data were extracted every 100 mm. For each slice, circles were fitted to both flanges simultaneously using a least squares minimization algorithm with a constraint that the fit circles must be tangent at the flange-web boundary, as shown in Fig. 2.4. The fit circles at adjacent slices for each flange were used to define the piece-wise cylindrical segments and the line connecting the centers of the circles was defined as the axis of the cylinder.

The objective function used to find the best-fit circles is:

$$\begin{aligned} \min f(x_{c\_f}, y_{c\_f}, R_f, x_{c\_b}, y_{c\_b}, R_b) &= \sum_{i=1}^{m}\left(\sqrt{(x_i - x_{c\_f})^2 + (y_i - y_{c\_f})^2} - R_f\right)^2 \\ &+ \sum_{j=1}^{n}\left(\sqrt{(x_j - x_{c\_b})^2 + (y_j - y_{c\_b})^2} - R_b\right)^2 \\ \text{such that } &\left|\left(x_{c\_f} + \sqrt{R_f^2 - (y_{fw} - y_{c\_f})^2}\right) - \left(x_{c\_b} - \sqrt{R_b^2 - (y_{fw} - y_{c\_b})^2}\right)\right| \leq \epsilon \end{aligned} \tag{2.1}$$

where (x_{c_f}, y_{c_f}) and (x_{c_b}, y_{c_b}) are the coordinates of the centers and R_f and R_b are the radii of the best-fit circles for the front and back flanges, respectively, (x_i, y_i) are the data points in the front flange, (x_j, y_j) are the data points in the back flange, m and n are the number of data points in the front and back flanges at a given slice,

y_{fw} is the y-coordinate of the flange-web boundary and ϵ is a small tolerance, on the order of 10^{-5} mm, to allow for numerical error in the constraint. The radii of the best-fit circles, R_f and R_b, were constant along the entire length of the longeron, though they were included as fit parameters in Eq. (2.1) because the mean radius of each flange was not initially known.

Using this method of piece-wise fit cylinders accurately results in the flange-web boundary being the center of rotation for the axial twist, so the twist is uniform throughout the longeron cross-section. Additionally, the circumferential coordinate is set to $\theta = 0°$ at flange-web boundary since the boundary is aligned with the center of the circle, which simplifies the rest of the analysis.

After the axes of the best-fit cylinders had been found, the x and y-coordinates of the center line at a given z-coordinate were subtracted from the data points at that z-coordinate to center the flange data on the z-axis of the respective fit cylinder. Then, a standard transformation from Cartesian to cylindrical coordinates was used to compute the r and θ-coordinates of each data point. Once in cylindrical coordinates, the radial coordinates of the data points were written as a function of the axial and circumferential coordinates: $r(z, \theta)$. In this form, the domain of the flange data is $z \in [10, 490]$ mm for the longerons in Set 1 and $z \in [100, 1600]$ mm for the longerons in Set 2, and $\theta \in [0°, \alpha]$ for both sets. This form of the flange data will be used for the remainder of the chapter.

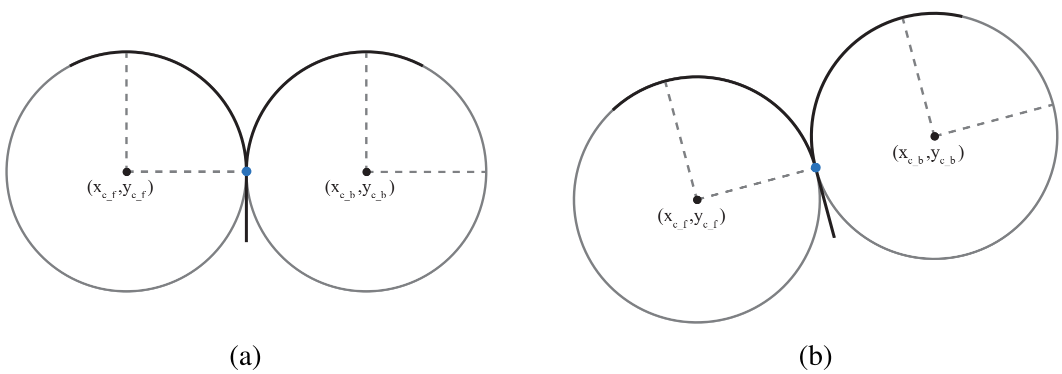

Figure 2.4: Schematic of circles fit to longeron cross-section showing a straight cross-section, (a), and a twisted cross-section, (b). The blue dot indicates the flange-web boundary.

Global Imperfection Analysis

Variations in the flange radius, subtended angle and arc length from the nominal parameters were computed by discretizing the data in each flange into 1 mm thick cross-sectional slices taken every 5 mm along the length of the longeron. The radius of each slice was computed by taking the mean of the r-coordinates of the data points in the slice. The subtended angle of each slice was determined by taking the difference between the maximum and minimum θ-coordinates of the data points in the slice. Then, the arc length of each slice was computed as the product of the radius and subtended angle of the slice. Finally, the mean radius, subtended angle and arc length of the entire flange was computed by taking the mean of the respective parameter measurements at all slices along the length of the flange.

The axial twist along the length of each longeron was determined by measuring the twist in the web region. Since the twist is uniform throughout the longerons cross-section, the web region was chosen for simplicity. The twist was computed by discretizing the data points in the web into cross-sectional slices, similar to those for the flanges, and performing a linear fit of the data points in each slice. Note that the data points in the web remained in Cartesian coordinates. Then, the twist angle with respect to the axis was computed by taking the arc tangent of the fit line. The first slice, at $z = 10$ mm for Set 1 and $z = 100$ mm for Set 2, was set to have zero twist and its twist was subtracted from that of all subsequent slices to find the relative twist at each slice. Additionally, the length of the web region at each slice was determined by computing the length of the fit line.

The twist profile of each longeron can be fitted with good accuracy to the sum of a sine and linear function:

$$\beta(z) = a \sin\left(\frac{2\pi(z-\phi)}{\lambda}\right) + cz \tag{2.2}$$

where a is the amplitude, ϕ is the phase shift and λ is the wavelength of the sine term, and c is the coefficient of the linear term. To simplify the fitting, the data points in the web were shifted in the z-direction so that the data would start at $z = 0$. This eliminated the need for a constant term in Eq. (2.2) since the twist was zero at the left end of the longeron.

Local Radial Imperfections

The next part of the analysis focused on measuring the lengths and amplitudes of individual local radial imperfections in the flanges. In this analysis, the full point cloud for each flange, with data points in the form $r(z, \theta)$, was analyzed. To filter out the measurement noise in the radial coordinates, a 2D moving window average in both the z and θ directions was used. A window size of 10 mm in the z-direction and 4° (1 mm arc length) in the θ-direction was found to achieve the best balance between reducing noise and preserving local variations. Then, for each data point in the front flange and back flange, the difference between the local radius at that point and the mean radius of the respective flange was computed. These radial deviations were displayed on a contour plot for each flange.

Two main types of local imperfections were observed. The first type are bumps and dimples which have a finite length in both the z and θ-directions and have an approximately elliptical footprint. The second type are ridges and valleys which have a finite length in the z-direction and span the entire flange in the θ-direction. The ridges and valleys have a rectangular footprint since they are uniform in the θ-direction. The difference between the two types of imperfections is shown in Fig. 2.5. To measure the lengths and amplitudes of these imperfections, an imperfection shape function was fitted to the flange data after the smoothing and subtraction of the mean radius described above.

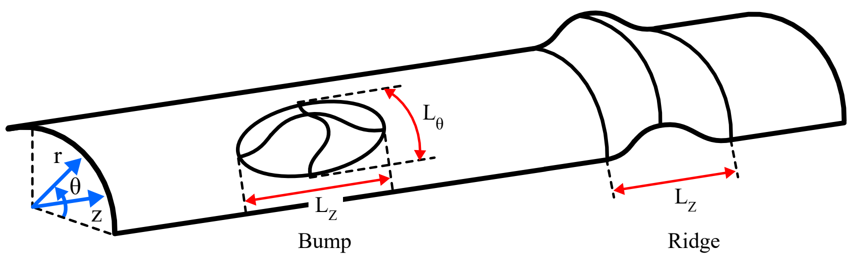

Figure 2.5: Schematic showing difference between bump and ridge.

The chosen shape function for the bumps and dimples was a single period of a cosine wave surface in both the z and θ directions:

$$\Delta r(z,\theta) = \pm 0.25A\left(\cos\left(\frac{2\pi(z-C_z)}{\lambda_z}\right)+1\right)\left(\cos\left(\frac{2\pi R(\theta-C_\theta)}{\lambda_\theta}\right)+1\right)+b$$
$$\text{for } z \in \left[C_z-\frac{\lambda_z}{2}, C_z+\frac{\lambda_z}{2}\right],\ \theta \in \left[C_\theta-\frac{\lambda_\theta}{2R}, C_\theta+\frac{\lambda_\theta}{2R}\right],\ \text{with } \Delta r = 0 \text{ otherwise} \tag{2.3}$$

where the fit parameters are A, the imperfection amplitude, C_z and C_θ, the coordinates of the center of the imperfection, λ_z and λ_θ, the length of the imperfection in the z and θ directions, respectively, and b, a shift in the radial direction that allows for global radial variations. R is the mean radius of the flange, which is used to convert $(\theta - C_\theta)$ from an angle to an arc length. The shape function is positive for bumps and negative for dimples. Shifting the cosine functions by one ensured that the maximum amplitude of the shape function would be at the center and the values at the edges would be zero. This form of shape function was chosen because its value and first derivative are both zero at the edges of its domain:

$$\begin{gathered}\Delta r(z = C_z \pm \frac{\lambda_z}{2}, \theta) = 0, \quad \Delta r(z, \theta = C_\theta \pm \frac{\lambda_\theta}{2R}) = 0, \\ \left.\frac{\partial(\Delta r)}{\partial z}\right|_{z=C_z \pm \frac{\lambda_z}{2}} = 0, \quad \left.\frac{\partial(\Delta r)}{\partial \theta}\right|_{\theta=C_\theta \pm \frac{\lambda_\theta}{2R}} = 0\end{gathered} \tag{2.4}$$

which makes the imperfection shape smooth.

A similar shape function was used for the ridge and valley imperfections. To make the shape function in Eq. (2.3) uniform in the circumferential direction, the arc length in the θ-direction was set to $\lambda_\theta = \infty$. This resulted in a single period of a cosine wave in the z-direction that spans the entire length of the flange in the θ-direction:

$$\begin{aligned}&\Delta r(z, \theta) = \pm 0.5A \left(\cos\left(\frac{2\pi(z - C_z)}{\lambda_z}\right) + 1\right) + b \\ &\text{for } z \in \left[C_z - \frac{\lambda_z}{2}, C_z + \frac{\lambda_z}{2}\right], \ \theta \in [0, \alpha], \ \text{with } \Delta r = 0 \text{ otherwise}\end{aligned} \tag{2.5}$$

The function is positive for ridges and negative for valleys.

For both main types of imperfections, the shape function was moved along the flange using a sliding rectangular window with variable size in both the z and θ-directions. The MATLAB gradient minimization algorithm, *fmincon* [43], was used to find the window size and location for which the shape function yielded the best fit to the flange data. This analysis was carried out first using Eq. (2.3), once with the positive version of the function to find the dominant bump and once with the negative version to find the dominant dimple in the flange. Then, the analysis was repeated using Eq. (2.5), with both positive and negative versions of the function to find the dominant ridge and valley, respectively.

Since the goal was to fit a shape function to the dominant imperfection of each of the four imperfection types (bump, dimple, ridge and valley), a minimum criterion was set for the amplitude parameter of $A \geq 0.2$ mm, to filter out noise. Then, to determine whether a certain region with a large radial deviation should be fit with Eq. (2.3) or Eq. (2.5), a criterion on the quality of the fit was set: $R^2 > 0.9$. Only fit functions that met these two criteria were used, and no instances were encountered where both types of shape functions met the criteria for the same region of a flange. The details of the shape function fitting algorithm are shown in Fig. 2.6.

Use $fmincon$ to find window size and location that maximize R^2:

$$\min_{W_z, W_\theta, z_i, \theta_i} f(W_z, W_\theta, z_i, \theta_i) = -R^2 \text{ such that } \begin{cases} W_{z\_min} \leq W_z \leq W_{z\_max} \\ W_{\theta\_min} \leq W_\theta \leq W_{\theta\_max} \\ z_{min} \leq z_i \leq z_{max} - W_z \\ \theta_{min} \leq \theta_i \leq \theta_{max} - W_\theta \end{cases}$$

For each (W_z, W_θ), compute (z_i, θ_i) such that window slides along data with 90% overlap

For each window:
- Use least squares fitting algorithm to compute shape function parameters with best fit
  - Apply constraint $A \geq A_{min}$
- Output R^2 value

If maximum $R^2 > 0.9$
    Output shape function parameters with optimal (W_z, W_θ) and (z_i, θ_i)
Else
    Output: "Fit quality criterion not satisfied for this imperfection type"

Repeat for positive and negative versions of both Eq. (2.3) and Eq. (2.5)

Figure 2.6: Algorithm for determining shape function parameters, where W_z and W_θ are the window size, and z_i and θ_i are the coordinates defining the window's lower bounds in the z and θ-directions, respectively.

For this work, the constraints shown in Fig. 2.6 were set as follows. The lower bound on the window size in the z-direction was set to W_{z_min} = 10 mm, and the upper bound was set to W_{z_max} = 400 mm. When fitting bumps and dimples, the lower bound on the window size in the θ-direction was set to W_{θ_min} = 10° and the upper bound was set to W_{θ_max} = 75°. When fitting ridges and valleys, the window size in the θ-direction was set to $W_\theta = \alpha$ to fit the shape function to the entire circumferential length of the flange. The lower and upper bounds of the data, z_{min} and z_{max} in the axial direction and θ_{min} and θ_{max} in the circumferential direction, were set to the domain of the flange data, defined in the previous sections. The criterion for the minimum imperfection amplitude was set to A_{min} = 0.2 mm, as discussed above. The parameters with the best fit for each imperfection type were taken to be the parameters describing the dominant imperfection of that type, when all criteria were met. This approach could be generalized to use any other shape function that would realistically fit the expected imperfections in a given structure.

2.4 Results

The geometric imperfections of two sets of longerons were measured and analyzed using the methods described in Sections 2.2 and 2.3. Set 1 consisted of three 500 mm long longerons, one with each flange subtended angle, 105°, 120° and 135°, and Set 2 consisted of five 1,700 mm long longerons all with a nominal flange subtended angle of 120°. The longerons in Set 1 are labeled using the flange subtended angle, and the longerons in Set 2 are labeled Sample 1 through 5. As discussed in Section 2.3, the longerons in Set 1 were defined over the domain $z \in [10, 490]$ mm. In Set 2, Samples 1, 3, 4 and 5 were defined over $z \in [100, 1600]$ mm. Sample 2 had a large delaminated region near the end, so an additional 100 mm were removed, resulting in a domain $z \in [100, 1500]$ mm. The results for the mean geometric parameters, axial twist, and local radial imperfections are presented in the following sections.

Global Imperfections

Tables 2.1 and 2.2 provide the mean values and standard deviations of the flange radius, subtended angle and arc length, and the web length for each longeron in Sets 1 and 2, respectively, compared to their nominal values. The variations in the mean radius were caused by variations in the amount that the flanges sprang back when removed from the molds after curing. When the mean radius is larger, it means that the flange sprang back more, and when the radius is smaller, it means that the flange sprang back less. Since the flanges were cut to a given arc length in both manufacturing processes, the flange subtended angle varies inversely to the flange radius. Thus, when the radius is larger, the subtended angle is smaller and when the radius is smaller, the subtended angle is larger. For example, both flanges of the longerons with $\alpha = 120°$ in Set 1 have a mean radius very close to 13.6 mm so the subtended angle is very close to the nominal 120°, while both flanges of Sample 3 in Set 2 have a significantly smaller radius which results in a significantly larger subtended angle.

In general, the longerons in Set 1 have a larger flange radius than the longerons in Set 2. This suggests that during the second cure, stresses are created in the flanges that cause them to spring back to a larger radius when removed from the molds. As discussed in Section 2.2, the molds were made with a smaller radius of 12.7 mm to account for the spring back in the two-cure process and produce longerons with a nominal radius of 13.6 mm. Indeed, the mean radius of the longerons in Set 1 is 13.46 mm, which is quite close to nominal. On the other hand, the mean radius of the longerons in Set 2 is 12.76 mm, which suggests that there is nearly no spring back after a single cure. The smaller than nominal radius of the longerons in Set 2 causes their subtended angle to be larger than nominal.

For all longerons in both sets, the flange arc length is within 1 mm of the nominal value and the web length is within 0.5 mm of nominal. In both cases, the error is greater than zero because when cutting material there is a bias towards longer rather than shorter. Overall, the differences between the mean and nominal values of the flange arc length and web length are quite small. This suggests that the variations in flange radius, and consequently subtended angle, within each set are caused by thermal expansion of the aluminum molds, temperature fluctuations and other conditions in the autoclave during curing that may differ between samples.

Table 2.1: Mean Values of Geometrical Parameters for Longerons in Set 1
Measured values are written with mean ± std.

Sample	Flange	Radius [mm]	Subtended angle [°]	Arc length [mm]	Web length [mm]
$\alpha = 105°$	Nominal	13.6	105	25	8
	Front	13.82 ± 0.07	104.33 ± 1.53	25.16 ± 0.10	8.28 ± 0.18
	Back	13.36 ± 0.26	109.03 ± 2.18	25.42 ± 0.11	
$\alpha = 120°$	Nominal	13.6	120	28.5	8
	Front	13.60 ± 0.17	120.75 ± 1.86	28.65 ± 0.19	8.33 ± 0.14
	Back	13.53 ± 0.12	121.71 ± 1.67	28.73 ± 0.19	
$\alpha = 135°$	Nominal	13.6	135	32	8
	Front	13.16 ± 0.19	142.15 ± 2.56	32.64 ± 0.16	8.20 ± 0.24
	Back	13.26 ± 0.11	140.67 ± 1.77	32.56 ± 0.16	

The axial twist profiles and the corresponding fit curves for the longerons in Sets 1 and 2 are compared in Fig. 2.7a and 2.7b. A positive twist is defined as counter clockwise in both figures. In Set 1, the longeron with $\alpha = 105°$ has the greatest twist with a maximum magnitude of 7.1°, and the longeron with $\alpha = 135°$ has the least twist with a maximum magnitude of 2.2°. For all three longerons in Set 1, the twist decreases near the right end, which is likely because the ends were glued into acrylic plates. Though the longerons were suspended while scanning, allowing the bottom end to hang freely, the rigid connection to the acrylic plate likely reduced the twist. In Set 2, Sample 2 has the greatest amount of twist with a maximum magnitude of 12.3°. This is a significant amount of twist that can affect the longeron's structural properties. Sample 4 has a maximum twist of 7.2°, which is about the same as the longeron with $\alpha = 105°$ from Set 1. The twist near the right end remains large for most of the longerons in Set 2 since the ends were unconstrained. There does not seem to be much correlation between the twist profiles of different longerons in the

Table 2.2: Mean Values of Geometrical Parameters for Longerons in Set 2
Measured values are written with mean ± std.

Sample	Flange	Radius [mm]	Subtended angle [°]	Arc length [mm]	Web length [mm]
	Nominal	13.6	120	28.5	8
1	Front	12.91 ± 0.40	128.54 ± 4.95	28.93 ± 0.52	8.35 ± 0.16
	Back	13.16 ± 0.54	125.57 ± 4.79	28.81 ± 0.47	
2	Front	13.18 ± 0.43	125.38 ± 4.26	28.81 ± 0.34	8.35 ± 0.15
	Back	13.38 ± 0.40	123.99 ± 3.53	28.93 ± 0.28	
3	Front	12.07 ± 0.39	137.22 ± 4.35	28.87 ± 0.45	8.38 ± 0.19
	Back	12.23 ± 0.46	135.37 ± 4.99	28.86 ± 0.38	
4	Front	13.17 ± 0.63	125.85 ± 6.11	28.87 ± 0.31	8.39 ± 0.15
	Back	12.21 ± 0.44	134.76 ± 5.37	28.67 ± 0.27	
5	Front	12.66 ± 0.47	129.69 ± 4.21	28.63 ± 0.48	8.41 ± 0.21
	Back	12.71 ± 0.44	131.28 ± 4.89	29.08 ± 0.38	
	Set 2 Mean	12.76 ± 0.64	129.83 ± 6.53	28.84 ± 0.42	8.37 ± 0.17

same set or between the two sets. This fairly random twist distribution suggests that the twist is either caused by thermal gradients during curing that vary between different curing cycles or by defects in the composite prepregs used to manufacture the longerons, such as nonuniform fiber distribution and twist in the fibers, or a combination of both.

Table 2.3 shows the values of the fit parameters and the R^2 value for the curves fit to the twist profiles, defined by Eq. (2.2). In general, the sum of sine and linear functions fits the twist profiles quite well with an R^2 value greater than 0.9 in all but one case. This exception is the longeron with $\alpha = 135°$ in Set 1 which has an R^2 value of 0.82. As seen in Table 2.3, there is a wide spread in the values of the fit parameters describing the twist, with no clear trend in the values for the longerons in each set or between sets. Due to the lack of a trend between the sets, the mean of the parameters (shown in the last line of Table 2.3) was taken over all longerons in both sets. Consistent with the wide spread in the fit parameters, the standard deviations are high for all four parameters. For this reason, using the mean values to model the twist in future simulations of imperfect longerons, manufactured using the current methods, would result in a non-conservative estimate. The best recommendation, based on the current results, would be to use the parameters for the worst case twist of Sample 2 in Set 2 to model the twist in these longerons.

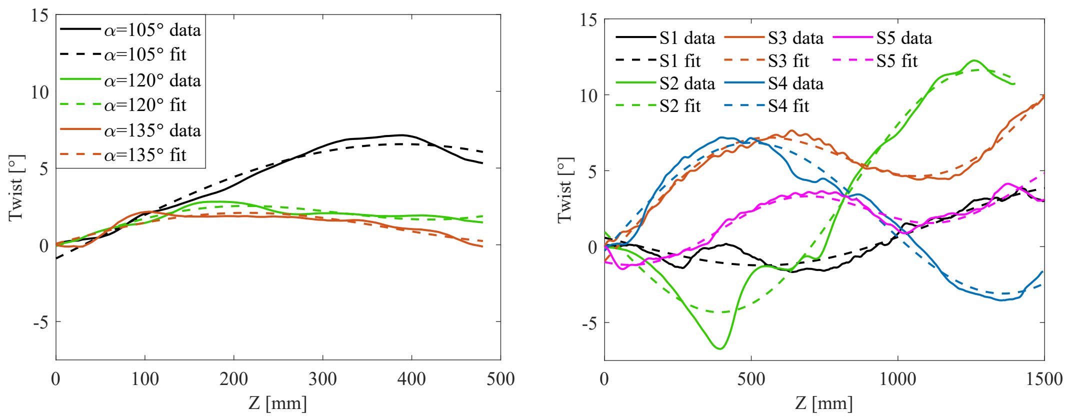

(a) Set 1 (b) Set 2

Figure 2.7: Axial twist profiles along the length of the longerons and the corresponding fit curves.

Table 2.3: Parameters of Twist Profile Fit Curves

Set	Sample	a [°]	λ [mm]	ϕ [mm]	c [°/mm]	R^2
1	$\alpha = 105°$	6.50	1,429.1	31.26	1.44×10^{-4}	0.97
	$\alpha = 120°$	1.30	621.1	6.81	6.58×10^{-3}	0.90
	$\alpha = 135°$	1.51	769.2	-6.24	2.84×10^{-3}	0.82
2	1	2.00	2,040.2	1,116.77	1.34×10^{-3}	0.90
	2	6.14	1,593.2	836.56	4.37×10^{-3}	0.98
	3	3.56	1,496.4	64.51	7.27×10^{-3}	0.97
	4	5.86	1,832.8	13.61	2.01×10^{-3}	0.97
	5	1.51	1,021.7	390.18	2.70×10^{-3}	0.92
	Mean ± std	3.55 ± 2.28	1,350.5 ± 503.2	306.68 ± 439.52	3.41×10^{-3} ± 2.50×10^{-3}	

Local Imperfections

For brevity, throughout this section detailed results will only be shown for two representative examples from each set. However, the discussion will include comments about all samples and the mean amplitudes and lengths of the dominant imperfections of all samples will be shown. Detailed results for all samples are included in Appendix A.1.

The local radial deviations from the mean flange radius for representative example flanges from each set are shown in Fig. 2.8. The axial coordinate, measured from the left end of each longeron, is plotted on the horizontal axis, the circumferential coordinate is plotted on the vertical axis, with the edge of the flange at the top of the plot, and the contours show the radial deviations, or imperfection amplitudes. Positive radial deviations indicate a larger local radius, meaning a bump or ridge, and negative deviations indicate a smaller local radius, a dimple or valley, on the flange. For example, the orange region in the top left of Fig. 2.8a indicates a local bump, the blue region in the top right of Fig. 2.8b indicates a local dimple, the red region in the middle of Fig. 2.8d is a ridge, and the blue region in the left of Fig. 2.8d is a valley. The uneven shape at the top of the plots is caused by variations in the flange subtended angle. Note that in regions where the subtended angle is larger (less white space at the top of the plots), the radial deviations are negative since the flange radius varies inversely to the subtended angle. Likewise, in regions where the subtended angle is smaller, the radial deviations are positive.

In general, the longerons in Set 1 have smaller amplitude imperfections than the longerons in Set 2. Note that for this reason, the scale of the contours in Fig. 2.8a and 2.8b is smaller than the scale of Fig. 2.8c and 2.8d. The main imperfections seen in Set 1 are bumps and dimples that occur at the edge of the flange. On the other hand, ridges and valleys are more common in Set 2, as well as bumps at the edge of the flange. Additionally, dimples near the flange-web boundary, such as the blue and green regions along the bottom of Fig. 2.8c, occur in several of the samples in Set 2. These dimples are caused by delaminated regions near the flange-web boundary that are introduced during the one-cure process. In the two-cure process, curing the flanges individually before bonding them likely prevents these dimples.

Next, a shape function was fitted to the dominant bump, dimple, ridge and valley in the front and back flanges of each longeron, using the method described in Section 2.3. The shape functions overlaid on the deviations of the flange data from the mean radius for the example flanges are shown in Fig. 2.9. Note that for most flanges the minimum amplitude and fit quality criteria were not satisfied for all four types of imperfections. For example, only one flange in Set 1 had a ridge and none of the flanges in Set 1 had a valley. Also, note that the shape function does not capture the sharper peaks and troughs of some of the imperfections, for example the sharp peak

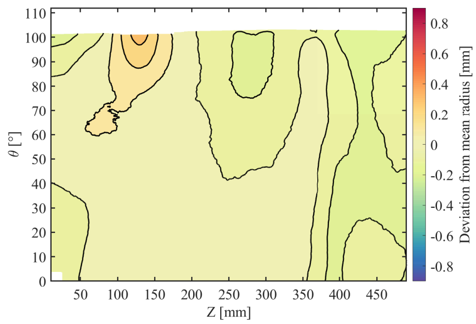

(a) Front flange, Set 1, $\alpha = 105°$

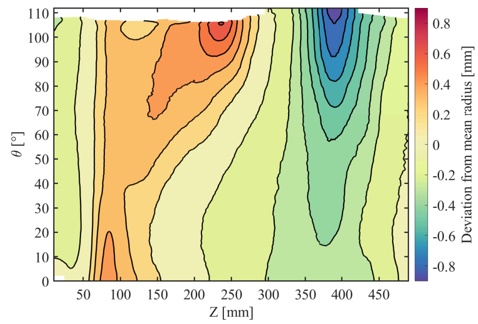

(b) Back flange, Set 1, $\alpha = 105°$

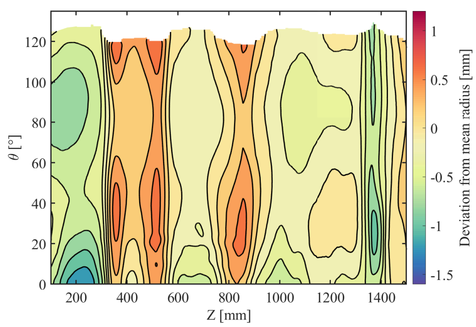

(c) Back flange, Set 2, Sample 2

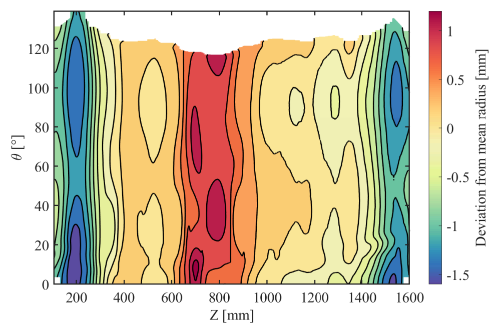

(d) Front flange, Set 2, Sample 4

Figure 2.8: Radial imperfections for example flanges. Positive deviations from the mean radius indicate outward imperfections (bumps or ridges) and negative deviations indicate inward imperfections (dimples or valleys).

of the bump in Fig. 2.9b. This results in the amplitude of the shape function being smaller than the actual amplitude of the imperfection in these cases. However, in general the fit of the shape function is quite good and it gives a good quantitative measurement of the amplitude and length of the local imperfections.

Table 2.4 provides the fit parameters of the shape function in Eq. (2.3) and the R^2 value of the fit for the dominant imperfections of the example flanges. For all flanges, the R^2 value is above 0.9 indicating that the fit function is a relatively good fit to the data. Many of the dominant bumps and dimples occurred on the edge of the flange, i.e. $C_\theta = \theta_e$, where θ_e is the θ-coordinate at the edge of the flange. When this was the case, the maximum amplitude occurred at θ_e, and only half the length of the fit function in the circumferential direction was actually on the flange, resulting in a semi-elliptical imperfection region. For this reason, the window size that resulted in the highest R^2 value was approximately λ_z by $\frac{\lambda_\theta}{2R}$, for most dominant bumps and dimples. The window was centered on (C_z, C_θ), so the resulting bounds of the window were $[C_z - \frac{\lambda_z}{2}, C_z + \frac{\lambda_z}{2}]$ and $[C_\theta - \frac{\lambda_\theta}{2R}, C_\theta]$. For most ridges and valleys

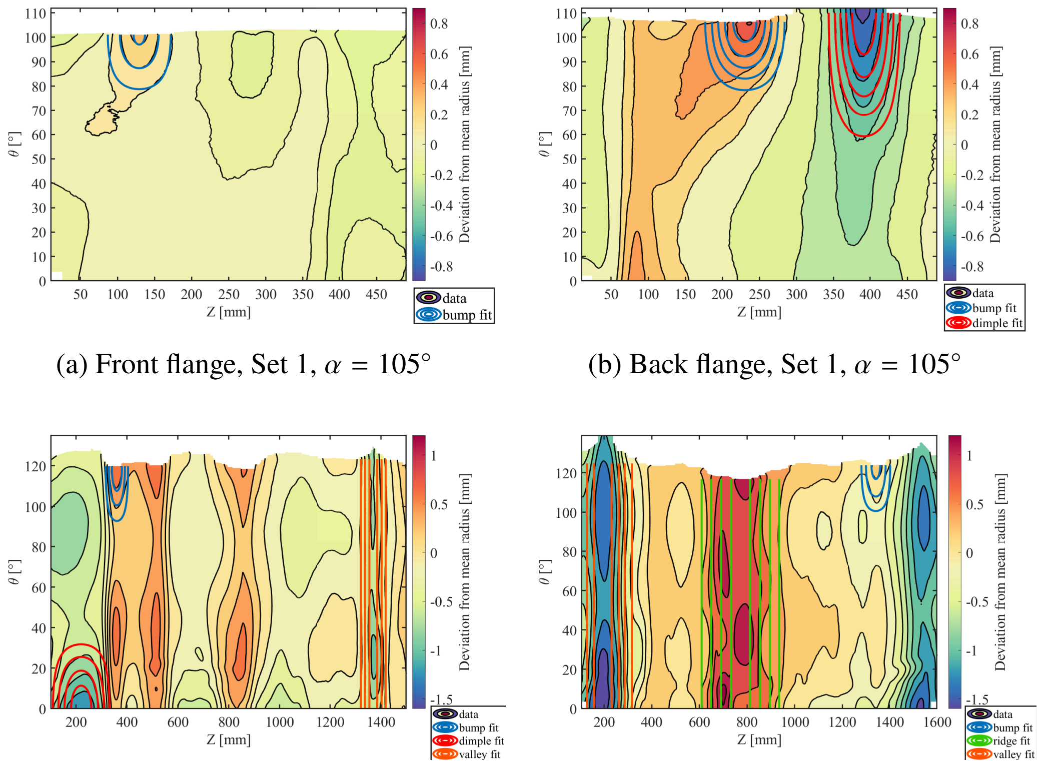

(a) Front flange, Set 1, $\alpha = 105°$

(b) Back flange, Set 1, $\alpha = 105°$

(c) Back flange, Set 2, Sample 2

(d) Front flange, Set 2, Sample 4

Figure 2.9: Shape functions fitted to dominant imperfections for example flanges.

the bounds of the window that gave the highest R^2 value were $[C_z - \frac{\lambda_z}{2}, C_z + \frac{\lambda_z}{2}]$ and $[0, \theta_e]$. There were a few imperfections that were exceptions to this, including the dimples near the flange-web boundary in Set 2 and imperfections near the edge of the domain in the axial direction. Another exception was the case where λ_z and/or λ_θ were significantly larger than the window lengths that gave the highest R^2 value, but the shape function remained fully within the domain of the data. In this case, the window lengths were a better approximation of the imperfection length than the shape function parameters. Therefore, the window lengths were used to approximate the imperfection lengths, and alternate length variables, L_z and L_θ, were defined to account for these modifications. In all other cases, L_z and L_θ were equal to λ_z and λ_θ, respectively. The bounds of the windows that gave the best fit for all of these exceptions are listed in the Appendix in Table A.3.

The mean values and standard deviations of the amplitudes and lengths in the z and θ-directions of the dominant imperfections for the flanges in each set and overall for all flanges are shown in Table 2.5. The imperfection amplitudes and lengths for the individual flanges are listed in the Appendix in Tables A.4 and A.5.

Key results of this study are as follows. The mean imperfection amplitude for the flanges in Set 1 for all relevant imperfection types is about 4 times the flange thickness. For the flanges in Set 2, the mean imperfection amplitude is nearly 8 times the flange thickness for bumps and dimples, nearly 7 times the thickness for ridges, and about 10 times the thickness for valleys. The overall mean imperfection amplitude is 6 to 7 times the flange thickness for bumps, dimples and ridges, and about 10 times the thickness for valleys. These are significant imperfections that can impact the longerons' stability. The mean imperfection lengths are fairly similar between the flanges in Sets 1 and 2. The bumps have the smallest footprint, with a mean L_z of about 130 mm and a mean L_θ of about 18 mm. The ridges and valleys are the longest in the axial direction, with a mean L_z of about 240 mm. These lengths include the nearly tangential tails of the cosine shape functions, which is one reason why they are so long.

Table 2.4: Parameters of Shape Functions for Dominant Imperfections

Set	Sample	Type	A [mm]	λ_z [mm]	λ_θ [mm]	b [mm]	C_z [mm]	C_θ [°]	R^2
1	Front flange, $\alpha = 105°$	Bump	0.25	118.4	15.05	0.05	129.3	101.1	0.98
	Back flange, $\alpha = 105°$	Bump	0.60	159.3	19.40	0.05	230.3	106.3	0.99
		Dimple	0.58	132.7	32.41	-0.20	391.5	112.0	0.99
2	Back flange, Sample 2	Bump	0.67	119.2	16.94	0.10	360.0	119.8	0.91
		Dimple	0.79	288.9	19.28	-0.35	219.7	0	0.93
		Valley	0.58	136.5	∞	-0.09	1,370.4	N/A	0.95
	Front flange, Sample 4	Bump	0.44	159.9	14.14	-0.18	1,343.0	123.9	0.91
		Ridge	0.66	328.0	∞	0.37	772.3	N/A	0.92
		Valley	1.20	315.2	∞	-0.06	194.24	N/A	0.95

Table 2.5: Mean Amplitudes and Lengths of Dominant Imperfections

	Bump			**Dimple**			**Ridge**		**Valley**	
	A [mm]	L_z [mm]	L_θ [mm]	A [mm]	L_z [mm]	L_θ [mm]	A [mm]	L_z [mm]	A [mm]	L_z [mm]
Set 1 Mean	0.43 ±0.25	138.9 ±28.9	17.22 ±1.54	0.41 ±0.15	186.9 ±60.6	22.80 ±4.42	0.46 ± 0	212.7 ± 0	N/A	N/A
Set 2 Mean	0.77 ±0.32	125.1 ±20.6	17.78 ±1.78	0.78 ±0.23	163.8 ±76.6	18.42 ±1.85	0.67 ±0.11	246.4 ±75.5	1.03 ±0.23	243.5 ±68.4
Overall Mean	0.70 ±0.33	127.9 ±21.4	17.67 ±1.66	0.58 ±0.26	176.6 ±65.7	20.85 ±3.33	0.65 ±0.13	242.2 ±80.4	1.03 ±0.23	243.5 ±68.4

2.5 Conclusion

This work has presented an analysis method for characterizing the rich landscape of geometric imperfections present in open cross-section, thin-shell composite structures. The method was used to measure the imperfections of a total of eight longeron test samples made using two different manufacturing processes, revealing the types of defects most commonly introduced during manufacturing. This method could also be generalized to characterize the imperfections of other thin-shell structures with a circle-based cross section.

Global imperfections such as variations in the longerons' geometric parameters and axial twist were measured. The differences between the mean and nominal values of the flange arc length and web length were found to be small for longerons in both sets, suggesting that the material was cut accurately in both manufacturing processes. The flange radius of the longerons in Set 1 was found to be larger than the radius of the longerons in Set 2, though both were manufactured using the same mold. This suggests that the two-cure process introduces stresses in the flanges that cause them to spring back to a larger radius when removed from the molds. Within each set, the flange radius was fairly consistent, suggesting that each manufacturing process is repeatable from this perspective.

Significant axial twist was found in the longerons in both sets. The twist profiles of different longerons appear to be fairly random, with no clear trend in the profiles between longerons in different sets. Additionally, the standard deviations of the fit parameters of curves fit to the twist profiles are high. This suggests that the twist is not affected by the number of-cures and is instead caused by defects in the composite prepregs used to manufacture the longerons, such as nonuniform fiber distribution and twist in the fibers, or thermal gradients in the autoclave that vary between curing cycles.

Four types of local radial imperfections in the longerons' flanges were identified. The amplitude and length of the dominant bump, dimple, ridge and valley in both flanges of each longeron were computed, for imperfection types that met the requirements $A \geq 0.2$ mm and $R^2 > 0.9$. The overall mean imperfection amplitude ranged from 6 to 10 times the flange thickness. The mean imperfection length ranged from about 130 mm to 240 mm in the z-direction, and 18 mm to 21 mm in the θ-direction for bumps and dimples. These are significant geometric deviations that can create weak spots where local buckling and other structural failures are likely to occur, and it is important to know that these imperfections exist in the manufactured longerons.

Notably, all of the measured local imperfections were quite different from the wave-like eigenmode shapes that are commonly used to model imperfections.

For all imperfection types, the mean imperfection amplitude of the longerons in Set 1, which were manufactured using a two-cure process, is significantly smaller than the amplitude of the longerons in Set 2, which were manufactured using a one-cure process. Thus, the conclusion is that curing the flanges individually before bonding them together reduces the local imperfections. Therefore, the two-cure process should be the preferred choice for future longerons. Another option could be to use higher quality composite molds that have a lower coefficient of thermal expansion, since it is suspected that thermal expansion of the mold during curing introduces stresses that cause the local imperfections.

The results from this study can be used to create a detailed numerical model of a longeron with the measured geometric imperfections in order to compute an accurate buckling knockdown factor of the imperfect longerons. This will give a quantitative measure of the effect of the imperfections on the longerons' stability. Additionally, a numerical model can be used to compute the knockdown factor of a longeron with each type of imperfection individually, to determine which imperfection is most detrimental to the structure. Knowing which type of imperfection has the greatest effect on stability, efforts can be made to mitigate this type of imperfection during manufacturing and future imperfection measurements can focus on this imperfection.

Chapter 3

EXPERIMENTS AND SIMULATIONS ON IMPERFECT SHELLS IN BENDING

3.1 Introduction

Designing thin-shell structures that are robust to buckling failure, yet not over designed, is important for many engineering applications, including large, lightweight space structures. Achieving this requires an accurate method for predicting a structure's critical buckling load, which is know to decrease if a structure contains initial geometric imperfections [6, 7]. A commonly used metric to quantify the effect of imperfections on a structure's stability is the knockdown factor, which is the ratio of the critical buckling load of the actual imperfect structure to the buckling load of the theoretical perfect structure [4]. Due to the complex imperfection sensitivity of thin-shell structures, understanding the effect of imperfections on a structure's buckling behavior has historically been, and continues to be, an important research area.

In an early study of the effects of imperfections, Donnell and Wan [8] analytically calculated the critical buckling load of cylinders loaded in axial compression with an initial geometric imperfection and showed that the buckling load decreases with increasing imperfection amplitude. Similarly, in an analytical study of columns with thin-walled flanges loaded in bending, van der Neut [9] showed that the bending stiffness and critical buckling load of the flanges in compression decreases significantly as the imperfection amplitude increases. Both studies also showed that the peak in the load-displacement (or stress-strain) curve that occurs at the bifurcation point becomes less sharp with increasing imperfection amplitude, until a certain large amplitude is reached where a bifurcation point no longer exists and the curve increases monotonically [8, 9].

A comprehensive study of imperfection sensitivity is presented in Chapter 6 of Wullschleger's 2006 PhD thesis [44] where he used finite element analyses to study the effect of a single dent or bulge on the stability of thin-walled isotropic cylinders and laminated CFRP cylinders under axial compression. Wullschleger varied the initial amplitude, axial length and circumferential width of the imperfection and found that the critical buckling load decreased with increasing imperfection amplitude. He also found that the critical buckling load decreased with increasing imperfection length and width for large amplitude dents, with ring-shaped dents having the lowest buckling load. In contrast, for small amplitude dents, the buckling load increased slightly with increasing imperfection size. Wullschleger observed that for relatively low amplitude dents the cylinder experienced local buckling but restabilized and could support further axial compression until total cylinder collapse was reached. In contrast, cylinders with larger amplitude dents did not experience local buckling, since the dent gradually deepened and flattened up to total cylinder collapse, so the sudden snap of local buckling was avoided. He also showed that dents reduced the critical buckling load more than bulges of the same amplitude and size. For composite cylinders, Wullschleger showed that although the value of the critical buckling load differed for different stacking sequences, the trends with varying imperfection amplitude and size were the same as for the isotropic cylinders. However, Wullschleger lacked experimental results to validate his numerical findings and his finite element analysis was fairly rudimentary due to computing limitations.

More recently, Gerasimidis et al. [15] numerically studied cylinders under axial compression with dimple imperfections of varying amplitude and length. They showed that the knockdown factor decreased significantly with increasing imperfection amplitude, and that the knockdown factor was lower for axisymmetric dimple imperfections that spanned the entire cylinder in the circumferential direction and increased as the imperfection became shorter and more localized [15]. In another recent paper, Lee et al. [17] experimentally studied the imperfection sensitivity of hemispherical elastomeric shells, which could be manufactured with precisely controlled imperfections. Lee et al. studied such shells with a single dimple under pressure loading and found a clear trend of decreasing knockdown factor with increasing defect amplitude in both experimental and numerical results, similar to the trend seen for cylinders. This work was continued by Abbasi, Derveni and Reis [18] who numerically compared the effect of a single dimple or bump on the knockdown factor of hemispherical elastomeric shells. They found that the knockdown factor decreased with increasing imperfection amplitude for both dimples and bumps, consistent with previous literature. Abbasi, Derveni and Reis also showed that the dimples had a lower knockdown factor than bumps with the same amplitude and size, and that bumpy shells were less imperfection sensitive than dimpled shells. Additionally, for dimples the shell with the widest dimple had the lowest knockdown factor, while for bumpy shells the knockdown factor was lowest at intermediate widths [18].

Studying imperfection sensitivity is especially important for very thin, open cross-section, composite structures since manufacturing these thin composites is challenging and often results in initial geometric imperfections. One notable work is that of Leclerc and Pellegrino [38], who measured the buckling behavior and critical buckling load of open cross-section, composite longerons loaded in bending. In both experiments and numerical simulations, Leclerc and Pellegrino showed that the longerons have a stable post-buckling regime. Numerically, they performed both linear and non-linear eigenvalue computations, as well as a post-buckling analysis using an arc-length solver. Additionally, global imperfections measured in the experimental longerons, such as variations in the cross-sectional parameters and axial twist, were included in their numerical model [38], but local imperfections were not considered. Another work is that of Fathi and Royer [40], who recently performed a numerical analysis of open cross-section, cylindrical composite shells with a single Gaussian dimple loaded in bending, and quantified the imperfection's effect by probing at the location of the imperfection and measuring the buckling energy barrier.

While there has been work on the stability of open cross-section composite shells, as discussed above, and extensive literature regarding the effects of imperfections on the stability of closed cross-section thin-shell structures, the effects of local imperfections on the buckling behavior and knockdown factor of open cross-section, ultra-thin, composite structures has not been studied. Open cross-section structures have the added complexity of a weak unsupported edge, which creates the potential for interesting buckling behavior not present in axisymmetric closed cross-section structures, such as cylinders and spheres. Furthermore, open cross-section composite structures with qualitatively greater local imperfections were observed to have a lower bending stiffness and critical buckling load than structures with smaller imperfections [36], highlighting the need for a detailed study of the imperfection sensitivity of such structures.

The present study is focused on open cross-section, ultra-thin, composite, triangular rollable and collapsible (TRAC) [32] longerons loaded in pure bending. The TRAC longeron cross-section is formed by two circular arc flanges connected by a straight web region, which results in the flanges being about half the thickness of the web region. Longerons were chosen for this study because they are the load-bearing elements for the Caltech Space Solar Power Project (SSPP) spacecraft [31], which uses composite longerons since they have a high stiffness to mass ratio, efficient packaging and can deploy using their stored strain energy. Bending is the main load expected for the SSPP spacecraft, therefore, bending was chosen for the loading in this study.

The flanges of the longerons studied in this work are less than 100 µm thick. These very thin composite shells are very prone to manufacturing imperfections which are often observed in experimental longerons. The amplitude of these imperfections can be fairly large, often five to ten times the shell thickness, due to the very thin, high-strain composite material.

The first part of this chapter uses a finite element analysis to characterize the effect on the longeron's buckling behavior of a single imperfection on the longeron's flange with varying parameters. The numerical model is motivated by experimental longerons and an experimental setup so that experimental and numerical results can later be compared. This part of the work is performed numerically because numerically it is possible to isolate the effect of individual imperfections to see what has the greatest impact on the longeron's stability. Knowing which imperfections are most detrimental will enable a focus on this type of imperfection when predicting the buckling load of longerons used in structural applications. Additionally, this knowledge can inform the design of more robust structures by modifying the longeron's design to make it more resistant to these most detrimental imperfections.

In the second part of the chapter, experiments are performed to study the buckling behavior of actual structures. Longerons manufactured using two different manufacturing processes, whose imperfections were previously characterized, are tested. Since these are actual functional structures with random manufacturing imperfections, using structures made with a high quality manufacturing process as well as ones made with a lower quality manufacturing process that introduces larger imperfections enables an experimental study of the effects of imperfections. In both the numerical and experimental studies, the knockdown factor is used to quantify the effect of imperfections on the longerons' stability. Since the longerons are loaded in bending, the critical buckling bending moment of an imperfect longeron is compared to that of the numerical perfect longeron to compute the knockdown factor in all cases.

The chapter begins by describing the types of imperfections commonly observed in the experimental longerons and the experimental setup used to load the longerons in pure bending and measure the critical buckling load in Section 3.2. Next, the numerical analysis methods used to model longerons with different imperfection types, amplitudes, lengths and circumferential locations are described in Section 3.3. Then, in Section 3.4, the experimental test structures and methods are presented. The numerical results are shown in Section 3.5 and the experimental results are shown in Section 3.6. Finally, the experimental and numerical results are compared in Section 3.7 and the chapter is concluded in Section 3.8.

3.2 Longerons Under Pure Bending

The longerons used in this study had flanges that were 80 μm thick and a web region that was 185 μm thick. They had a nominal axial length of 500 mm, web length of 8 mm, and flange radius of 13.6 mm and subtended angle of 120°, which resulted in a flange arc length of 28.5 mm. The numerical longerons had this geometry exactly, and variations to these parameters found in the experimental longerons will be discussed in a later section.

Basic Imperfections

Initial geometric imperfections are often introduced during the composite manufacturing process. The primary concern are local imperfections since they are the most likely to cause local buckling, which is one of the longerons' main failure modes [38]. Imperfections have a greater effect on the longeron's flanges since the flanges are thinner than the web region. Furthermore, when the longerons are loaded in bending about the vertical axis, the greatest bending moment occurs near the edges of the flange and there is zero moment in the web region. Therefore, local imperfections in the flanges will have the greatest effect on the longeron's buckling behavior and, thus, will be focused on in this chapter.

Two main types of local imperfections have been observed in the flanges of experimental longerons. The first type are local bumps and dimples. Bumps are outward imperfections that increase the flange radius in the local region of the defect, and dimples are inward imperfections that decrease the local flange radius. Both bumps and dimples have a finite length in both the axial and circumferential directions which results in an approximately elliptical footprint. The second type of imperfections are ridges and valleys. Ridges are outward imperfections, similar to bumps, while valleys are inward imperfections, similar to dimples. The main difference is that ridges and valleys have a finite length in the axial direction but span the entire width of the flange in the circumferential direction, as shown in Fig. 3.2. This results in ridges and valleys having a rectangular footprint since they are uniform in the circumferential direction.

Test Setup, Loading and Boundary Conditions

Since longerons are extremely sensitive to loading and boundary conditions, it is important to apply a well characterized load and minimize the effects of all other loads. Experimentally, this is achieved by using a specially designed bending machine that applies a rotation to load a test structure in as close as possible to pure bending about the vertical axis [42, 45]. The bending machine constrains only one of each degree of freedom to ensure that there is no self stress in the test sample, while a motor rotates one end of the sample to apply the bending. Air bearings, sliders and counterweights allow the sample to move freely in the degrees of freedom that are not constrained.

As shown in Fig. 3.1, the left end of the test sample (End 1) is actuated by a Harmonic Drive FHA-8C DC motor which applies a rotation about the vertical, y-axis. The applied rotation is measured by an incremental encoder with a resolution of 4.5×10^{-4} degrees. End 1 is held fixed in translation along the y-axis, and in both translation and rotation about the z-axis. An air bearing on a rail running along the x-axis allows End 1 to freely translate along and rotate about the x-axis. The right end of the test sample (End 2) is held fixed in both translation and rotation about the x-axis, and in rotation about the y-axis. A vertical slider on End 2 allows free translation along the y-axis, and an air bearing on a rail along the axial direction allows free translation and rotation about the z-axis. Forces and moments in all three directions are measured by load cells at each end of the test sample to record the bending moment about the vertical axis and verify that all of the other forces and moments are negligibly small. The ATI Mini40 load cells have a resolution of 1/100 N for the three force components and a resolution of 1/4000 Nm for the three moment components.

In order to mount an experimental longeron onto the bending machine, the ends of the longeron are rigidly glued into acrylic plates that are 50 mm wide, 90.5 mm tall and 6 mm thick. The acrylic plate on End 1 of the longeron is screwed onto a stiff aluminum plate which hangs down on the left side of the bending machine, and the acrylic plate on End 2 of the longeron is screwed onto the vertical slider on the right side of the bending machine.

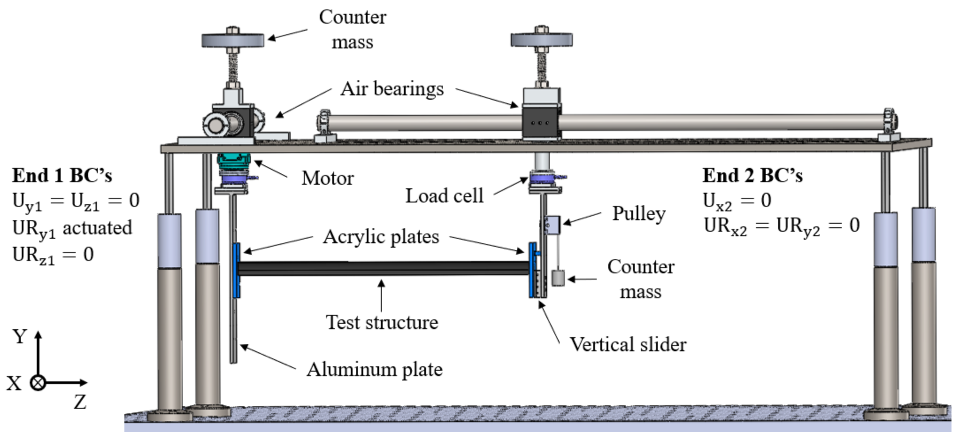

(a)

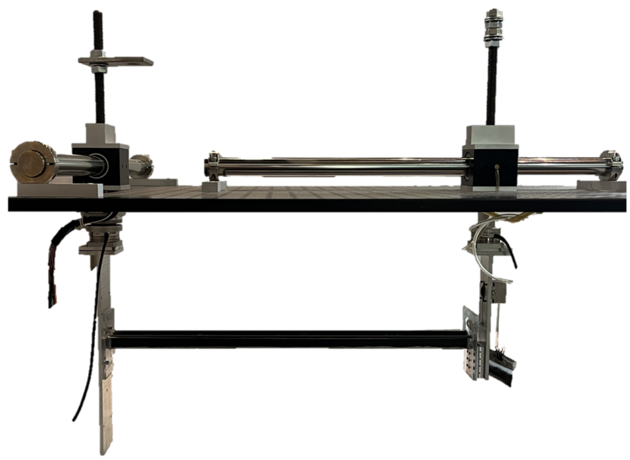

(b)

Figure 3.1: (a) CAD model of the bending machine and the boundary conditions at each end of the test structure. (b) Experimental bending machine.

3.3 Numerical Analysis Methods

The benefits of performing a numerical analysis are that a perfect longeron, without the imperfections observed in the experimental longerons, can be simulated and its bending stiffness and critical buckling load can be measured and used as a baseline when computing the knockdown factor. Furthermore, in a numerical analysis, different kinds of imperfections can be isolated, so the effects of each imperfection can be studied and it can be determined which imperfection is most detrimental to the longeron’s stability.

The goal of the numerical model was to simulate the experimental longerons and bending setup as closely as possible so that the experimental and numerical results could be compared. This was achieved by creating a model of a longeron and the bending machine boundary conditions using the Abaqus 2024 commercial finite element software. A key element required to make the numerical results similar to the experimental ones was to model the compliance of the bending machine. As described in Section 3.2, the acrylic plate on End 1 of the longeron was attached to a stiff aluminum plate, so it was assumed that the acrylic plate did not add additional compliance beyond that of the bending machine. However, the acrylic plate on End 2 was unsupported so its compliance needed to be accounted for. This was done by including the acrylic plate on End 2 in the numerical model.

Numerical Model

The structure in the numerical model was a longeron and the acrylic plate on End 2. The numerical longeron was modeled to have the nominal geometrical parameters described in Section 3.2 and the acrylic plate had the same dimensions as the experimental plates. The material properties of the composite flange and web were determined by conducting tensile and bending tests to compute the components of the generalized stiffness matrices, A-B-D, for the flange and web materials. More details about the testing process and the values of the A-B-D matrices are given in [46]. The material properties of continuous cast acrylic were used to model the acrylic plate.

The longeron was modeled using 4-node shell elements with reduced integration and hourglass control (S4R). 8-node linear brick elements with reduced integration and hourglass control (C3D8R) were used to model the acrylic plate. A quad-dominated mesh with a side length of 0.5 mm was used to model the longeron and a hex mesh with a side length of 2 mm was used to model the acrylic plate. The mesh size was refined until the critical buckling bending moment of a perfect longeron converged.

Model of Loading and Boundary Conditions

The boundary conditions of the numerical model were created to mimic the boundary conditions of the experimental bending machine as closely as possible. The entire bending machine could have been modeled, but the air bearings, rails and other components would be difficult to simulate with high fidelity. Instead, the compliance of the air bearings, rails and aluminum attachment plates was modeled using bending springs that were compliant only in bending about the vertical axis. In order to determine the spring constant, the bending stiffness of End 1 was measured experimentally by clamping the bottom of the aluminum plate (with no structure mounted on the bending machine) and rotating motor while measuring the bending moment. The spring constant was determined by fitting a line to the bending moment-rotation data and computing the slope of the best fit line. It was found to be $K = 2,215$ Nmm/°. For simplicity, it was assumed that the stiffness of End 2 was the same as that of End 1. This assumption neglects the compliance of the vertical slider and the shorter aluminum plate on End 2, but it is believed that these details do not significantly affect the overall bending stiffness. The compliance of the acrylic plate on End 2 was included since it was modeled directly.

At End 1, one end of the bending spring was attached to a reference point at the centroid of the longeron cross-section (RP-1), which was connected to the nodes in the first 1.5 mm of the longeron using a multi-point beam constraint. The other end of the spring was attached to a reference point above End 1 of the longeron (RP-2), which was constrained in all degrees of freedom except rotation about the vertical axis. A rotational boundary condition was applied to RP-2 to create the bending and simulate the motor in the bending machine. This rotation was transferred through the bending spring to the longeron, simulating the bending machine's compliance. RP-1 was allowed to translate along and rotate about the x-axis to simulate the air bearing on the bending machine, while vertical translation and axial translation and rotation were held fixed.

The nodes in the 1.5 mm of the longeron closest to End 2 were rigidly attached to the acrylic plate at End 2 using a tie constraint. One end of the bending spring at End 2 was attached to a reference point (RP-3) that was connected, using a coupling constraint that constrained all degrees of freedom, to a region of the acrylic plate that was approximately the size and location of the vertical slider on the bending machine. The other end of the spring was attached to a reference point above the acrylic plate (RP-4) that was fixed in all degrees of freedom. To simulate the vertical slider and air bearing on the bending machine, vertical translation and axial translation and rotation were free at RP-3, while displacement and rotation in the x-direction were constrained.

Finite Element Analysis

The Riks arc-length solver [47] in Abaqus Standard with nonlinear geometry was used to statically bend the longeron and measure the bending moment as the rotational boundary condition was applied. An initial arc-length increment of 0.05 with automatic incrementation was found to yield the best convergence. The arc-length solver was used since it allows the structure's pre-buckling path, critical buckling load and post-buckling path to be computed in a single step, and clearly shows the bifurcation in the moment-rotation curve that occurs at the critical buckling load and additional bifurcations if they exist.

Initially, the iterative nonlinear eigenvalue analysis described in [38] was used to compute the critical buckling load, and then the arc-length solver was used in a subsequent step to compute the post-buckling behavior. However, it is preferable to see the entire equilibrium curve at once, and the critical buckling load computed using the arc-length solver (denoted by a local maximum in the bending moment) was found to be extremely close to that computed by the nonlinear eigenvalue analysis. Additionally, the buckled shapes computed by the arc-length solver are more realistic than the wave-like mode shapes predicted by the eigenvalue analysis. For these reasons, it was decided to use a single step with only the arc-length solver for all bending and buckling computations.

Model of Imperfection

There are two methods for creating imperfections on the numerical longeron's flanges. The first method uses a single model where the imperfection is created in the first step and bending occurs in the second step. This results in stresses caused by the imperfection being carried over into the bending step. The second method uses two separate models, both with the same geometry, material properties and mesh. The imperfection is created in the first model and the nodal displacements are saved and imported into the second model where the bending occurs. This creates a purely geometrical imperfection with no initial stress, which most closely simulates the manufacturing imperfections in experimental longerons, where the displacement can be measured and the stress caused by the imperfection is difficult to measure but likely fairly small.

In both methods, the imperfection is created by applying a displacement boundary condition to a region of the flange where it is desired to create the imperfection and using Abaqus' static general solver to compute the shape of the imperfections. Then, the bending and buckling behavior of the imperfect longeron is computed by applying a rotational boundary condition and using the arc-length solver as described above. Though the first method seems simpler since only one model is required, issues were encountered when trying to create imperfections of a given shape since the bending machine's boundary conditions allowed unwanted displacements and rotations. Furthermore the stress created by the imperfection caused convergence issues in the bending step. For these reasons, the second method was used in this work to create geometric imperfections with no initial stress.

To create an imperfection of the desired shape in the first model, all parts of the longeron outside the region of the imperfection were clamped to prevent unwanted displacements, and a displacement boundary condition was applied to the imperfection region. After running the simulation, the final increment resulted in a longeron with the desired imperfection and no other displacements. Then, the nodal displacements of the imperfect longeron were imported into the second model using the *Imperfection command in the second model's input file. Since only the nodal displacements were imported into the second model, it had the geometry of the imperfection but no initial stress. The bending machine's boundary conditions, described above, were applied to the longeron in the second model and the bending and buckling behavior of the imperfect longeron were simulated.

Four types of local imperfections were modeled to study the effect of different types of imperfections on the longeron's bending and buckling behavior: bumps, dimples, ridges and valleys. All imperfections were created on the flange that would be in compression once bending was applied. The region of the flange where the displacement boundary condition was applied was elliptical for bumps and dimples, and rectangular spanning the entire circumferential width of the flange for ridges and valleys. The displacement field was applied normal to the flange and described by a shape function, which approximated the shape of the imperfections observed experimentally. To ensure that the displacement would always be normal to the flange, it was simplest to use a shape function in circumferential coordinates where the radial displacement, Δr, was a function of the axial, z, and circumferential, θ, coordinates. The origin of the circumferential coordinate system in the in-plane direction was at the center of the circle formed by the arc of the flange on which the imperfection was created, and at End 1 of the longeron in the axial direction, as shown in Fig. 3.2.

The shape function for bumps and dimples was a single period of a cosine wave surface in both the z and θ directions:

$$\Delta r(z,\theta) = \pm 0.25A\left(\cos\left(\frac{2\pi(z-C_z)}{L_z}\right)+1\right)\left(\cos\left(\frac{2\pi R(\theta-C_\theta)}{L_\theta}\right)+1\right)$$

$$\text{for } z \in \left[C_z - \frac{L_z}{2}, C_z + \frac{L_z}{2}\right] \text{ and } \theta \in \left[C_\theta - \frac{L_\theta}{2R}, C_\theta + \frac{L_\theta}{2R}\right], \text{ with } \Delta r = 0 \text{ otherwise} \tag{3.1}$$

where A is the imperfection amplitude, C_z and C_θ are the coordinates of the center of the imperfection, L_z is the length of the imperfection in the z-direction, L_θ is the arc length of the imperfection in the θ-direction, and R is the nominal flange radius that is used to convert $(\theta - C_\theta)$ from an angle to an arc length. The function was positive for bumps and negative for dimples. The cosine function was translated by one in the radial direction so that the maximum amplitude would be at the center and the values at the edges would be zero. This form of shape function was chosen because its value and first derivative are both zero at the edges of its domain:

$$\begin{aligned} \Delta r(z = C_z \pm \frac{L_z}{2}, \theta) = 0, \quad \Delta r(z, \theta = C_\theta \pm \frac{L_\theta}{2R}) = 0, \\ \left.\frac{\partial(\Delta r)}{\partial z}\right|_{z=C_z \pm \frac{L_z}{2}} = 0, \quad \left.\frac{\partial(\Delta r)}{\partial \theta}\right|_{\theta=C_\theta \pm \frac{L_\theta}{2R}} = 0 \end{aligned} \tag{3.2}$$

which makes the imperfection smooth, as is the case for real imperfections. A similar cosine based shape function was used by Ref. [44] to define the shape of geometric, stress-free imperfections. Additionally, using a shape function with zero value at the edges of its domain simplified the process of creating the numerical imperfection by enabling the parts of the longeron outside the imperfection region to be clamped in the first model where the imperfection was created, as described above. Using a Gaussian based shape function, which is exponentially small away from the center of the imperfection but nonzero, as was done in Ref. [15] and Ref. [40], would have resulted in a similar imperfection shape but created additional numerical complexity that this study preferred to avoid.

A similar shape function was used for the ridge and valley imperfections. To make the shape function in Eq. (3.1) uniform in the circumferential direction, the imperfection length in the θ-direction was set to $L_\theta = \infty$. This resulted in a single period of a cosine wave in the z-direction that spans the entire width of the flange in the θ-direction:

$$\begin{aligned} &\Delta r(z, \theta) = \pm 0.5A \left(\cos\left(\frac{2\pi(z - C_z)}{L_z} \right) + 1 \right) \\ &\text{for } z \in \left[C_z - \frac{L_z}{2}, C_z + \frac{L_z}{2} \right] \text{ and } \theta \in [0, 120^\circ], \text{ with } \Delta r = 0 \text{ otherwise.} \end{aligned} \tag{3.3}$$

The function was positive for ridges and negative for valleys.

For all imperfection types, the imperfection was always axially centered on the longeron, so $C_z = 250$ mm. When comparing the effects of the different types of imperfections, the imperfection amplitude was set to $A = 0.5$ mm and the imperfection length in the axial direction was $L_z = 10$ mm. The bump and dimple imperfections were centered on the edge of the flange, so $C_\theta = \frac{2\pi}{3}$ rad, and the arc length for these imperfections was $L_\theta = 10$ mm. Since the imperfections were centered on the edge of the flange, only half the length of the imperfection in the circumferential direction was actually on the flange so the actual arc length of the imperfection was $\frac{L_\theta}{2}$, resulting in a semi-elliptical imperfection region, as shown in Fig. 3.2.

Next, the imperfection amplitude and length were varied for the bump, dimple, ridge and valley. Imperfection amplitudes of 0.01 mm, 0.1 mm and 1 mm were simulated to study the effects of the imperfection amplitude across varying orders of magnitude, while the imperfection length remained at $L_z = 10$ mm. For the bumps and dimples, the arc length remained $L_\theta = 10$ mm and the location remained at the edge of the flange. Then, the imperfection length was increased to $L_z = 100$ mm, and $L_\theta = 20$ mm for bumps and dimples, while keeping the imperfection amplitude constant at $A = 0.5$ mm, and the location at the edge of the flange for bumps and dimples. This arc length was chosen for the longer imperfections because they could not be circular (since the flange arc length is 28.5 mm) and $L_\theta = 20$ mm resulted in 10 mm actually being on the flange, which is about a third of the total flange arc length. It was desired not to exceed this arc length so that the bumps and dimples would maintain their properties and not become similar to the ridges and valleys. Finally, in the last portion of the numerical study, the location of a bump imperfection in the circumferential direction was moved to the center of the flange, $C_\theta = \frac{\pi}{3}$ rad, with the amplitude remaining at $A = 0.5$ mm and the length remaining at $L_z = 10$ mm and $L_\theta = 10$ mm.

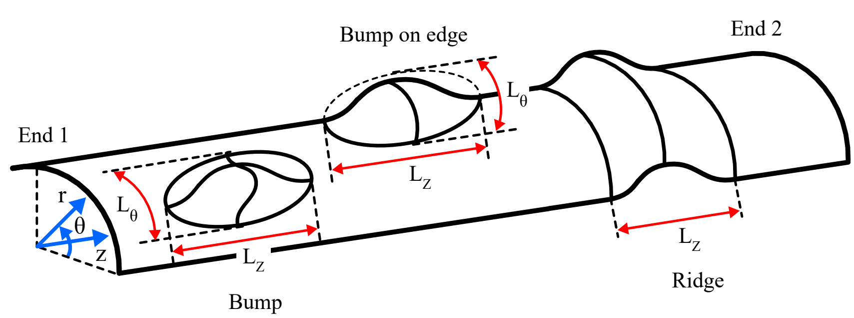

Figure 3.2: Schematic of a single flange showing the different types of imperfections.

3.4 Test Structures and Experimental Methods

Four composite longeron test structures were studied in this work. The first was manufactured using an autoclave two-cure process, and the subsequent three samples were manufactured using an autoclave one-cure process. Both manufacturing processes are described in the following section and then the experimental methods used to bend the longerons and measure their critical buckling load are presented.

Longeron Manufacturing

For all longeron test samples, the flanges were 80 µm thick and had the layup $[\pm 45_{GFPW}/0_{CFUD}/\pm 45_{GFPW}]$. The web region was 185 µm thick and had the layup $[\pm 45_{GFPW}/0_{CFUD}/\pm 45_{3,GFPW}/0_{CFUD}/\pm 45_{GFPW}]$. CFUD represents a unidirectional layer of Mitsubishi Chemical's Pyrofil MR 70 12P carbon fiber that is 30 µm thick and GFPW represents a plain weave scrim glass ply that is 25 µm thick. Both the carbon fiber and scrim glass plies were impregnated with North Thin Ply Technology's ThinPreg 415 resin, and the complete $[\pm 45_{GFPW}/0_{CFUD}/\pm 45_{GFPW}]$ stack was supplied by North Thin Ply Technology.

In the two-cure manufacturing process, the three-ply preimpregnated laminates for the two flanges were first cured individually on U-shaped aluminum molds with a radius of 12.7 mm. After the flanges were cured, a single ply of ±45 GFPW was added to the web region of one of the molds, and the two molds were clamped together and cured for a second time to bond the flanges. When the longeron was removed from the mold after the second cure, the flanges sprang back to a radius of approximately 13.6 mm, due to residual stress from cooling at the end of the curing cycle. More details about this manufacturing process are described in [38]. In a final step, the longeron used in this work was cut to an axial length of 500 mm, discarding material near the ends that had greater imperfections. Then, the flanges were temporarily flattened and cut to a nominal arc length of 28.5 mm, which corresponds to a subtended angle of 120° when the flange radius is the nominal 13.6 mm. Lastly, the bottom of the web region was cut to a nominal length of 8 mm.

The one-cure manufacturing process began by cutting the three-ply laminates for the two flanges to an axial length of 1,700 mm and a nominal total arc length of 36.5 mm. The two laminates were placed on the same U-shaped molds and aligned such that the web region was 8 mm long and the flange arc length was 28.5 mm, to achieve the same nominal lengths as in the two-cure process. Next, a single ply of ±45 GFPW was added to the web region of one of the molds. Then, the two molds were clamped together, vacuum bagged, and cured. After removing the longeron from the mold, it was expected that the flanges would spring back to a nominal radius of 13.6 mm as they do after the better characterized two-cure process. This was found not to be the case, as will be discussed in a later section. Approximately 100 mm was cut off each end of the longeron and discarded since the ends were found to have the significantly more imperfections than the central portion of the longeron. Then, the remaining approximately 1,500 mm long longeron was cut into three 500 mm long test samples. More details about the one-cure processes can be found in [48]. The one-cure process was later found to introduce more imperfections in the longerons than the two-cure process, as discussed in Chapter 2. However, for the purpose of this work, the three longerons manufactured using the one-cure process provided good examples of the worst case manufacturing imperfections, while the longeron manufactured using the two-cure process provided an example of the best case experimental longeron with the least imperfections.

As mentioned in Section 3.2, the ends of the four test samples were rigidly glued into 6 mm thick acrylic end plates. For each end of each longeron, a thin slit matching the exact cross section of that end, determined using the shape measurement process described in Chapter 2, was laser cut through about three quarters of the thickness of the corresponding acrylic plate. Then, each end of the longeron was fitted into the slits and epoxied into the plate to form a rigid connection between the longeron and the end plates. This rigid connection allowed the bending machine boundary conditions to be applied directly to the longeron.

Imperfection Measurements

The shape of the longerons was measured using a Faro Arm (Edge 14000) with a 3D laser scanner attachment (ScanArm HD), which has an accuracy of ±25 µm. The laser scanner generates a 3D point cloud of the scanned object using the CAM2 Measure 10 software. The method described in Chapter 2 was used to analyze the point cloud data from the laser scanner and compute the local and global imperfections in the longerons. Variations in the flange radius and subtended angle in cross-sections taken at multiple locations along the length of the longerons were computed and used to calculate the mean of these parameters for each flange of the experimental longerons. The difference between the local radius of each data point in each flange and the mean radius of the respective flange, or the radial deviations, was computed and displayed in a contour plot for both the front and back flanges of each of the longeron test samples.

Bending Procedure

At the beginning of the experimental campaign, the counter mass above each air bearing on the bending machine was set such that when no test sample was mounted on the bending machine, the moments from the counter masses compensated for the moments due to the mass of the components below the air bearings. This was done by adding mass to the counter masses until the moment about the x-axis for End 1 and z-axis for End 2 was approximately zero. The counter masses were calibrated with no sample mounted on the bending machine because the longeron test samples were fairly light and did not create a large moment and there was concern about large moments before the counter masses were calibrated damaging the longerons. This also simplified the procedure since the counter masses above the air bearings remained the same for all test samples.

Before mounting each sample to the bending machine, the load cells on either end of the bending machine were zeroed. Then, a longeron test sample was mounted onto the bending machine by screwing the acrylic plates onto the aluminum plate on End 1 and the vertical slider on End 2, as shown in Fig. 3.1. To balance the vertical force due to gravity and allow the vertical slider to move freely, a counter mass equaling half the mass of the sample plus the mass of the translating part of the vertical slider was attached to the acrylic plate on End 2 through a low-friction pulley. After mounting the longeron, if there was a small bending moment about the vertical axis, small rotations were incrementally applied until the moment became zero.

Once all forces and moments were zero, the longeron was rotated about the vertical axis. A rotation of positive 2° was applied to the sample, which created compression in the front flange, and the bending moment and rotation were measured during the loading. Once the locations of any buckles on the front flange were noted, a rotation in the opposite direction was applied to bring the longeron back to its unloaded condition. The longeron was left unloaded for one to two hours to allow any residual moment caused by hysteresis during the unloading to dissipate. Then, a rotation of negative 2° was applied to create compression in the back flange. After all data was saved, the longeron was unloaded by applying a rotation in the opposite direction. This was repeated for 3 to 5 trials for each sample. The critical buckling bending moment and rotation were determined to be the point in the moment-rotation curve where a local maximum was reached, after which the bending moment decreased sharply with increased rotation. If a test sample did not buckle below an applied rotation of 2°, a rotation of 3° was applied and the above procedure was repeated for that sample.

3.5 Numerical Results

The results of the numerical study investigating the effects of imperfection type, amplitude, length and circumferential location on the longeron's knockdown factor are presented in the following sections. In order to compare the buckling behavior of the imperfect longerons to that of a perfect longeron, the results of a numerical analysis of a perfect longeron are presented before continuing to discuss the results of the imperfect longerons.

Perfect Longeron

The numerical study began by computing the behavior of a perfect longeron loaded in pure bending to be used as a baseline to compare to the behavior of the imperfect longerons. To achieve convergence of the arc-length solver past the first bifurcation, a very small bump imperfection with an amplitude of $A = 0.004$ mm and length of $L_z = 10$ mm and $L_\theta = 10$ mm was introduced on the edge of the flange in compression, following the procedure described in Section 3.3. The first critical buckling load of the longeron with the small bump was within 1% of that of the perfect longeron and the mode shapes of the perfect and slightly imperfect longerons were the same. Therefore, it was considered reasonable to use the slightly imperfect longeron in place of the perfect longeron, for which post-buckling convergence could not be achieved. For the remainder of the chapter, when referring to the perfect longeron, the results of the slightly imperfect longeron will actually be shown instead.

The bending moment-rotation curve of the perfect longeron is shown in Fig. 3.3. The moment-rotation curve is initially linear, as expected since the longerons behave linear elastically below the critical buckling load. Then, a local maximum is reached at a critical bending moment of 318 Nmm, the longeron buckles and the moment decreases sharply, following the initial loading curve quite closely. After decreasing to a moment of about 200 Nmm, the longeron restabilizes and the moment and rotation increase again following a post-buckling path with lower bending stiffness than the initial loading curve. A second bifurcation is reached at a moment of 523 Nmm, after which the longeron cannot regain stability and numerical convergence is lost. Note that although there is a softening response in the post-buckling regime between the first and second bifurcations, bending moments significantly higher than the first critical buckling moment can be achieved in this regime.

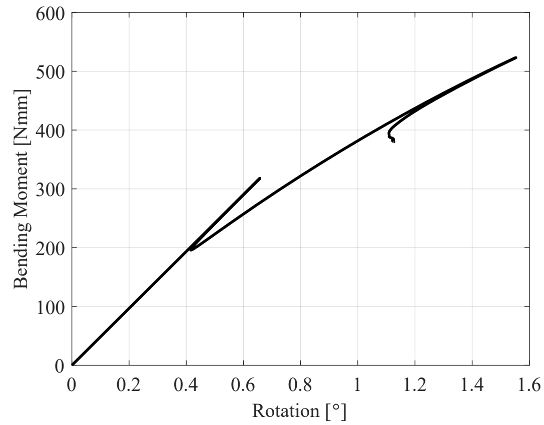

Figure 3.3: Plot of bending moment-rotation curve for perfect longeron.

Fig. 3.4 shows the shapes of the perfect longeron before and after the first and second bifurcations. In both cases, the buckle(s) forms before the bifurcation and gradually grows until the bifurcation occurs, after which the buckle gets significantly larger. Immediately after the first bifurcation, the longeron has two small local buckles. One is centered at z = 442 mm (58 mm from End 2) with an amplitude of 0.12 mm, and the other is at the axial center of the longeron, at z = 250 mm, with an amplitude of 0.07 mm. The maximum amplitude of both buckles occurs at the edge of the flange. In the post-buckling regime after the first bifurcation, the axially centered buckle gradually grows and becomes quite large, while the buckle near End 2 disappears. Then, after the second bifurcation, the deformation is more global and the longeron has a large, axially centered buckle with a maximum amplitude of 7.8 mm at the edge of the flange, as well as axial twist near End 2. This asymmetric twist likely occurs because axial rotation is allowed only at End 2. It is interesting to note that in all cases, the buckles form outwards in the direction that flattens the flange and decreases its radius of curvature.

Varying Imperfection Type

The buckling behavior of longerons with a bump, dimple, ridge, and valley imperfection was computed as described in Section 3.3. All of the imperfections had an amplitude of A = 0.5 mm and length L_z = 10 mm in the axial direction. The bump and dimple imperfection had an arc length of L_θ = 10 mm in the circumferential direction and were centered on the edge of the flange.

The bending moment-rotation curves for the longerons with different types of imperfections are compared in Fig. 3.5. The moment-rotation curve of the perfect

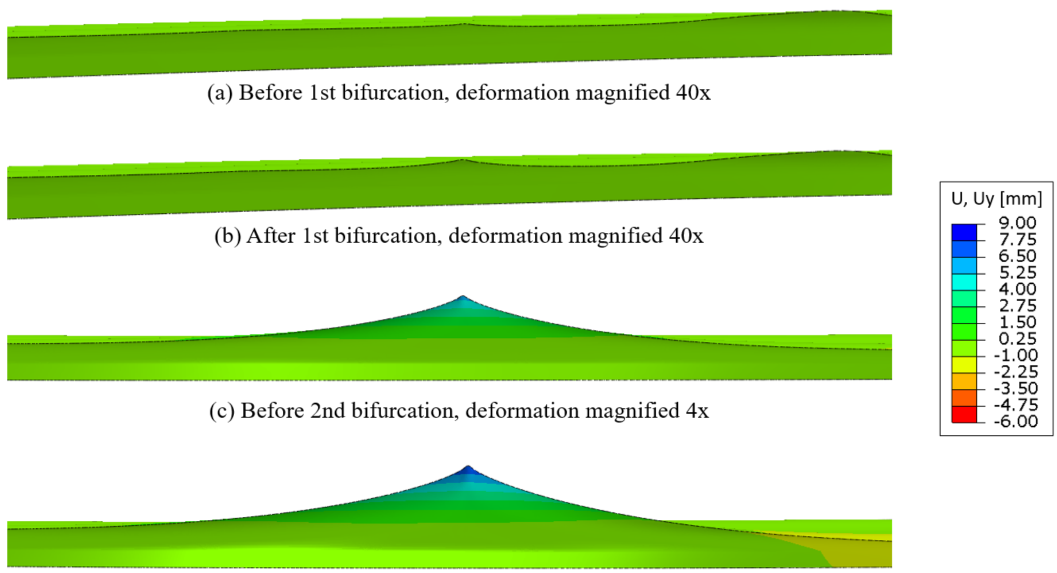

(a) Before 1st bifurcation, deformation magnified 40x

(b) After 1st bifurcation, deformation magnified 40x

(c) Before 2nd bifurcation, deformation magnified 4x

(d) After 2nd bifurcation, deformation magnified 4x

Figure 3.4: Shape of perfect longeron before and after the first and second bifurcations. The color scale shows vertical displacement.

longeron is included in Fig. 3.5 for reference, and the bifurcation points for each longeron are circled. The curves for the longerons with bump and dimple imperfections show a softening response, after an initial linear region, but do not have a clear bifurcation below the first critical buckling load of the perfect longeron. This is because the imperfection decreases the first critical buckling load so much that a first bifurcation does not occur and, instead, the longeron immediately follows the post-buckling path of the perfect longeron. This effect of large amplitude imperfections was predicted analytically by Ref. [8, 9] and numerically by Ref. [44]. Leclerc et al. [39] also observed this loss of the first bifurcation in experimental longerons loaded in bending, when comparing their experimental results to numerical ones. In the post-buckling regime, the longerons with bump and dimple imperfections have approximately the same stiffness as the perfect longeron. The curves for the ridge and valley imperfections do not have any bifurcations and instead have a limit point where bending stiffness is lost. These longerons are significantly more compliant than the longerons with the bump and dimple, suggesting that the ridge and valley imperfections have the greatest impact on both the longeron's stability and stiffness.

The second mode critical buckling moments and rotations as well as the knockdown factor of the longerons with different types of imperfections are compared to that of the perfect longeron in Table 3.1. Mode 2 was chosen for the comparison because the longerons with bump and dimple imperfections do not have a first buckling

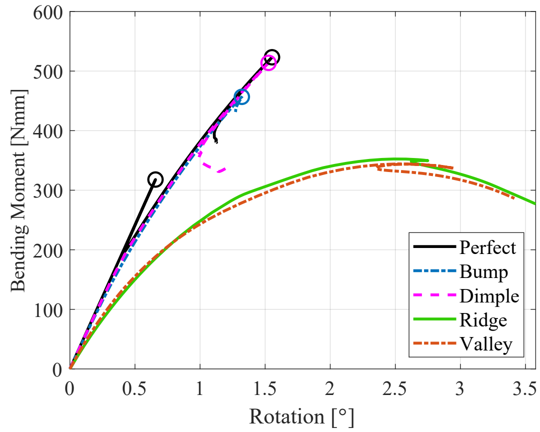

Figure 3.5: Comparison of bending moment-rotation curves for longerons with different imperfection types. Bifurcation points are circled.

mode. For this reason, the second mode values will be compared for the other parameters that are varied later in the section as well. The longeron with the dimple imperfection has the highest knockdown factor of 0.98. Despite this high knockdown factor, the dimple causes the first bifurcation to disappear, resulting in lower bending stiffness than the perfect longeron at lower rotations. The longeron with the bump imperfection has the next highest knockdown factor of 0.87. The bump has a greater effect on stability than the dimple likely because the longeron naturally buckles outwards so the bump aids buckling while the dimple opposes it. The ridge and valley have the lowest knockdown factors of 0.67 and 0.66, respectively. Since the ridge and valley do not have bifurcation points, the knockdown factor was calculated using the bending moment at the limit point instead of the moment at the second bifurcation. It is interesting that the valley has a lower knockdown factor than the ridge, despite the ridge being an outward imperfection similar to the bump, suggesting that the shape of an imperfection has a greater effect on stability than its orientation. These results suggest the following order of the effect of the four types of imperfections studied on the stability of longerons from least to greatest effect: dimple, bump, ridge, valley.

Fig. 3.6 compares the shapes of the perfect and imperfect longerons after the second bifurcation. For the longerons with ridge and valley imperfections, the shape is shown at the limit point instead since they do not have a second bifurcation. In all cases the buckle formed approximately at the axial center of the longeron, which is the location of the imperfection. As seen in Fig. 3.6b, the bump imperfection has little effect on the mode shape and the shape of the longeron with the bump is very similar to that of the perfect longeron. The dimple creates a slight asymmetry in the

Table 3.1: Mode 2 Critical Buckling Moments and Rotations for Different Imperfection Types

Imperfection Type	**Crit. Moment** [Nmm]	**Crit. Rotation** [°]	**Knockdown Factor**
Perfect	523	1.55	—
0.5 mm Bump	457	1.32	0.87
0.5 mm Dimple	514	1.53	0.98
0.5 mm Ridge[1]	352	2.49	0.67
0.5 mm Valley[1]	344	2.52	0.66

[1] Values at limit point where bending stiffness is lost.

mode shape, as seen in Fig. 3.6c, but the buckle is still localized at the edge of the flange, similar to the mode shape for the perfect longeron. In contrast, the ridge (Fig. 3.6d) causes a kink throughout the entire flange cross section in the circumferential direction, though the maximum amplitude of the buckle is at the edge of the flange. The valley imperfection (Fig. 3.6e) creates shear throughout the flange cross section, since the flange wants to buckle upwards but the valley is downwards. Additionally, the buckles that occur with the ridge and valley imperfections have lower amplitude and are narrower than the buckles that occur with the bump and dimple imperfections. However, in all cases, the buckles form outwards and the maximum amplitude is at the edge of the flange regardless of the type of imperfection that is introduced. This shows that the natural buckling shape dominates over the shape of the imperfection.

Varying Imperfection Amplitude

The bending moment-rotation curves for imperfection amplitudes of 0.01 mm, 0.1 mm and 1 mm for bump, dimple, ridge and valley imperfections are compared to each other and to the perfect longeron's curve in Fig. 3.7. For all four imperfections types, the moment-rotation curves of the longerons with 0.01 mm amplitude imperfections closely follow that of the perfect longeron, achieving a first bifurcation in all cases. The first critical buckling moment for the longerons with 0.01 mm amplitude dimple and valley imperfections is about the same as that of the perfect longeron, suggesting that these imperfections have little to no effect on the longeron's stability when their amplitude is small. However, convergence of the arc-length solver past the first bifurcation could not be achieved for these imperfections. The longerons with 0.01 mm amplitude bump and ridge imperfections had knockdown factors of 0.90 and 0.87, respectively for their first buckling mode. It makes sense that the bump and ridge imperfections have a greater impact on the longeron's stability than the dimple

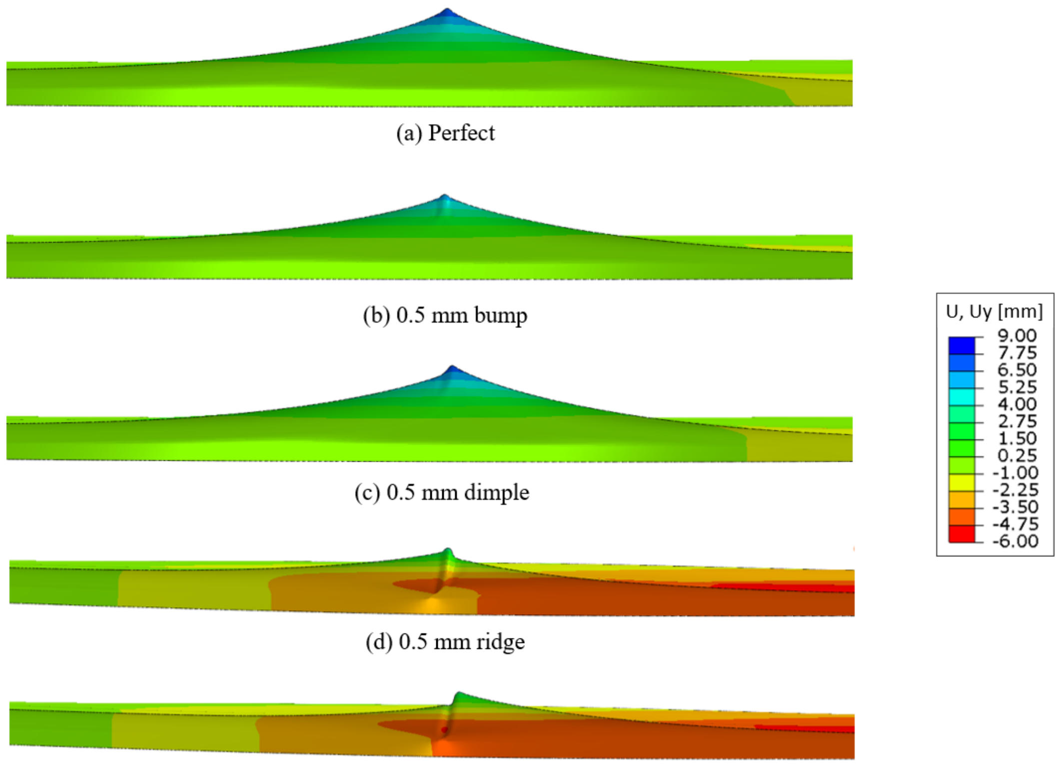

(a) Perfect

(b) 0.5 mm bump

(c) 0.5 mm dimple

(d) 0.5 mm ridge

(e) 0.5 mm valley

Figure 3.6: Comparison of buckled shapes after 2nd bifurcation for different imperfection types. The deformation is magnified 4x, and the color scale shows vertical displacement.

and valley, since the bump and ridge are in the direction that buckling occurs, while the dimple and valley are in the direction that opposes buckling.

The buckling behavior of the longerons changes significantly as the imperfection amplitude increases. At an imperfection amplitude of 0.1 mm, only the dimple imperfection has a first bifurcation and its knockdown factor is 0.68, which is fairly low. As seen in Fig. 3.7b, the moment-rotation curve of the longeron with a 0.1 mm dimple imperfection only decreases slightly after the first bifurcation before restabilizing and following the post-buckling path of the perfect longeron; while the moment-rotation curve of the longeron with a 1 mm dimple does not have a first bifurcation and immediately follows the post-buckling path of the perfect longeron. This exemplifies that as the imperfection becomes larger and more detrimental to the longeron's stability, the first critical buckling load decreases until it reaches the post-buckling path of the perfect longeron at which point a first bifurcation no longer occurs and the longeron simply follows the post-buckling path, as was discussed earlier. As seen in Fig. 3.7a, the moment-rotation curves of the longerons with

0.1 mm and 1 mm bumps both lack a first bifurcation and immediately follow the post-buckling path of the perfect longeron. However, the longeron with a 0.1 mm bump follows the perfect longeron's curve more closely and has a higher bending stiffness than the longeron with a 1 mm bump.

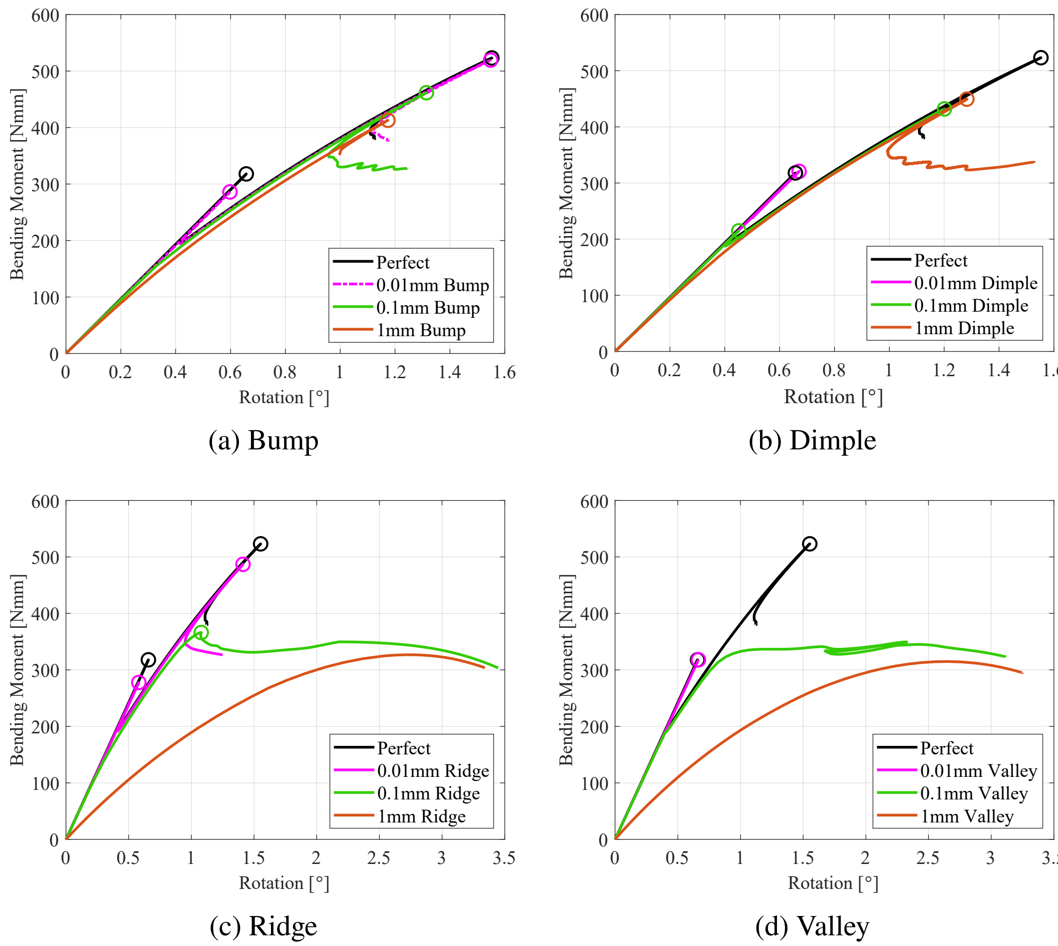

(a) Bump (b) Dimple

(c) Ridge (d) Valley

Figure 3.7: Comparison of bending moment-rotation curves for varying imperfection amplitudes. Bifurcation points are circled.

The effect of increased imperfection amplitude is much more significant for the ridge and valley imperfections than it is for the bump and dimple. As seen in Fig. 3.7c, the longeron with a 0.1 mm ridge has a lower bending stiffness than the longeron with a 0.01 mm ridge and lacks a first bifurcation. Additionally, the curve for the longeron with a 0.1 mm ridge only has a slight decrease after the second bifurcation, suggesting that it is close to imperfection amplitude where the second bifurcation no longeron occurs. Indeed, the curve for the longeron with a 1 mm amplitude ridge has neither a first nor second bifurcation and instead has a limit point where bending stiffness is lost. The longeron with a 1 mm ridge also has significantly lower bending stiffness than the other longerons with ridge imperfections. As seen in Fig. 3.7d, the longeron with a 0.1 mm valley initially has approximately the same bending stiffness as the perfect longeron, but it does not have any bifurcations and instead has a limit point where the bending moment plateaus. The longeron with a 1 mm valley is significantly less stiff than the other longerons with valley imperfections and has a limit point but no bifurcations, similar to the longeron with a 1 mm ridge.

Table 3.2 shows the mode 2 critical buckling moments and rotations and knockdown factors for the longerons with varying imperfection amplitudes. Values for the 0.01 mm dimple and valley are not shown because convergence past the first bifurcation could not be achieved for these longerons. In general, the knockdown factor decreases with increasing imperfections amplitude, as expected. An exception is the dimple imperfection where the 0.1 mm amplitude dimple has a slightly lower knockdown factor than the 1 mm dimple. However, the longeron with the 0.1 mm dimple has a first bifurcation while the longeron with the 1 mm dimple does not, so it can be argued that the 0.1 mm dimple has less effect on the longeron's stability than the 1 mm dimple despite the lower knockdown factor. Thus, it can be concluded that the stability of the longerons decreases with increasing imperfection amplitude.

Table 3.2: Mode 2 Critical Buckling Moments and Rotations for Varying Imperfection Amplitudes

Imperfection Type	**Crit. Moment** [Nmm]	**Crit. Rotation** [°]	**Knockdown Factor**
0.01 mm Bump	519	1.55	0.99
0.01 mm Ridge	487	1.41	0.93
0.1 mm Bump	462	1.31	0.88
0.1 mm Dimple	432	1.20	0.83
0.1 mm Ridge	366	1.08	0.70
0.1 mm Valley[1]	333	1.00	0.64
1 mm Bump	413	1.17	0.79
1 mm Dimple	449	1.28	0.86
1 mm Ridge[1]	327	2.75	0.62
1 mm Valley[1]	315	2.65	0.60

[1] Values at limit point where bending stiffness is lost.

Varying Imperfection Length

Next, the imperfection length was increased to $L_z = 100$ mm in the axial direction and $L_\theta = 20$ mm in the circumferential direction for bumps and dimples. An amplitude of $A = 0.5$ mm was used for all imperfections in this portion of the study.

The bending moment-rotation curves of the longerons with longer imperfections are compared to those of the longerons with shorter imperfections (which were shown previously) in Fig. 3.8, and the mode 2 critical bending moments and rotations and knockdown factors for the longerons with longer imperfections are shown in Table 3.3. As seen in Fig. 3.8a, the longerons with the longer bump and dimple imperfections do not have a first bifurcation, similar to the longerons with the shorter bump and dimple imperfections. The longeron with the longer bump has approximately the same bending stiffness as the perfect longeron in its post-buckling regime, but has a higher second critical buckling load than perfect longeron. The longeron with the longer dimple is stiffer than the perfect longeron in its post-buckling regime and its second critical buckling moment is about the same as that of the longeron with the shorter dimple.

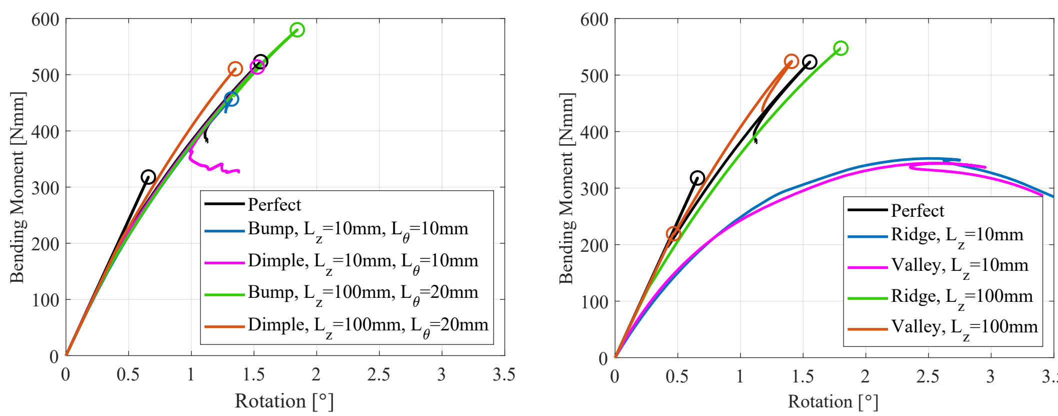

(a) Bump and dimple (b) Ridge and valley

Figure 3.8: Comparison of bending moment-rotation curves for varying imperfection lengths with A = 0.5 mm. Bifurcation points are circled.

As seen in Fig. 3.8b, the longerons with 100 mm wide ridge and valley imperfections both have a second bifurcation and generally follow the perfect longeron's path, unlike the longerons with 10 mm wide ridge and valley imperfections. The longeron with the 100 mm wide ridge lacks a first bifurcation and has a lower bending stiffness than the perfect longeron in its post-buckling regime. However, its bending stiffness is much closer to that of the perfect longeron than to the bending stiffness of the longeron with the 10 mm wide ridge. The longeron with the 100 mm wide valley has a first bifurcation, with a knockdown factor of 0.69, though the local maximum in its moment-rotation curve created by the bifurcation is very small. Then, in the post-buckling regime the longeron with the 100 mm wide valley is stiffer than the perfect longeron and has about the same second critical buckling moment as the perfect longeron. It is interesting that the wider ridge and valley imperfections have only a moderate effect on the longeron's stability, while the narrower ridge and valley severely degrade both the stability and bending stiffness. In general, these results suggest that for all imperfection types longer imperfections have significantly less effect on the longeron's stability than shorter, more localized imperfections.

Varying Imperfection Location

In the final portion of the numerical study, a bump imperfection with $A = 0.5$ mm, $L_z = 10$ mm, and $L_\theta = 10$ mm was moved to the circumferential center of the flange. Since the imperfection is no longer at the edge of the flange, the footprint of the bump was a full circle. The bending moment-rotation curve of the longeron with a bump in the center of the flange is compared to that of the longeron with a bump on the edge of the flange with the same length and amplitude in Fig. 3.9, and its mode 2 critical moment and rotation and knockdown factor are shown in Table 3.3. The longeron with the center bump has a higher bending stiffness than the longeron with the edge bump. Additionally, the longeron with the center bump has both a first and second bifurcation, unlike the longeron with the edge bump that immediately follows the perfect longeron's post-buckling path and has only a second bifurcation. However, the longeron with the center bump has a slightly lower mode 2 knockdown factor (0.82) than the longeron with the edge bump (0.87). Despite this, the existence of a first bifurcation and the higher bending stiffness of the longeron with the center bump leads to the conclusion that imperfections on the edge of the flange have a greater effect on the longeron's stability and structural properties than imperfections in the circumferential center of the flange.

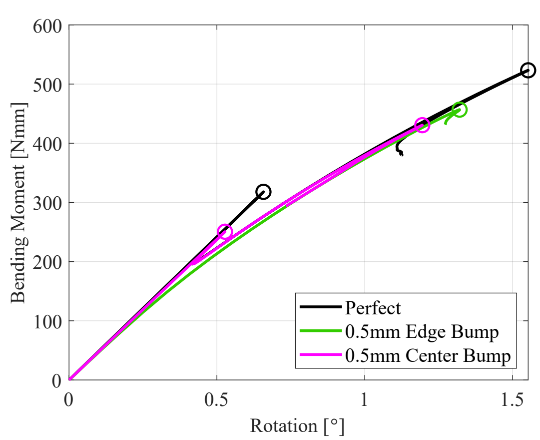

Figure 3.9: Comparison of bending moment-rotation curves for longerons with a bump on the center and edge of the flange. Bifurcation points are circled.

Table 3.3: Mode 2 Critical Buckling Moments and Rotations for Varying Imperfection Length and Location

Imperfection Type	**Crit. Moment** [Nmm]	**Crit. Rotation** [°]	**Knockdown Factor**
Bump, L_z = 100 mm, L_θ = 20 mm	580	1.85	1.11
Dimple, L_z = 100 mm, L_θ = 20 mm	510	1.35	0.98
Ridge, L_z = 100 mm	548	1.80	1.05
Valley, L_z = 100 mm	524	1.41	1.00
Center Bump	431	1.19	0.82

3.6 Experimental Results

The bending and buckling behavior of one longeron manufactured using a two-cure manufacturing process and three longerons manufactured using a one-cure process was measured following the procedure described in Section 3.4. The longeron made with two cures will be referred to as "two-cures" and the longerons made with one cure will be referred to as "Sample 1, 2 and 3." This section begins with a brief discussion of the geometric imperfections measured in the experimental longerons so that the buckling results can discussed in the context of these imperfections. Then, the results of the experimental bending and buckling tests are presented.

Geometric Imperfections

The mean and standard deviation of the flange radius, subtended angle and arc length of the four longeron test samples are shown in Table 3.4. The mean values of these parameters for both flanges of the two-cure longeron are very close to nominal, since the nominal values were determined based on the better characterized two-cure manufacturing process. In contrast, the mean flange radius of all three longerons made with one cure is smaller than nominal and varies from 12.3 mm to 12.9 mm. This is because after the single cure, the flanges did not spring back to a larger radius as was expected based on the two-cure process. The smaller flange radius caused the subtended angle to be greater than nominal since the flanges were cut to a given arc length during manufacturing. Indeed, the mean flange arc length remains within 1 mm of nominal for all samples. However, there is a consistent trend of the back flange being longer than the front flange for the one-cure samples. This suggests that the laminate for the back flange was cut slightly longer than the laminate for the front flange, since all three one-cure longerons were manufactured out of the same longer longeron.

Table 3.4: Mean Values of Longeron Geometrical Parameters
Measured values are written with mean ± std.

Sample	Flange	Radius [mm]	Subtended angle [°]	Arc length [mm]
	Nominal	13.6	120	28.5
2 cures	Front	13.60 ± 0.17	120.75 ± 1.86	28.65 ± 0.19
	Back	13.53 ± 0.12	121.71 ± 1.67	28.73 ± 0.19
Sample 1, 1 cure	Front	12.34 ± 0.39	131.52 ± 3.99	28.29 ± 0.48
	Back	12.41 ± 0.40	135.24 ± 4.06	29.28 ± 0.34
Sample 2, 1 cure	Front	12.81 ± 0.12	129.77 ± 2.00	29.01 ± 0.41
	Back	12.87 ± 0.10	129.95 ± 2.09	29.18 ± 0.37
Sample 3, 1 cure	Front	12.83 ± 0.60	127.84 ± 5.64	28.57 ± 0.26
	Back	12.84 ± 0.52	128.58 ± 5.02	28.78 ± 0.24

Figures 3.10 and 3.11 show plots of the local radial deviations from the mean flange radius for each flange of the two-cure longeron and the three one-cure longerons, respectively. The axial coordinate, measured from the left end of each longeron, is plotted on the horizontal axis, the circumferential coordinate is plotted on the vertical axis, with the edge of the flange at the top of the plot, and the contours show the radial deviations, or imperfection amplitudes. Positive radial deviations indicate a larger local radius, meaning a bump or ridge, and negative deviations indicate a smaller local radius, a dimple or valley, on the flange. For example, the red region in the middle of Fig. 3.11f is a ridge and the blue region on the left side of Fig. 3.11a is a valley. The variation in the amount of white space at the top of the plots is caused by variations in the flange subtended angle.

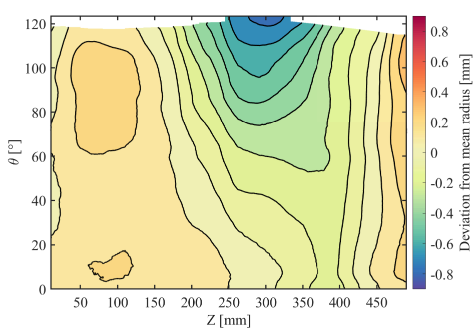

(a) Front flange, two-cures

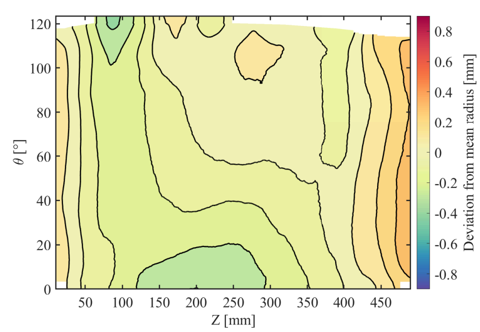

(b) Back flange, two-cures

Figure 3.10: Local radial deviations from the mean flange radius for the two-cure longeron. Positive deviations indicate outward imperfections (bumps or ridges) and negative deviations indicate inward imperfections (dimples or valleys).

When comparing Fig. 3.10 and Fig. 3.11, it is evident that the one-cure longerons

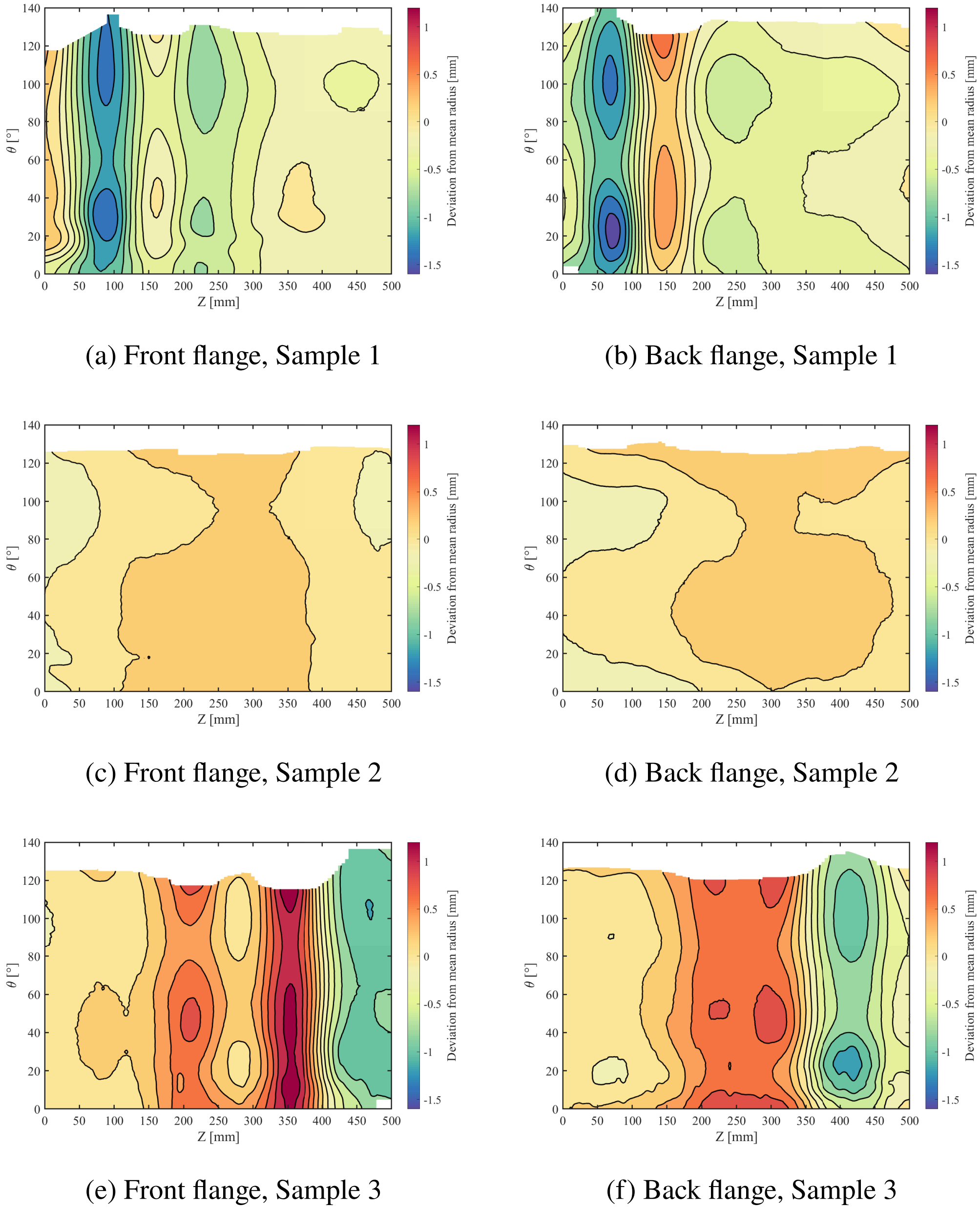

(a) Front flange, Sample 1

(b) Back flange, Sample 1

(c) Front flange, Sample 2

(d) Back flange, Sample 2

(e) Front flange, Sample 3

(f) Back flange, Sample 3

Figure 3.11: Local radial deviations from the mean flange radius for the one-cure longerons.

generally have larger amplitude imperfections and more imperfections on each flange than the two-cure longeron. Additionally, the one-cure longerons have ridges and valleys, which were shown in Section 3.5 to be more detrimental to the longeron's stability than bumps and dimples, while the two-cure longeron does not. The dominant imperfection in the front flange of the two-cure longeron is a dimple with $A = 0.5$ mm, $L_z = 268$ mm and $L_\theta = 32$ mm, as seen in the blue region at the top center of Fig. 3.10a. The dominant imperfection in the back flange is a dimple with

A = 0.3 mm, L_z = 121 mm and L_θ = 16 mm, seen in the green region at the top left of Fig. 3.10b. As seen in Fig. 3.11, Sample 2 has the least local imperfections of the three one-cure longerons, while Sample 3 has the greatest local imperfections. The front flange of Sample 3 has a 0.7 mm amplitude bump (orange region at top center of Fig. 3.11e), a 0.8 mm amplitude ridge (red region on the right side of Fig. 3.11e), and a 0.9 mm amplitude valley (green region on the far right of Fig.3.11e), which is the most imperfections of any of the experimental longerons. Sample 1 has a moderate amount of imperfections with the front flange having a 1.1 mm amplitude valley and a 0.5 mm amplitude ridge (blue region and yellow region on the left side of Fig. 3.11a, respectively), and the back flange having a 0.8 mm amplitude valley and a 0.9 mm amplitude ridge (blue region and orange region on the left side of Fig. 3.11b, respectively).

Bending and Buckling Results

The bending moment-rotation curves for the two-cure longeron are shown in Fig. 3.12 and the curves for the one-cure longerons are shown in Fig. 3.13. In both figures, the plots on the left show the results when a positive rotation was applied, resulting in a positive bending moment, and the front flange was in compression. The plots on the right show the results when a negative rotation was applied, resulting in a negative moment, and the back flange was in compression. In other words, two sets of bending tests were performed on each sample: one where the front flange was in compression, and one where the back flange was in compression. To make the results with opposite moments and rotations easier to compare, the magnitude of the bending moment and rotation was plotted in Fig. 3.12 and Fig. 3.13. In most cases, three trials were performed for each flange and the agreement between trials was generally very good. However, if the results differed significantly between trials, four or five trials were performed.

The moment-rotation curves in Fig. 3.12 and Fig. 3.13 began with the magnitude of the bending moment increasing with increased applied rotation. Then, a local maximum in the bending moment was reached and the moment decreased sharply with increased rotation, denoting that buckling had occurred. This drop in moment was accompanied by the observation of a local buckle on the flange in compression. The snap of the buckle often caused the structure to oscillate on the bending machine's low friction air bearings and these oscillations are seen in some of the moment-rotation curves after the decrease in moment (for example, the oscillations on the right side of Fig. 3.13b). In some cases, the longeron restabilized after buckling and

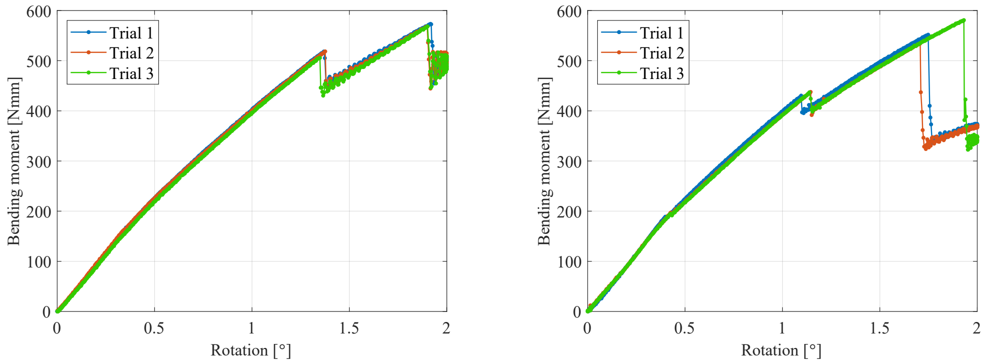

(a) Front flange in compression

(b) Back flange in compression

Figure 3.12: Magnitude of bending moment-rotation curves for two-cure longeron.

the bending moment continued increasing up to the next critical buckling load. One thing to note is that the experiments were rotation controlled so the magnitude of the rotation could only increase monotonically. Therefore, when buckling occurred and the bending moment dropped, the moment-rotation curve was either nearly vertical or had a negative slope. In contrast, in the numerical moment-rotation curves, the rotation often decreased along with the bending moment after buckling occurred causing the curve to follow the initial loading path, which was possible using the arc-length solver in the simulations since it had no restrictions on the direction of the rotation.

In most cases, the experimental longerons do not have a first bifurcation below the critical buckling load of the numerical perfect longeron, similar to the numerical longerons with large amplitude imperfections, so the first observation of buckling is actually the second critical buckling load. This makes sense, since most of the experimental longerons have large amplitude imperfections which cause the first bifurcation to disappear, as was discussed in Section 3.5. Exceptions to this are the back flanges of Samples 1 and 2, which both had a first bifurcation when loaded in compression, as seen by the small decrease in bending moment that occurs at a rotation of 0.6° in Fig. 3.13b and at 1° in Fig. 3.13d. It makes sense that the back flange of Sample 2 has a first bifurcation since it has no significant local imperfections. However, it is inconsistent that the back flange of Sample 1, which has a large amplitude ridge and valley, has a first bifurcation that did not disappear due to the large imperfections. It is also inconsistent that the front flange of Sample 2, which has no local imperfections similar to the back flange of Sample 2, does not have a first bifurcation, as seen in Fig. 3.13c.

When comparing Fig. 3.12 and Fig. 3.13, the two-cure longeron has a higher

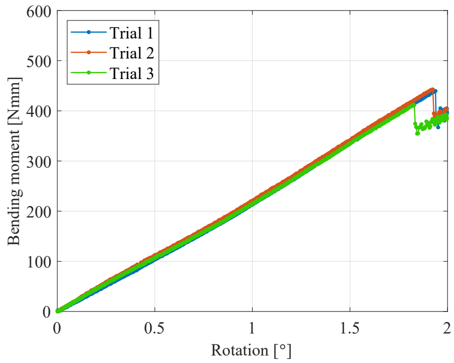

(a) Front flange in compression, Sample 1

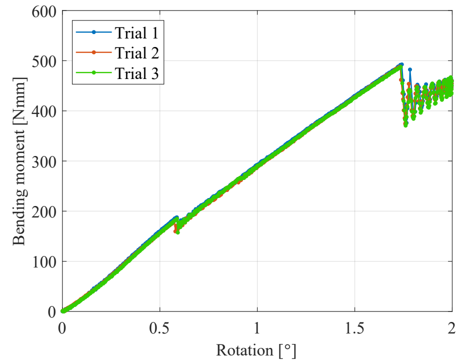

(b) Back flange in compression, Sample 1

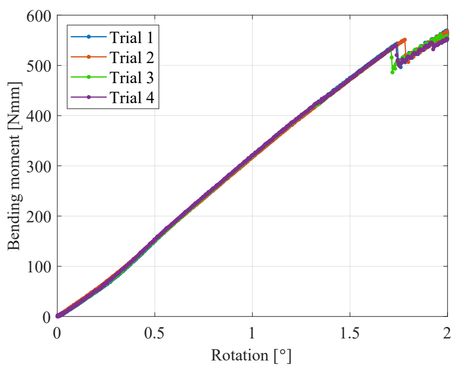

(c) Front flange in compression, Sample 2

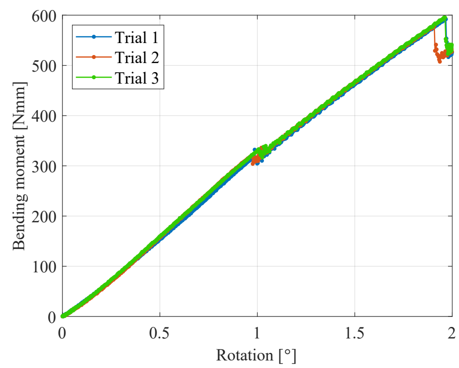

(d) Back flange in compression, Sample 2

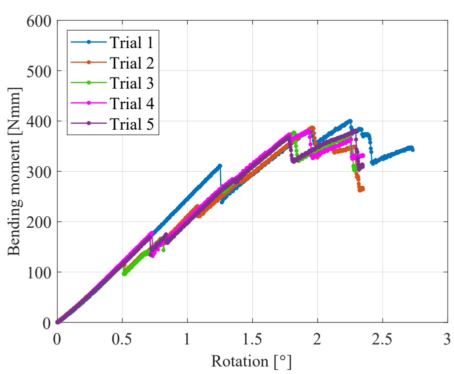

(e) Front flange in compression, Sample 3

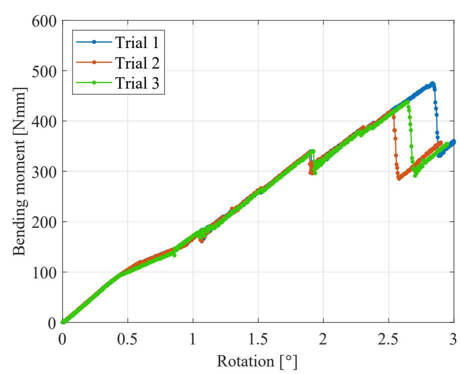

(f) Back flange in compression, Sample 3

Figure 3.13: Magnitude of bending moment-rotation curves for one-cure longerons.

bending stiffness than any of the one-cure longerons, showing that the higher quality two-cure manufacturing process improves the longeron's structural properties. Comparing the one-cure longerons in Fig. 3.13, Sample 2, which has the least imperfections, has the highest bending stiffness. On the other hand, Sample 3, which has the most imperfections, has the lowest bending stiffness. This suggests that imperfections effect the longeron's structural properties in addition to its stability.

Table 3.5 shows the mean magnitude of the second critical buckling moment and rotation taken over all trials for each flange in compression for each experimental longeron. It also shows the knockdown factor which was calculated using the ratio of the mean experimental second critical moment to the second critical moment of the numerical perfect longeron. The second critical buckling load was chosen since most of the experimental longerons do not have a first bifurcation. When looking at the one-cure longerons in Table 3.5, the knockdown factor is higher when the back flange was in compression than when the front flange was in compression. This may be because the subtended angle and arc length of the back flange is larger than that of the front flange, which increases its stability, though more research is needed to confirm this hypothesis.

Table 3.5: 2nd Critical Moments and Rotations for Experimental Longerons
Experimental values are written with mean ± std.

Sample	**Flange in Compression**	**|Crit. Moment|** [Nmm]	**|Crit. Rotation|** [°]	**Knockdown Factor**
	Num. Perfect	523	1.55	—
2 cures	Front	514 ± 9	1.36 ± 0.01	0.98
	Back	435 ± 4	1.13 ± 0.03	0.83
Sample 1, 1 cure	Front	432 ± 16	1.90 ± 0.06	0.82
	Back	489 ± 3	1.737 ± 0.004	0.94
Sample 2, 1 cure	Front	542 ± 8	1.74 ± 0.03	1.04
	Back	588 ± 9	1.95 ± 0.03	1.12
Sample 3, 1 cure	Front	N/A	N/A	N/A
	Back	339 ± 4	1.91 ± 0.01	0.65

As seen in Table 3.5, Sample 2, which has no significant local imperfections, has the highest knockdown factor with values over 1 for both flanges. The next highest knockdown factor of 0.98 occurred when the front flange of the two-cure longeron was in compression. It is interesting that the back flange of the two-cure longeron has a lower knockdown factor than the front flange even though it has a smaller amplitude dimple than the front flange. A potential explanation for this will be proposed in the next section. The lowest knockdown factor of 0.65 occurred when the back flange of Sample 3 (which has a large amplitude ridge and valley) was in compression. Of the longerons tested, only the front flange of Sample 3 has the more imperfections. However, the mean critical moment and rotation for the front flange of Sample 3 could not be computed due to the multiple bifurcations and poor agreement between the five trials, as seen in Fig. 3.13e, which made it difficult to determine the critical buckling load. This chaotic buckling behavior was likely caused by the very large imperfections. These results show that in general, the knockdown factor is higher when there are less imperfections and lower when there are more imperfections, as expected.

Figure 3.14 shows a few examples of the buckled shapes of the experimental longerons after the second bifurcation. The shapes of all other longerons are included in Appendix A.2. The edges of the longerons were highlighted in silver to make the buckles more visible. All of the buckles formed on the edge of the flange in compression, and in most cases, were outwards and occurred at the locations of the imperfections, similar to the numerical results. As seen in Fig. 3.14a, an inward valley-shaped buckle formed at the location of the valley on the back flange of Sample 1 (left side of the figure), an outward buckle formed immediately to the right of the valley, at the location of the ridge, and a large outward buckle formed at the axial center of the longeron. Another example is shown in Fig. 3.14b where a large amplitude outward buckle formed at the location of the large ridge on the front flange of Sample 3. The dimples seen lower in the image near the flange-web boundary are delaminated regions that were caused by the one-cure manufacturing process.

(a) Back flange in compression, One-cure, Sample 1

(b) Front flange in compression, One-cure, Sample 3

Figure 3.14: Example of buckled shapes of experimental longerons after 2nd bifurcation.

3.7 Comparison of Experimental and Numerical Results

To validate the numerical model, whose results were presented in Section 3.5, the experimental and numerical results were compared. The experimental results for the two-cure longeron and one of the one-cure longerons were compared to numerical results of longerons modeled with similar imperfections, described by the simple shape functions defined in Section 3.3.

Comparison to Two-Cure Longeron

This part of the work began by comparing the experimental results for the two-cure longeron to the numerical results from a model of a longeron that had the same type of imperfection with approximately the same amplitude and size as the dominant imperfections measured on the two-cure longeron. Since the mean geometric parameters of the two-cure longeron were very close to the nominal parameters, these parameters continued to be used in the numerical model. A dimple was the dominant imperfection on both flanges of the two-cure longeron, as mentioned in Section 3.6. Therefore, a numerical longeron was created with a dimple imperfection on the edge of each flange. Both dimples were located in the axial center of the longeron and had $L_z = 100$ mm and $L_\theta = 20$ mm, which is shorter than the experimental imperfections, but on the same order of magnitude. The dimple on the front flange had an amplitude of 0.5 mm, and the dimple on the back flange had an amplitude of 0.3 mm, which is the same as the experimental imperfections.

The magnitude of the experimental and numerical bending moment-rotation curves when each flange was loaded in compression are compared in Fig. 3.15. Since there was good agreement between the experimental trials, the mean of the three trials for each flange is shown. The moment-rotation curve for the numerical perfect longeron is also included in the plots for reference. When the front flange was in compression, the numerical model with the dimple imperfection had almost exactly the same bending stiffness and second critical buckling moment and rotation as the experimental longeron, as seen in Fig. 3.15a. Both the experimental and numerical longerons lack a first bifurcation but are stiffer than the perfect longeron in the post-buckling regime, likely because of the fairly large amplitude dimple.

When the back flange was in compression, the numerical model was slightly stiffer than the experimental longeron and had a slightly higher second critical buckling moment and rotation, as seen in Fig. 3.15b. This could be because the size and axial location of the numerical imperfection is different from that of the actual experimental imperfection. However, the shape of the experimental and numerical curves is the same, with both lacking a first bifurcation, and there is only an 8% difference between the knockdown factors of the experimental and numerical longerons. Additionally, when the back flange of the numerical longeron was in compression, the knockdown factor is lower than when the front flange was in compression, which is also seen in the experimental results (see Table 3.5). This may be because a dimple imperfection opposes buckling, which naturally occurs in the outward direction, so the larger amplitude dimple in the front flange increases stability.

For both flanges, the simulation could not converge much past the second bifurcation, despite the experimental curves restabilizing and continuing to a third bifurcation at a higher critical moment before losing stability. This shows that the second bifurcation is not necessarily the end of the longeron's stable regime, as suggested by the numerical results. Overall, the agreement between the experimental and numerical results for both flanges is very good, which helps validate the numerical model and the method of using simplified shape functions to model the imperfections measured in experimental longerons.

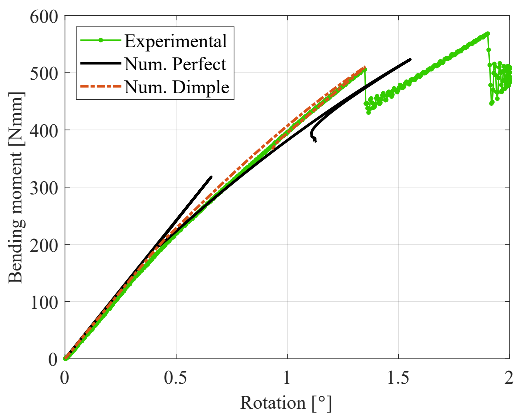

(a) Front flange in compression

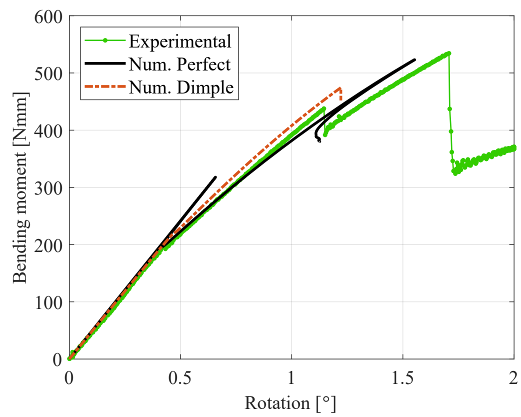

(b) Back flange in compression

Figure 3.15: Comparison of magnitude of experimental and numerical bending moment-rotation curves for two-cure longeron.

Comparison to One-Cure Longeron

Sample 1 was chosen for the comparison of a longeron manufactured with one cure to the numerical model. Since the one-cure longerons had mean geometrical parameters that were significantly different from nominal, a numerical longeron with the same radius and subtended angle as each flange of Sample 1 was modeled. The front flange was modeled with a radius of 12.34 mm and subtended angle of 131.5°, and the back flange had a radius of 12.41 mm and subtended angle of 135.2°. Initially, the model was created with a single imperfection in each flange, which was based on the largest amplitude imperfection measured on each flange of Sample 1, similar to the model resembling the two-cure longeron discussed above. An axially centered valley was created on the front flange with A = 1.1 mm and L_z = 100 mm, and an axially centered ridge with A = 0.9 mm and L_z = 100 mm was created on the back flange. However, the resulting bending moment-rotation curves were much stiffer and had a much higher second critical buckling moment than the experimental results, both when the front flange was in compression and when the back flange was in compression.

Since the simple method of modeling the one dominant imperfection in each flange did not work, in the next iteration, the two large amplitude imperfections in each flange were modeled, using their exact length and axial location. On the front flange, a valley with $A = 1.1$ mm, $L_z = 110$ mm and $C_z = 88$ mm, and a ridge with $A = 0.5$ mm, $L_z = 70$ mm and $C_z = 178$ mm were created. On the back flange, a valley with $A = 0.8$ mm, $L_z = 91$ mm and $C_z = 70$ mm, and a ridge with $A = 0.9$ mm, $L_z = 105$ mm and $C_z = 145$ mm were created. The results of the simulation with this detailed model are shown in the orange curves in Fig. 3.16. When the front flange was in compression, numerical convergence could not be achieved much past the second bifurcation. The green curves in Fig. 3.16 show the mean of the experimental results over all trials for each flange. The moment-rotation curves of the numerical perfect longeron with the same radius and subtended angle as each flange of Sample 1 are also shown for reference. When comparing the curves for the perfect longeron in Fig. 3.16a and Fig. 3.16b, the bending stiffness and both the first and second critical buckling moments were higher when the back flange was in compression than when the front flange was in compression. This must be due to the larger radius and subtended angle of the back flange, since that is the only difference between the two flanges of the numerical perfect longeron.

As seen in Fig. 3.16, the numerical model with the detailed ridge and valley imperfections was still much stiffer and had a significantly higher second critical buckling moment than the experimental longeron, both when the front flange was in compression and when the back flange was in compression. To determine if this difference between the experimental and numerical results was due to the simple shape functions used to model the imperfections differing from the shape of the actual imperfections or not capturing interactions between the imperfections, a model was created with the full set of radial imperfections measured in Sample 1. This was done by interpolating the radial coordinates of the point cloud data measured by the laser scanner over the coordinates of the nodes in the numerical model. The results of this simulation that included all imperfections measured in both flanges are shown in the blue curves in Fig. 3.16.

The moment-rotations curves for the model with all imperfections are much closer to the experimental results than the curves for the model with the ridge and valley. There was only a 4.5% difference between the knockdown factors of the experimental longeron and the numerical longeron with all imperfections when the front flange was in compression and a 10% difference when the back flange was in compression. In comparison, the difference between the knockdown factors of the experimental longeron and the longeron with the ridge and valley imperfections was about 35% for each flange. However, the numerical longeron with all imperfections is still stiffer than the experimental longeron. This could be due to delaminated regions and resin buildup (which suggests that there are also resin-poor voids) observed in the one-cure longerons, or other variations in the material properties caused by the lower quality one-cure manufacturing process.

When the front flange was in compression, the shapes of the moment-rotation curves of the experimental longeron and the numerical longerons with the ridge and valley imperfections and with all imperfections are similar in that all three lack a first bifurcation and the bending moment increases monotonically up to the second bifurcation, as seen in Fig. 3.16a. Other than the bending stiffness, the key difference in the shapes of the three curves is that the experimental longeron and numerical longeron with the ridge and valley have a sharp drop in the bending moment after the second critical buckling load, while the numerical longeron with all imperfections has only a very slight decrease in the bending moment after which the moment plateaus. When the back flange was in compression, the shapes of the experimental moment-rotation curve and the curves for the two imperfect numerical longerons appear fairly similar. However, the experimental longeron has a first bifurcation, while both of the imperfect numerical longerons lack a first bifurcation due to the large amplitude imperfections, as seen in Fig. 3.16b. It is unclear why this inconsistency in the experimental results occurs. Comparing Fig. 3.16a and Fig. 3.16b, the back flange has a higher bending stiffness and critical buckling load than front flange for the experimental longeron as well for the two imperfect numerical longerons. It is reassuring that the numerical models capture this difference in behavior between the two flanges, despite not being as compliant as the experimental longeron.

These results show that when a longeron has only one dominant imperfection with low to moderate amplitude on each flange, the numerical model can simulate the behavior of the imperfect longeron very well and good agreement with experimental results can be achieved. This was exemplified by the good agreement between the experimental and numerical results for the two-cure longeron. However, if a longeron has multiple large amplitude imperfections, the method of using simplified shape functions to model the imperfections breaks down and the actual imperfections must be modeled with high fidelity.

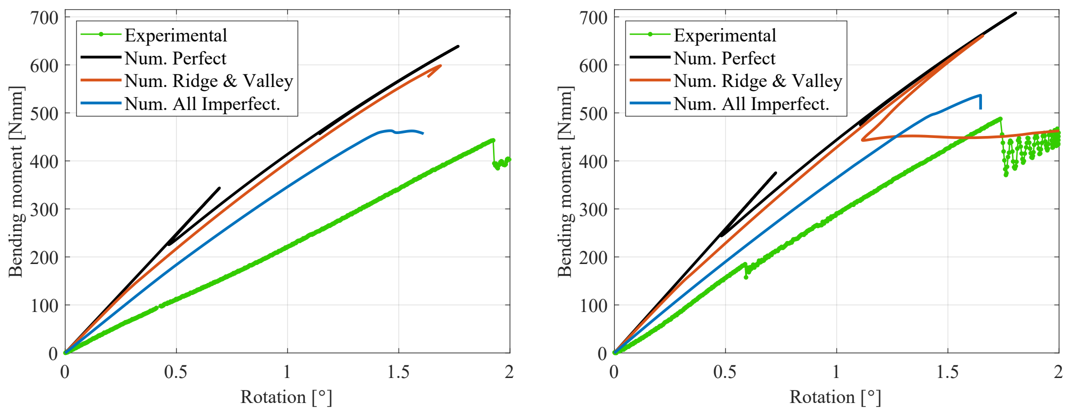

(a) Front flange in compression

(b) Back flange in compression

Figure 3.16: Comparison of magnitude of experimental and numerical bending moment-rotation curves for Sample 1 made with one cure.

3.8 Conclusion

This work presented a numerical and experimental characterization of the effects of imperfections on the knockdown factor of ultra-thin composite longerons loaded in pure bending. This is the first time that the effects of local imperfections on open cross-section thin shells has been characterized. Though open cross-section shells have the added complexity of an unsupported edge, where imperfections were shown to have the greatest effect, in many ways they behave similarly to thin-shell cylinders and spheres which have frequently been studied in the literature.

The first part of this work used finite element simulations to characterize the effect of a single local imperfection on the longeron's flange, with a wide range of varying geometric parameters. The imperfections in the numerical longeron were modeled using simple cosine based shape functions, which approximated the shape of the imperfections observed experimentally. Ridge and valley imperfections, which span the entire circumferential width of the flange, were found to have a more detrimental effect on the longeron's knockdown factor and bending stiffness than more localized bumps and dimples. Similar results were seen for cylinders where axisymmetric ring-shaped imperfections resulted in a lower knockdown factor than more localized dimple imperfections [15, 44]. Interestingly, longer imperfections, whose axial length was increased by a factor of 10 and circumferential width was increased by a factor of 2 for bumps and dimples, were more stable and had a significantly higher bending stiffness than shorter imperfections of the same amplitude. Based on the imperfections measured in the experimental longerons, these longer imperfections that have an axial length of 100 mm, and a circumferential width of 20 mm for bumps and dimples, are more realistic, while the shorter imperfections are actually unrealistically narrow. A future study that varies the imperfection size in smaller increments could be very helpful to more fully understand the effects of imperfection length and width.

Bump imperfections were shown to have a greater effect on the longeron's stability than dimple imperfections with the same amplitude and size, since bumps are in the direction in which the longerons naturally buckle. The opposite behavior was seen for hemispherical shells, where dimples were found to have a lower knockdown factor than bumps with the same amplitude and size [18]. This is likely because spherical shells naturally buckle inwards, so dimples are in the direction that aids buckling while bumps oppose buckling. Therefore, these two case studies suggest that imperfections in the same direction in which a perfect structure naturally buckles are more detrimental to the structure's stability than imperfections in the opposite direction, regardless of the structure's geometry.

For all imperfection types studied, the knockdown factor and bending stiffness of the longerons decreases with increasing imperfection amplitude, which is consistent with the trend seen in literature for various different thin-shell structures [8, 9, 15, 17, 18, 44]. Additionally, when a certain large imperfection amplitude was reached, the longeron's first buckling mode was shown to disappear, resulting in the bending moment-rotation curve following a path with lower bending stiffness that approaches the post-buckling path of the perfect longeron. This phenomenon was seen in literature in both analytical and numerical studies [8, 9, 44]. Future work could include a more thorough numerical study where the imperfection amplitude is varied in smaller increments to determine the exact imperfection amplitude where the first bifurcation disappears.

In the second part of this work, the buckling behavior of experimental longerons with random manufacturing imperfections was tested. Local radial imperfections with amplitudes between three and five times the flange thickness were measured in longerons manufactured using a higher quality two-cure process, while imperfection amplitudes between five and ten times the flange thickness were measured in the longerons made using a lower quality one-cure process. When loaded in bending, the two-cure longeron had a higher knockdown factor than all the one-cure longerons, except for Sample 2 which had no significant local imperfections in either flange and had the highest knockdown factor of the tested longerons. Furthermore, the two-cure longeron had a higher bending stiffness than any of the one-cure longerons, showing that the higher quality manufacturing process improves the longerons' structural properties in addition to their stability. Among the one-cure longerons, Sample 2, which had no significant local imperfections, had the highest knockdown factor, while Sample 1, which had moderate local imperfections, had the next highest knockdown factor, and Sample 3, which had the greatest local imperfections, had the lowest knockdown factor. This trend of decreasing knockdown factor with increasing imperfection amplitude agrees with the numerical results, as well as with results in literature for other thin-shell structures.

Excellent agreement was achieved when comparing the experimental and numerical results for the two-cure longeron, which has only one dominant imperfection with moderate amplitude on each flange. However, when multiple large amplitude imperfections are present, the method of modeling the imperfections with simplified shape functions breaks down and a high fidelity model must be used, as seen with the one-cure longeron. The one-cure manufacturing process is no longer being used by the lab due to the large imperfections it introduces in the longerons and the inconsistent, but overall poor, stability and structural properties of the one-cure longerons. Therefore, the numerical model, which was validated for the two-cure longeron, can reliably be used in future studies to predict the knockdown factor of the two-cure longerons.

Another direction for future work includes measuring the pre-buckling deformation of the longerons to track the growth of the buckle before the first bifurcation as well as in the post-buckling regime between the first and second bifurcations. This would be fairly easy to do in a numerical analysis. It would be interesting to measure the amplitude and length of the buckle formed after the first bifurcation and compare the behavior of the numerical perfect longeron in the post-buckling regime to that of a longeron with an imperfection of the same geometry as the buckle. The buckled shape of experimental longerons could also be measured using a 3D laser scanner, following a method similar to the one described in Chapter 2 for measuring the longerons' geometric imperfections.

Chapter 4

EFFECTS OF VARYING CROSS-SECTIONAL PARAMETERS

4.1 Introduction

Deployable structures that can be efficiently packaged for launch and then deploy once in space are useful for large space structures, such as the booms or structural members that support large photovoltaic blankets, solar sails, and antennas. Due to their high strength to mass ratio and ability to withstand tight packaging, thin composite shells are increasingly being used for these deployable space structures [27, 29]. However, buckling is known to be one of the main failure modes of thin-shell structures, which are also very sensitive to geometric imperfections [6–8, 12, 15, 41, 44]. Imperfection sensitivity is a particularly important issue for extremely thin composite shells, which often contain manufacturing imperfections, as was shown in Chapter 2. The knockdown factor, which is the ratio of the critical buckling load of an actual imperfect structure to the buckling load of the theoretical perfect structure is a commonly used metric to quantify the effect of imperfections on a structure's stability [4].

A deployable structure of particular interest to this work is the open cross-section, ultra-thin, composite, triangular rollable and collapsible (TRAC) [32] longeron. The longeron cross section consists of two circular arc flanges connected by a straight web region, which results in the flanges being about half the thickness of the web region. The geometry of the longeron cross-section is defined by the height of the web region and the flange radius and subtended angle. For packaging, the longeron's flanges can be flattened and then the longeron can be coiled around a central hub, resulting in a smaller packaged volume for a given deployed bending stiffness than most traditional closed cross-section booms [32]. For this reason, longerons are the chosen load-bearing elements for the Caltech Space Solar Power Project (SSPP) spacecraft [31].

The open cross-section longerons have a vast design space of combinations between their web height, flange radius and flange subtended angle that has yet to be fully explored. One contribution is the work of Banik and Murphey [32] who performed a numerical analysis varying the flange flare angle of composite TRAC booms from 60° to 170°. They and showed that the boom's bending stiffness increased with increasing flange flare angle, and thus, chose a flare angle of 170° for their study to maximize the bending stiffness. Banik and Murphey also numerically studied TRAC booms with a few different flange radii loaded in bending and measured the bending stiffness and critical buckling load.

Another notable contribution is the work of Bessa and Pellegrino [49] who used a data-driven machine learning and optimization method to vary the longeron's flange subtended angle and web height and find the optimal values of these parameters that resulted in the highest critical buckling load. To study the imperfection sensitivity of different designs, Bessa and Pellegrino seeded geometric imperfections that were a combination of the first two eigenmode shapes, since imperfections in experimental longerons had not yet been measured. However, the shapes of the linear buckling modes were later found to be quite different from the shapes of actual local imperfections measured in experimental longerons, as was seen in Chapter 2. Additionally, Bessa and Pellegrino focused more on developing the data-driven methodology than on selecting the best cross-sectional geometry to be used for realistic structures. For this reason, the cross-section of the longerons used in the SSPP structure was not modified as a result of this work.

The composite longerons currently used in the SSPP structure have a flange thickness of 80 µm and a web thickness of 185 µm, which is significantly thinner than the longerons studied in Ref. [32]. These ultra-thin shells are highly prone to buckling, and all buckles form on edge of flange, as was shown in Chapter 3. Additionally, significant geometric imperfections, which are introduced during the composite manufacturing process, have been measured in the longerons and were shown to significantly decrease the longerons' stability and bending stiffness, with imperfections at the edge of the flange having the greatest effect. Since the edge of the flange is the most prone to buckling and the most sensitive to imperfections, varying the flange subtended angle has the potential to significantly effect the longeron's stability. Therefore, the present work aims to vary the longeron's flange subtended angle, α, with the goal of increasing its stability, resistance to imperfections and bending stiffness, and providing useful recommendations to improve the design of future longerons.

Since bending is the main loading expected for the SSPP structure, the longerons in this work were loaded in pure bending such that one flange was in compression and the other was in tension. This is the most interesting loading case since it resulted in the edges of the flanges, which are the most effected by the change in subtended angle, experiencing the maximum magnitude of bending moment. The flange subtended angle was varied in a range that could realistically be flattened and coiled, and the results were evaluated by measuring the bending response and critical buckling bending moments. The first part of this work preformed a numerical analysis of longerons with varying flange subtended angle, which allowed for a wider range of subtended angles and a smaller increment size. To to study the imperfection sensitivity with varying flange subtended angle, imperfections based on the shape of realistic defects measured in experimental longerons were modeled. Then, in the second part of this work, the bending and buckling behavior of experimental longerons, which have random manufacturing imperfections, with three different flange subtended angles was measured. In both the numerical and experimental studies, the knockdown factor was computed using the ratio of the critical buckling moment of an imperfect longeron to the critical moment of the numerical perfect longeron with the same flange subtended angle.

The chapter begins by describing the numerical analysis methods used to model both perfect and imperfect longerons with varying flange subtended angle, in Section 4.2. Then, the composite longeron manufacturing process and experimental methods are described in Section 4.3. The numerical and experimental results are presented and discussed in Section 4.4. Next, based on the promising results of increasing the flange subtended angle, yet the drawback of increased longeron mass, a numerical model of a longeron with a decreased radius at the edges of its flanges was created, and the bending and buckling results of this analysis are presented in Section 4.5. Finally, the chapter is concluded in Section 4.6.

4.2 Numerical Methods

Longerons loaded in pure bending about the vertical axis were modeled numerically using the Abaqus 2024 commercial finite element software. The flange subtended angle was varied from $\alpha = 90°$ to $\alpha = 135°$ in $5°$ increments, while keeping the flange radius constant at 13.6 mm, the web height at 8 mm and the longeron length at 500 mm. The same material properties, mesh, boundary conditions and all other analysis methods described below were used for all subtended angles. Both perfect longerons and longerons with a geometric imperfection were studied.

Numerical Model and Boundary Conditions

The goal of the numerical model was to simulate the experimental longerons and bending setup as closely as possible so that the experimental and numerical results could be compared. This was achieved by modeling the longerons using the material properties measured in the experimental composite longerons and by using the same boundary conditions as in the experimental bending machine, which will be described in more detail in Section 4.3. The longeron was modeled using 4-node shell elements with reduced integration and hourglass control (S4R) and a quad-dominated mesh with a side length of 0.5 mm. This mesh size was determined by refining the mesh until the critical buckling bending moment of longerons with both $\alpha = 105°$ and $\alpha = 120°$ converged. Note that this is the same numerical model that was used in Chapter 3.

The boundary conditions of the numerical model applied a rotation to the left end of the longeron to create the bending, while constraining only one of each degree of freedom, mimicking the boundary conditions of the experimental bending machine. A key element required to make the numerical results similar to the experimental ones was to model the compliance of the bending machine. This was done by modeling bending springs on each end of the longeron that were compliant only in bending about the vertical axis and whose spring constant was determined by experimentally measuring the bending stiffness of the bending machine with no test sample attached. As will be described in more detail in Section 4.3, the ends of the experimental longerons were rigidly glued into acrylic plates that could be mounted onto the bending machine. The acrylic plate on the left end of the longeron (End 1) was attached to a stiff aluminum plate, so it was assumed that this acrylic plate did not add additional compliance beyond that of the bending machine. However, the acrylic plate on the right end of the longeron (End 2) was unsupported, so its compliance was accounted for by including the plate in the numerical model. The material properties of continuous cast acrylic were used for the acrylic plate and it had the same dimensions as the experimental plates: 50 mm wide, 90.5 mm tall and 6 mm thick. A hex mesh with a side length of 2 mm and 8-node linear brick elements with reduced integration and hourglass control (C3D8R) were used to model the acrylic plate.

At the left end of the longeron, the bending spring was attached to a reference point at the centroid of the longeron cross-section (RP-1), which was connected to the nodes in the first 1.5 mm of the longeron using a multi-point beam constraint, creating a rigid end cross-section. The other end of the spring was attached to a reference point above End 1 (RP-2), where a rotational boundary condition about the vertical axis was applied and all other degrees of freedom were constrained. RP-1 was allowed to translate along and rotate about the out-of-plane axis, while vertical translation and axial translation and rotation were held fixed. The nodes in the rightmost 1.5 mm of the longeron were rigidly attached to the acrylic plate at End 2 using a tie constraint. One end of the bending spring at End 2 was attached to a reference point (RP-3) that was connected, using a coupling constraint that constrained all degrees of freedom, to a region of the acrylic plate that was approximately the size and location of the plate's connection to the bending machine. The other end of the spring was attached to a reference point above the acrylic plate that was fixed in all degrees of freedom. Vertical translation and axial translation and rotation were free at RP-3, while displacement and rotation in the out-of-plane direction were constrained.

Finite Element Analysis

The longeron was statically bent using the Riks arc-length solver in Abaqus Standard with nonlinear geometry. An initial arc-length increment of 0.05 with automatic incrementation was found to yield the best convergence. The arc-length solver was used since it computes the structure's pre-buckling path, critical buckling load and post-buckling path, i.e. the entire equilibrium curve, in a single step.

To achieve convergence of the arc-length solver past the first bifurcation, a very small bump imperfection with an amplitude of 5 µm (or 5% of the flange thickness) was introduced on the edge of the flange in compression, using the method described in the following Subsection. For all flange subtended angles, the first critical buckling load of the longeron with the small amplitude bump was within 5% of that of the perfect longeron and the buckled shapes of the perfect and slightly imperfect longerons after the first bifurcation were the same. Therefore, the slightly imperfect longerons were used in place of perfect longerons, for which post-buckling convergence could not be achieved, and in Section 4.4 below, when referring to perfect longerons, the results of the slightly imperfect longerons will actually be shown instead.

Model of Geometric Imperfection

In order to study the effect of flange subtended angle on the longeron's imperfection sensitivity, a geometric imperfection similar to the ones introduced during the manufacturing of experimental longerons was modeled on the numerical longerons. Based on the work in Chapters 2 and 3, where the geometric imperfections present in experimental longerons and their effect on the longeron's bending and buckling behavior were measured, the chosen imperfection was a bump on the edge of the longeron's flange that would be in compression once bending was applied.

To create a purely geometrical imperfection with no initial stress, which most closely simulated the manufacturing imperfections in experimental longerons, two separate models, both with the same geometry, material properties and mesh were used. In the first model, the imperfection was created by applying a displacement boundary condition to a semi-elliptical region at the edge of the flange where the bump was located and using Abaqus' static general solver to compute the shape of the imperfection. Then, the nodal displacements were saved and imported into the second model using the *Imperfection command in the second model's input file. Since only the nodal displacements were imported into the second model, it had the geometry of the imperfection but no initial stress. The bending and buckling behavior of the imperfect longeron was then computed in the second model by applying the boundary conditions and using the arc-length solver as described above.

In the first model's imperfection region, the displacement boundary condition was defined by a displacement field applied normal to the flange and described by a shape function, which approximated the shape of the imperfections observed experimentally. To ensure that the displacement would always be normal to the flange, it was simplest to use a shape function in circumferential coordinates where the radial displacement, Δr, was a function of the axial, z, and circumferential, θ, coordinates. The origin of the circumferential coordinate system in the in-plane direction was at the center of the circle formed by the arc of the flange on which the imperfection was created, and at the left end of the longeron in the axial direction. The shape function describing the bump imperfection was a single period of a cosine wave surface in both the z and θ directions:

$$\Delta r(z,\theta) = 0.25A\left(\cos\left(\frac{2\pi(z-C_z)}{L_z}\right)+1\right)\left(\cos\left(\frac{2\pi R(\theta-C_\theta)}{L_\theta}\right)+1\right)$$
$$\text{for } z \in \left[C_z - \frac{L_z}{2}, C_z + \frac{L_z}{2}\right] \text{ and } \theta \in \left[C_\theta - \frac{L_\theta}{2R}, C_\theta + \frac{L_\theta}{2R}\right], \text{ with } \Delta r = 0 \text{ otherwise} \tag{4.1}$$

where A is the imperfection amplitude, C_z and C_θ are the coordinates of the center of the imperfection, L_z is the length of the imperfection in the z-direction, L_θ is the arc length of the imperfection in the θ-direction, and R is the flange radius. The cosine function was translated by one so that the maximum amplitude would be at the center and the value and first derivative at the edges would be zero.

In all cases throughout this chapter, the bump imperfection was axially centered on the longeron, $C_z = 250$ mm, and circumferentially centered on the edge of the flange, $C_\theta = \alpha$, since it was shown in Chapter 3 that edge imperfections had the greatest effect on stability. Bumps of two different sizes were modeled. One bump had approximately the mean dimensions of the imperfections measured in the experimental longerons: an axial length of $L_z = 100$ mm and a circumferential arc length of $L_\theta = 20$ mm. The other shorter bump had an axial length of $L_z = 10$ mm and a circumferential arc length of $L_\theta = 10$ mm, since an imperfection of this size was shown in Chapter 3 to have a more detrimental effect on the longeron's stability so it will give a good measure of the longerons' imperfection sensitivity. Since both bumps were centered on the edge of the flange, they had a semi-elliptical footprint with only half their circumferential arc length actually on the flange. For both bumps, the imperfection amplitude was $A = 0.5$ mm, which is approximately the mean amplitude of the imperfections measured in the experimental longerons.

4.3 Experimental Methods

The bending and buckling behavior of experimental longerons with three different flange subtended angles, 105°, 120° and 135°, was measured. Similar to the longerons in the numerical model, the experimental longerons all had a nominal flange radius of 13.6 mm and web height of 8 mm and were all 500 mm long. The longeron manufacturing process as well as the experimental bending setup and procedure are presented in the following sections.

Longeron Manufacturing

For all longerons, the flanges were 80 µm thick and the web region was 185 µm thick. The flanges and web had the layup $[\pm 45_{GFPW}/0_{CFUD}/\pm 45_{GFPW}]$ and $[\pm 45_{GFPW}/0_{CFUD}/\pm 45_{3,GFPW}/0_{CFUD}/\pm 45_{GFPW}]$, respectively. CFUD represents a 30 µm thick unidirectional layer of Mitsubishi Chemical's Pyrofil MR 70 12P carbon fiber and GFPW represents a 25 µm thick plain weave scrim glass ply. Both the carbon fiber and scrim glass plies were impregnated with North Thin Ply Technology's ThinPreg 415 resin, and the complete $[\pm 45_{GFPW}/0_{CFUD}/\pm 45_{GFPW}]$ stack was supplied by North Thin Ply Technology.

The longerons were manufactured using an autoclave two-cure process where the three-ply preimpregnated laminates for the two flanges were first cured individually on U-shaped aluminum molds with a radius of 12.7 mm. After the flanges were cured, a single ply of ±45 GFPW was added to the web region of one of the molds, and the two molds were clamped together and cured for a second time to bond the flanges. When the longeron was removed from the mold after the second cure, the flanges sprang back to a nominal radius of 13.6 mm, due to residual stress from cooling at the end of the curing cycle. Finally, the flanges were temporarily flattened and cut to the arc length associated with the desired subtended angle. Excess material at the bottom of the web region was also cut to a nominal web length of 8 mm. More details about the manufacturing process are described in [38].

In this work, for uniformity, all three longerons were manufactured from one approximately 1,500 mm long longeron. After removing the longeron from the mold, it was cut into three 500 mm long test samples. The flanges of the first shorter longeron were cut to a nominal arc length of 25 mm, which resulted in a nominal subtended angle, α, of 105°. The other two longerons were cut to arc lengths of 28.5 mm and 32 mm, corresponding to nominal flange subtended angles of $\alpha = 120°$ and $\alpha = 135°$, respectively. To mount the longerons onto the bending machine, the ends of each longeron were rigidly glued into 50 mm wide, 90.5 mm tall and 6 mm thick acrylic end plates. For each end of each longeron, a thin slit matching the exact cross section of that end, which was measured using the method described in Chapter 2, was laser cut through about three quarters of the thickness of the corresponding acrylic plate. Then, each end of the longeron was fitted into the slits and epoxied. This formed a rigid connection between the longeron and the end plates, which allowed the bending machine's loading to be applied directly to the longeron.

Experimental Setup and Procedure

A specially designed bending machine [45] was used to load each longeron in as close as possible to pure bending about the vertical axis. The bending machine constrained only one of each degree of freedom, to ensure that there was no self stress in the test sample, while air bearings, sliders and counterweights allowed the sample to move freely in the degrees of freedom that were not constrained. A Harmonic Drive FHA-8C DC motor applied a rotation about the vertical axis to the left end of each longeron. The applied rotation was measured by an incremental encoder with a resolution of 4.5×10^{-4} degrees. End 1 was allowed to freely translate and rotate in the out-of-plane direction, while being held fixed in translation along the vertical axis and in both translation and rotation in the axial direction. The right end of each longeron was allowed to freely translate along the vertical axis and translate and rotate in the axial direction, while out-of-plane translation and rotation and rotation about the vertical axis were held fixed. Forces and moments in all three directions were measured by ATI Mini40 load cells at each end of the longeron to record the bending moment about the vertical axis and verify that all of the other forces and moments were negligibly small. These load cells have a resolution of 1/100 N for the three force components and a resolution of 1/4000 Nm for the three moment components.

To perform a bending test, a longeron was mounted onto the bending machine by screwing the acrylic plate on End 1 of the longeron onto a stiff aluminum plate on the left side of the bending machine and the acrylic plate on End 2 of the longeron onto a vertical slider on the right side of the bending machine. To balance the vertical force due to gravity and allow the vertical slider to move freely, a counter mass equaling half the mass of the longeron test sample plus the mass of the translating part of the vertical slider was attached to the acrylic plate on End 2 through a low-friction pulley. After mounting the longeron, a rotation of positive 2° was applied to create compression in the front flange, and the bending moment and rotation were measured. Once the locations of any buckles on the front flange were noted, a rotation in the opposite direction was applied to bring the longeron back to its unloaded condition. The longeron was left unloaded for one to two hours to allow any residual moment caused by hysteresis during the unloading to dissipate. Then, a rotation of negative 2° was applied to create compression in the back flange. After all data was saved, the longeron was unloaded by applying a rotation in the opposite direction. This was repeated for 3 to 4 trials for each of the three longerons.

4.4 Results of Varying Flange Subtended Angle

This section presents the results of the numerical and experimental studies of longerons with varying flange subtended angle loaded in pure bending. The behavior of both perfect and imperfect longerons with flange subtended angle varying from $\alpha = 90°$ to $\alpha = 135°$ was computed using the numerical methods described in Section 4.2. Then, three experimental longerons with different subtended angles, 105°, 120° and 135°, were tested following the procedure described in Section 4.3.

Numerical Results

The bending moment-rotation curves for selected flange subtended angles are shown in Fig. 4.1. The curves for perfect longerons are shown in Fig. 4.1a. Fig. 4.1b shows the moment-rotation curves for imperfect longerons with a bump imperfection whose dimensions were based on the lengths of the defects measured in experimental longerons: $L_z = 100$ mm and $L_\theta = 20$ mm. This imperfection will be referred to as the "100 mm bump" throughout this section. Finally, Fig. 4.1c shows the curves for imperfect longerons with a shorter bump imperfection (L_z = 10 mm and L_θ = 10 mm) that was previously shown to have a more detrimental effect on the longeron's stability. This shorter bump will be referred to as the "10 mm bump". Both types of bumps had an amplitude of 0.5 mm, and were axially centered on the longeron and circumferentially centered on the edge of the flange loaded in compression.

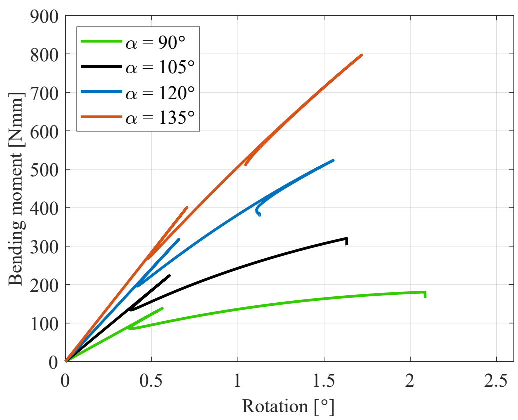

(a) Perfect

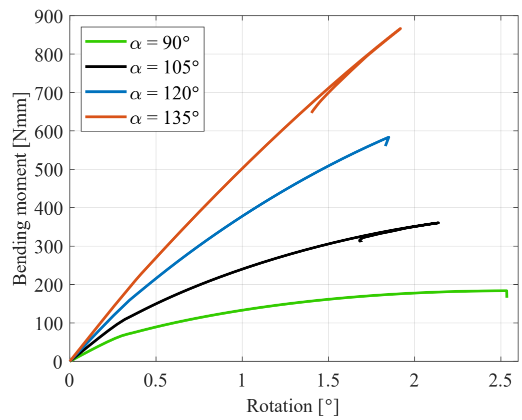

(b) 100 mm bump

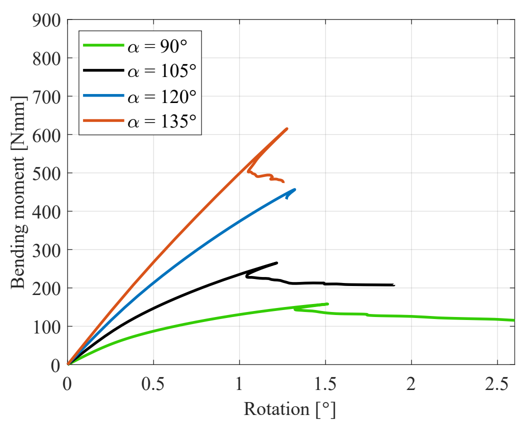

(c) 10 mm bump

Figure 4.1: Bending moment-rotation curves for perfect and imperfect longerons with varying flange subtended angle.

For the perfect longerons, the general shape of the curves is similar for all subtended angles, as seen in Fig. 4.1a. At all subtended angles, the moment-rotation curves are linear before the first bifurcation, which is denoted by the first local maximum in the bending moment. This is expected since the longerons behave linear elastically below the critical buckling load. After the longerons buckle, the bending moment decreases sharply, closely following the initial loading curve for all subtended angles. Then, a local minimum is reached, the longerons restabilize and the moment and rotation increase again following a post-buckling path with lower bending stiffness than the initial loading curve for the respective subtended angle. Finally, a second bifurcation is reached, denoted by the second local maximum in the moment, after which the longerons cannot regain stability and the simulations can no longer converge. It is important to note that for all subtended angles the perfect longerons restabilize in the post-buckling regime after the first bifurcation and buckling failure occurs after the second bifurcation.

A significant difference between the curves for different flange subtended angles is that the bending stiffness increases with increasing subtended angle. For perfect longerons, the bending stiffness was measured in the initial linear region before the first bifurcation and is plotted as a function of subtended angle in Fig. 4.2 and listed in Table 4.1. The trend of increasing stiffness with increasing subtended angle makes sense because a longeron with a larger subtended angle has a greater second moment of area, I, so the bending stiffness, EI, will be greater. As seen in Fig. 4.2, the bending stiffness increases nonlinearly, with the stiffness increasing less at higher subtended angles. This is explained by Equation 2.7 in Ref. [50] which shows that the bending stiffness of the longeron cross-section depends on a linear α term as well as a $-\sin(\alpha)$ term that increases and a $\sin(\alpha)\cos(\alpha)$ term that decreases with increasing α, for α between 90° and 135°.

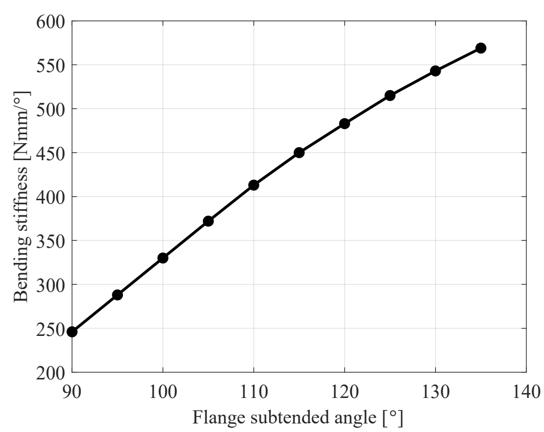

Figure 4.2: Bending stiffness of perfect longerons vs. flange subtended angle.

The bending stiffness in the post-buckling regime is harder to quantify since it is nonlinear. However, looking at Fig. 4.1a, it can be qualitatively observed that for the longeron with $\alpha = 90°$ (green curve) the post-buckling path has a significantly lower bending stiffness than the initial loading curve, while for the longeron with $\alpha = 135°$ (orange curve) the post-buckling path is only slightly more compliant than the initial loading curve. This means that the first bifurcation has less effect on longerons with a larger subtended angle than on longerons with a smaller subtended angle, which is a very desirable quality since it suggests that structures containing longerons could operate in the post-buckling regime with only a minor decrease in stiffness.

For the imperfect longerons with both bump lengths, the bending moment-rotation curves at all subtended angles do not have a bifurcation below the first critical buckling moment of the perfect longeron with the same respective subtended angle, as seen in Fig. 4.1b and 4.1c. Instead the curves follow the stable post-buckling path of the respective perfect longeron and have about the same bending stiffness as the perfect longeron in the post-buckling regime. This is because the imperfection decreases the first critical buckling load so much that a first bifurcation does not occur and the longeron immediately follows the perfect longeron's post-buckling path, as was discussed in Chapter 3. For this reason, the bifurcation that does occur for the imperfect longerons will be referred to as the second bifurcation and the critical moment will be compared to the perfect longerons' second critical moment when computing the knockdown factor. Though the simulations continue converging after the second bifurcation in a few cases, for all subtended angles the imperfect longerons cannot regain stability after the bifurcation, similar to the perfect longerons. Additionally, since the imperfect longerons follow the perfect longerons' post-buckling path, the trend of increasing bending stiffness with increasing subtended angle discussed above for the perfect longerons in the post-buckling regime applies to the imperfect longerons with both bump lengths as well.

At all subtended angles, the moment-rotation curves for the longerons with the longer 100 mm bump continue past the second bifurcation of the perfect longeron with the same respective subtended angle and have a higher second critical buckling moment and rotation, as seen when comparing Fig. 4.1a and 4.1b. The difference between the second critical moment of the imperfect longeron and that of the perfect longeron with the same subtended angle increases with increasing subtended angle. For example, for $\alpha = 90°$, the second critical moment of the imperfect longeron is only slightly higher than that of the perfect longeron; while for $\alpha = 135°$, the critical moment of the imperfect longeron is significantly higher. Additionally, the moment-rotation curves for the longerons with the 100 mm bump are nonlinear and have a softening response with increased applied rotation at all subtended angles. This softening is particularly pronounced at large rotations in the region beyond the perfect longeron's second bifurcation, and is significant at smaller subtended angles but fairly slight at larger α.

In contrast to the results for the longerons with the 100 mm bump, at all subtended angles, the longerons with the shorter 10 mm bump have a significantly lower second critical buckling moment and rotation than the perfect longeron with the same respective subtended angle, as seen when comparing Fig. 4.1a and 4.1c. This is the more traditional result expected for imperfect shells with fairly large amplitude imperfections.

Figure 4.3 shows the first and second critical buckling bending moments for the perfect longerons, as well as the second critical moment for the imperfect longerons with both bump lengths, plotted as a function of flange subtended angle. The values of the critical moments are also listed in Table 4.1 for the perfect longerons and in Table 4.2 for the imperfect longerons. For the perfect longerons, the first critical buckling moment (blue curve in Fig. 4.3) increases almost linearly with increasing flange subtended angle, while the second critical moment (black curve) increases much faster. This means that at larger subtended angles, bending moments much larger than the first critical moment can be reached in the stable post-buckling regime. Additionally, this shows that increasing the subtended angle has a greater affect on the second critical moment than on the first, which is significant since buckling failure occurs after the second bifurcation so the second critical moment is more important.

The second critical moment for the imperfect longerons with the 100 mm bump (green curve in Fig. 4.3) increases smoothly with increasing flange subtended angle, following a curve similar to that of the perfect longeron's second critical moment. At a given subtended angle, the second critical moment for the imperfect longeron is higher than that of the perfect longeron, and the difference between the moments increases with increasing subtended angle, as discussed above. This means that although the imperfect longerons lack a first bifurcation, the longer bump imperfection actually improves the longeron's stability in the post-buckling regime, especially for larger flange subtended angles.

Since the imperfect longerons with the 100 mm bump have a higher second critical moment than the perfect longeron, the knockdown factor is greater than one at all subtended angles, as shown if Fig. 4.4a and listed in Table 4.2. At smaller subtended angles, the knockdown factor increases with increasing subtended angle, as expected. However, a plateau is reached at $\alpha = 105°$, and for $\alpha > 115°$, the knockdown factor decreases with increasing flange subtended angle. This means that although the imperfect longeron's second critical moment increases with increasing flange subtended angle, it increases proportionally less than the perfect longeron at large subtended angles. This result is not particularly meaningful since the critical moment for the imperfect longerons still increases significantly with increasing subtended angle and remains higher than that of the equivalent perfect longeron. Therefore, the conclusion is that the longeron's stability increases with increasing flange subtended angle for both perfect longerons and longerons with realistic imperfections.

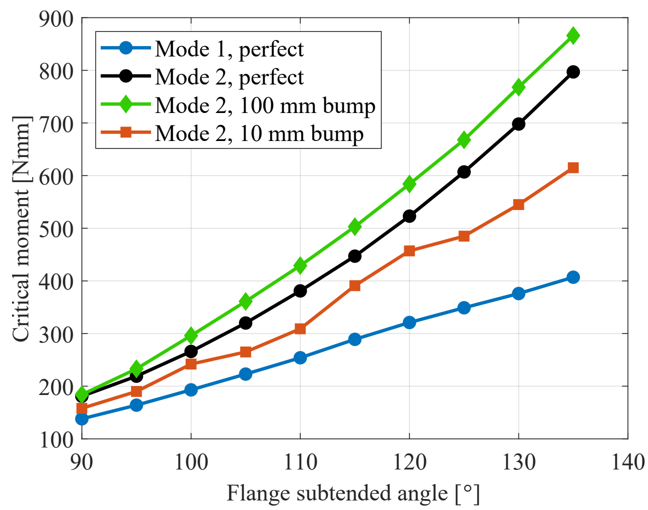

Figure 4.3: Critical buckling moments vs. flange subtended angle for perfect and imperfect longerons.

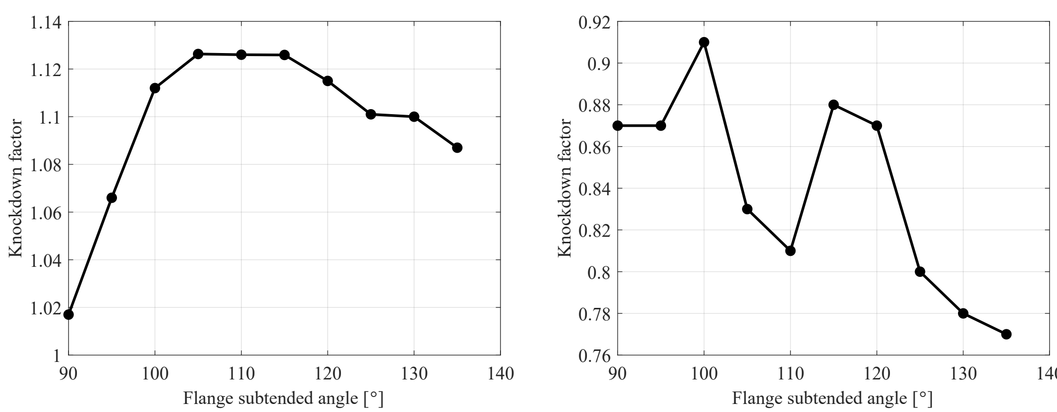

(a) 100 mm bump

(b) 10 mm bump

Figure 4.4: 2nd mode buckling knockdown factor vs. flange subtended angle for both bump lengths.

For the imperfect longerons with the shorter 10 mm bump, the second critical moment (orange curve in Fig. 4.3) increases with increasing flange subtended angle

Table 4.1: Bending Stiffness and Critical Buckling Moments for Perfect Longerons with Varying Flange Subtended Angle

Subtended Angle [°]	Bending Stiffness [Nmm/°]	1st Crit. Moment [Nmm]	2nd Crit. Moment [Nmm]
90	246	138	181
95	288	164	219
100	330	193	266
105	372	223	320
110	413	254	381
115	450	289	447
120	483	318	523
125	515	349	607
130	543	376	698
135	569	407	797

Table 4.2: 2nd Critical Buckling Moment and Knockdown Factor for Longerons with Bump Imperfections as Flange Subtended Angle Varies

	100 mm Bump		10 mm Bump	
Subtended Angle [°]	Crit. Moment [Nmm]	Knockdown Factor	Crit. Moment [Nmm]	Knockdown Factor
90	184	1.02	158	0.87
95	233	1.07	190	0.87
100	296	1.11	242	0.91
105	361	1.13	265	0.83
110	429	1.13	309	0.81
115	503	1.13	391	0.88
120	584	1.12	457	0.87
125	668	1.10	485	0.80
130	768	1.10	545	0.78
135	866	1.09	615	0.77

but does not increase uniformly, resulting in a fairly wavy curve. The second critical moment for these imperfect longerons is lower than that of the perfect longerons at all subtended angles, as discussed above. For subtended angles less than 120°, the critical moment for the imperfect longerons generally follows the trend of the perfect longerons' second critical moment. Then for subtended angles greater than 120°, the critical moment of imperfect longerons increases less with increasing subtended angle than that of the perfect longerons. This is reflected by the knockdown factor, shown in Fig. 4.4b as a function of subtended angle and listed in Table 4.2, decreasing for subtended angles greater than 120° and suggests that after a certain subtended angle the longerons become more sensitive to these narrow imperfections. The other local maximum in the knockdown factor at $\alpha = 100°$ and local minimum at $\alpha = 110°$ are interesting, and explaining this jagged behavior, that is not seen for the longerons with the longer bump, remains a subject for future work.

Experimental Results

The bending moment-rotation curves for the experimental longerons, which contained random manufacturing imperfections, with varying flange subtended angle are shown in Fig. 4.5. The results when a positive rotation was applied, resulting in a positive bending moment and the front flange being in compression are shown in Fig. 4.5a, and the results when a negative rotation was applied and the back flange was in compression are shown in Fig. 4.5b. To make the results with opposite moments and rotations easier to compare, the magnitude of the bending moment and rotation was plotted in these figures. In most cases, three trials were performed for each flange and the agreement between trials was generally very good. However, if the results differed significantly between trials, a fourth trial was performed. The mean results taken over all trials for each flange of each longeron are shown in Fig. 4.5, and the mean magnitude and standard deviation of the critical moment for each longeron, along with the knockdown factor, are listed in Table 4.3. The moment-rotation curves for the individual trials are shown in Appendix A.3.

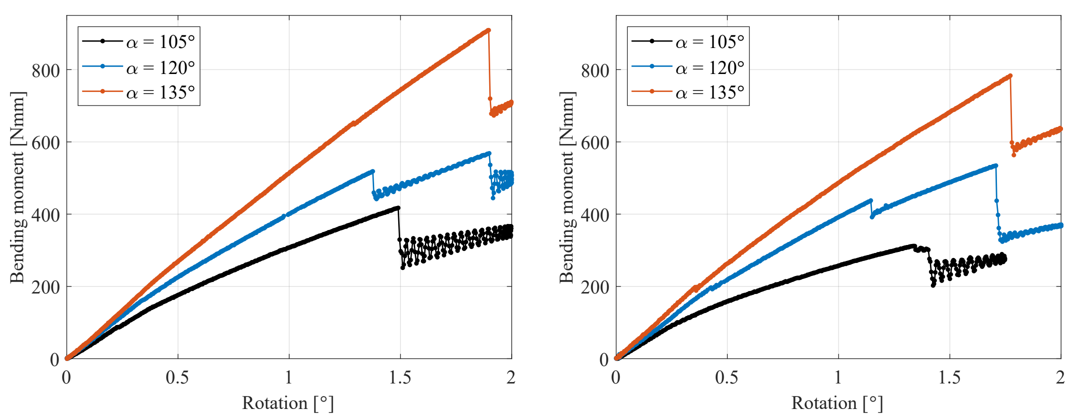

(a) Front flange in compression (b) Back flange in compression

Figure 4.5: Magnitude of bending moment-rotation curves for experimental longerons with varying flange subtended angle.

The critical buckling bending moment and rotation were determined to be the point in the moment-rotation curve where a local maximum was reached, after which the bending moment decreased sharply with increased rotation. At all flange subtended angles, when the longeron buckled, the sharp decrease in bending moment occurred at the same time that a local buckle was observed on the flange in compression. The snap of the buckle often caused the structure to oscillate on the bending machine's low friction air bearings and these oscillations are seen in some of the moment-rotation curves in Fig. 4.5 after the drop in moment. Since the experiments were rotation controlled, the magnitude of the rotation could only increase monotonically, which resulted in the experimental moment-rotation curves having a negative slope after buckling occurred and the bending moment dropped. In contrast, in the numerical moment-rotation curves, the rotation often decreased along with the moment after buckling occurred, resulting in the curve following the initial loading path, which was possible in the simulations that had no restrictions on the direction of rotation.

Similar to the imperfect numerical longerons, at all subtended angles the experimental longerons lack an initial linear region and do not have a bifurcation below the first critical buckling moment of the numerical perfect longeron with the same respective subtended angle. This means that the first observed buckle actually occurred at the second critical buckling load. The loss of the first bifurcation is likely caused by the manufacturing imperfections in the experimental longerons, which were measured in Chapter 2. For both flanges of the longeron with $\alpha = 120°$, the longeron restabilized after the second bifurcation and the moment increased up to a third bifurcation, in contrast to the numerical results where the simulation could not converge past the second bifurcation.

As seen in Fig. 4.5 and Table 4.3, both when the front flange was in compression and when the back flange was in compression, the magnitude of the second critical buckling moment increased with increasing flange subtended angle, in agreement with the numerical results for both perfect and imperfect longerons. Though the experimental longerons lack an initial linear region, making it difficult to measure the bending stiffness, it can be qualitatively observed that the bending stiffness increased with increasing subtended angle, with the longeron with $\alpha = 135°$ being the stiffest. This agreement of both trends with the numerical results helps validate the results, which demonstrate the benefits of increasing the flange subtended angle.

For all three experimental longerons, the magnitude of the critical moment was higher when the front flange was in compression than when the back flange was in compression. This was caused by the two flanges having different geometric imperfections. An example of this effect of local imperfections on the critical moment was seen when comparing the results for the numerical longerons with the

100 mm bump to those for the 10 mm bump in Fig 4.1 and 4.3. Since all three longerons were manufactured together out of the same longer longeron, it makes sense that for all subtended angles the front flange had an imperfection similar to the 100 mm bump that allowed it to continue along the post-buckling path past the perfect longeron's second critical moment, achieving a knockdown factor greater than or very close to one. On the other hand, the back flange had different imperfections that resulted in a lower second critical moment and a knockdown factor less than one in all cases. Additionally, the magnitude of the second critical moment for both flanges agrees relatively well with the numerical results for the longeron with the 100 mm bump, with the numerical results falling between the experimental results for the front and back flanges for two out of the three experimental subtended angles.

Table 4.3: Magnitude of 2nd Critical Buckling Moment for Experimental Longerons

Subtended Angle [°]	Flange in Compression	|Critical Moment| (mean ± std) [Nmm]	Knockdown Factor
105	Front	418 ± 2	1.31
	Back	310 ± 10	0.97
120	Front	514 ± 9	0.98
	Back	435 ± 4	0.83
135	Front	915 ± 6	1.15
	Back	782 ± 3	0.98

4.5 Decreased Radius at Edge of Flange

Increasing the flange subtended angle significantly improves the longeron's stability, as seen in Section 4.4, but has the drawback of increasing the amount of material, which increases the longeron's mass. Additionally, it was shown in Chapter 3 that buckles are the most likely to occur on the edge of the longeron's flange and imperfections created on the edge of the flange are the most detrimental to the longeron's stability. Therefore, this section presents and explores the idea of decreasing the radius at the edge of the flange, with the goal of improving the longeron's stability and imperfection sensitivity without adding material.

Methodology

The cross-sectional geometry of a single flange with a decreased radius at the edge is shown in Fig. 4.6. The design began with a flange that had a constant radius of 13.6 mm and subtended angle of 105° (shown in black in Fig. 4.6). Then, an arc with a radius of 6.8 mm and a subtended angle of 30° was added tangent to the edge of the constant radius flange (shown in blue in Fig. 4.6). This resulted in the new tangent to the edge of the flange being parallel to the tangent of the flange with $\alpha = 135°$. However, flange with the decreased radius has the same total arc length, and thus the same mass, as the flange with $\alpha = 120°$ and a constant radius of 13.6 mm. The edge of the flange with the decreased radius is 13.14 mm from the center of the original constant radius flange, so adding the smaller radius arc decreases the overall radius at the edge by just under 0.5 mm, which is approximately the mean amplitude of the imperfections that were measured in the two-cure experimental longerons in Chapter 2. Many other combinations of the subtended angles of the original flange and smaller radius arc, as well as the radius of the arc are possible, but the geometry discussed above is presented here to demonstrate the potential of this idea.

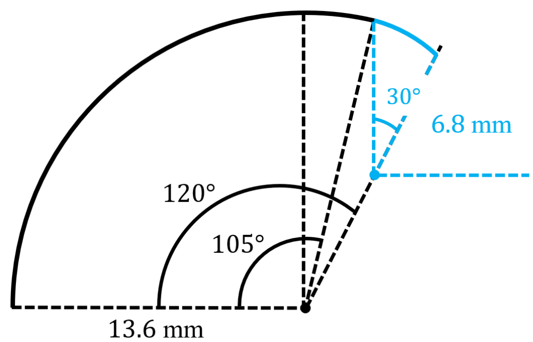

Figure 4.6: Schematic of flange cross-section with decreased radius at edge.

To study the effect of decreasing the radius on the longeron's stability and imperfection sensitivity, a numerical model of a longeron with the flange geometry discussed above was created. The boundary conditions, finite element solver and other numerical methods described in Section 4.2 were used to simulate both perfect and imperfect longerons with decreased radii at the edges of the flanges of loaded in pure bending. An imperfect longeron containing a bump imperfection with an amplitude of $A = 0.5$ mm was simulated following the method described in Section 4.2. To study the effect of an imperfection with an amplitude smaller than the amount by which the radius was decreased, a longeron with a 0.1 mm amplitude bump imperfection was modeled as well. Both bumps were axially centered on the longeron and circumferentially centered on the edge of the flange, and had an axial length of $L_z = 10$ mm and a circumferential arc length of $L_\theta = 10$ mm. This shorter bump length was used because shorter imperfections had a more detrimental effect on the stability of longerons with a constant radius, as shown in Section 4.4 and in more detail in Chapter 3. Therefore, modeling the shorter bump should give a good measure of the imperfection sensitivity of the longeron with the decreased radius.

Results

The bending moment-rotation curves for longerons with a decreased radius at the edge of the flange are shown in Fig. 4.7a and can be compared to the moment-rotation curves for longerons with a constant 13.6 mm flange radius and 120° subtended angle, shown in Fig. 4.7b, which have the same flange arc length. Both figures show curves for a perfect longeron as well imperfect longerons with 0.1 mm and 0.5 mm amplitude bump imperfections, with all other geometry being the same. Comparing the curve for the perfect longeron with a decreased flange radius (black curve in Fig. 4.7a) to the curve for the perfect longeron with a constant radius (black curve in Fig. 4.7b), it can be seen that both the first and second critical buckling moments and rotations for the longeron with the decreased radius are significantly higher than those for the longeron with the constant radius. The values of the critical moments and rotations for the perfect longerons are compared in Table 4.4. When comparing Fig. 4.7a and Fig. 4.7b, it can also be seen that the perfect longeron with the decreased radius has about the same bending stiffness as the longeron with the constant radius. This means that the longeron with the decreased radius simply continues on the same path as the longeron with the constant radius to reach a higher critical buckling moment in both the pre-buckling and post-buckling regimes.

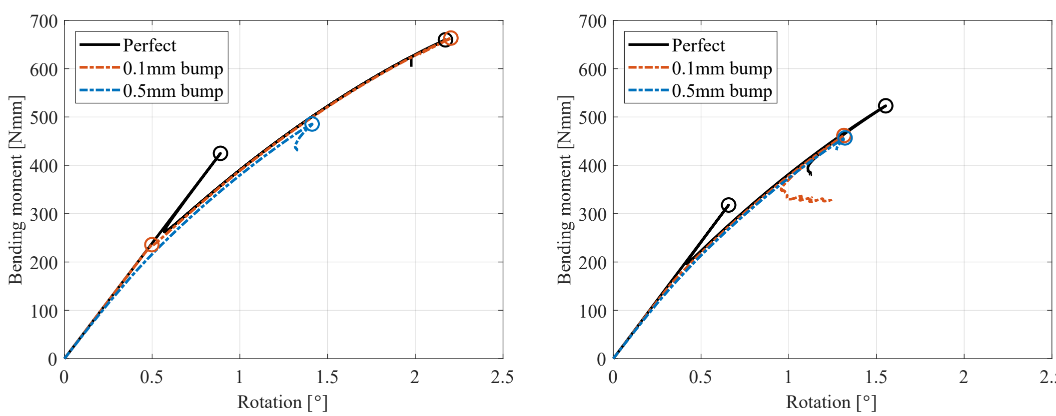

(a) Decreased radius at edge of flange

(b) Constant radius with $\alpha = 120°$

Figure 4.7: Bending moment-rotation curves for longerons with a decreased radius at the edge of the flange and varying amplitude bump imperfections compared to curves for longerons with a constant radius. The bifurcation points on all curves are circled.

The moment-rotation curve for the longeron with a decreased radius and the smaller 0.1 mm amplitude bump (dashed orange curve in Fig. 4.7a) is linear up to a first bifurcation, which has a critical moment of 236 Nmm and a critical rotation of 0.50°. However, it only has a small local maximum, meaning that the first bifurcation will disappear if the imperfection amplitude increases. Additionally, the longeron with the decreased radius and the 0.1 mm amplitude bump has about the same second critical buckling load as perfect longeron with the decreased radius, meaning that the imperfection has relatively little effect. In contrast, the constant radius longeron with same 0.1 mm amplitude imperfection immediately follows the post-buckling path of the perfect longeron with a constant radius and has a second mode knockdown factor of 0.88. The values of the second critical buckling moment and rotation and knockdown factor for the imperfect longerons with decreased radius at the edge of the flange are compared to the values for the longerons with constant flange radius in Table 4.5.

Table 4.4: Critical Buckling Moments and Rotations for Perfect Longerons with Constant and Decreased Radius

	1st Crit. Moment [Nmm]	1st Crit. Rotation [°]	2nd Crit. Moment [Nmm]	2nd Crit. Rotation [°]
Constant R	318	0.66	523	1.55
Decreased R	425	0.89	660	2.17

Table 4.5: 2nd Critical Buckling Moment and Rotation for Longerons with Constant and Decreased Radius with Varying Amplitude Bump Imperfections

	Bump Amplitude [mm]	Crit. Moment [Nmm]	Crit. Rotation [°]	Knockdown Factor
Constant R	0.1	462	1.31	0.88
	0.5	457	1.32	0.87
Decreased R	0.1	663	2.20	1.00
	0.5	486	1.41	0.74

Similar to both imperfect longerons with a constant flange radius, the longeron with a decreased radius and the larger 0.5 mm amplitude bump lacks a first bifurcation and immediately follows the post-buckling path of the perfect longeron, as seen in the dashed blue curve in Fig. 4.7a. When compared to the perfect longeron with the decreased radius, the longeron with the 0.5 mm amplitude bump has a fairly low second mode knockdown factor of 0.74. However, the value of the second critical moment for the longeron with the decreased radius and the 0.5 mm amplitude bump is higher than the second critical moment of the constant radius longerons with both the 0.1 mm and the 0.5 mm amplitude bumps, as seen in Table 4.5. Indeed, compared to the perfect longeron with the constant flange radius, the knockdown factor of the longeron with the decreased radius and the 0.5 mm amplitude bump is 0.93, which is significantly higher than the knockdown factor of either of the imperfect longerons with the constant radius. These results show that decreasing the radius at the edge of the flange results in greater stability and makes the longerons significantly more resistant to small amplitude imperfections, but also reduces the sensitivity to larger amplitude imperfections.

4.6 Conclusion

This work numerically and experimentally studied the effect of varying the cross-sectional geometry of longerons loaded in pure bending on their critical buckling load, imperfection sensitivity and bending stiffness. A finite element analysis was performed to measure the bending and buckling behavior of both perfect and imperfect longerons with a wide range of varying flange subtended angles. The numerical analysis was complimented by experimental bending and buckling tests of longerons with three different flange subtended angles. Then, based on the promising results of increasing the flange subtended angle, the radius at the edge of the flange was decreased which was shown to provide significant improvements in the longeron's stability and imperfection sensitivity without increasing its mass.

The numerical results showed that both the first and second critical buckling moments for the perfect longerons, as well as the second critical moments for imperfect longerons with both bump lengths, increase with increasing flange subtended angle. The second critical moment increases faster with increasing subtended angle than the first critical moment, which is significant since buckling failure occurs after the second bifurcation, making the second critical moment a more important value. Additionally, the bending stiffness for perfect longerons in the initial linear region before the first bifurcation increases with increasing flange subtended angle. It was also qualitatively observed that the bending stiffness after the first bifurcation decreased less for longerons with a larger subtended angle. This is significant since it means that the stiffness of the imperfect longerons, which do not have a first bifurcation and immediately follow the perfect longeron's post-buckling path, with a larger subtended angle is less effected by the loss of the first bifurcation, i.e the bending stiffness is less sensitive to imperfections at larger subtended angles.

The imperfect longerons with a 100 mm long bump, which was based on the shape of imperfections measured in experimental longerons, followed the perfect longeron's stable post-buckling path and had a higher second critical buckling moment at all subtended angles. The difference between the critical moments was greater at larger subtended angles, with the imperfect longerons having a significantly higher second critical moment than the perfect longerons at subtended angles of 120° and greater. This shows that the 100 mm bump actually increases the longeron's stability in the post-buckling regime and suggests that this type of imperfection, which exists in the current experimental longerons, may actually be beneficial. Therefore, structures using longerons with larger subtended angles, that contain this type of manufacturing imperfection, could potentially be designed to operate in the stable post-buckling regime, if the lower initial stiffness and slight softening response is acceptable.

Imperfect longerons with a shorter 10 mm bump with varying flange subtended angles were also studied numerically, since this type of imperfection was shown to have a more detrimental effect on the longeron's stability in previous work. Although this shorter bump is unrealistically narrow compared to the imperfections measured in the current experimental longerons, the results were presented in case this imperfection is encountered in future structures. The longerons with the 10 mm bump had a lower second critical moment than the perfect longerons at all subtended angles, and the curve of the knockdown factor as a function of subtended angle was fairly chaotic. To explain this behavior, future work includes studying the effect of different imperfection lengths, as well as smaller imperfection amplitudes, on longerons with varying flange subtended angle. It would also be interesting to study the effect of different types of imperfections, such as the dimple, ridge and valley described in Chapter 3. Overall, the conclusion from these numerical results is that the longerons' stability increases with increasing flange subtended angle in all cases, but the amount by which the critical moment increases is dependent on the imperfection(s) present in the longerons.

The results for the experimental longerons, which contained random manufacturing imperfections, followed the same trend of increasing critical buckling moment and bending stiffness with increasing flange subtended angle as was seen in the numerical results. The shape of the moment-rotation curves and values of the critical moments for the experimental longerons were relatively similar to the numerical results for the longerons with the 100 mm bump, with the same respective subtended angle. This agreement was expected since the 100 mm bump was based on the shape of the experimental imperfections. The differences between these experimental and numerical results are likely because the experimental longerons had dimple imperfections in addition to or instead of bumps, which effected the longeron's buckling behavior. However, the overall agreement between the experimental and numerical results was quite good.

This agreement between the experimental and numerical results validates numerical model and shows that increasing the flange subtended angle improves both the longeron's stability and structural properties. Therefore, the optimal subtended angle is the maximum angle where the longeron does not exceed the mass limit for a given application or the limit of strain where the longeron can still be flattened and coiled without cracking or other damage to the composite material. If these limits are sufficiently high, then the range of flange subtended angles that are studied can potentially be extended to angles greater than 135° in future work.

The validated numerical model was then used to measure the bending and buckling behavior of a longeron with a decreased radius at the edges of its flanges. It was shown that both the first and second critical buckling moments of a perfect longeron with a decreased radius were significantly higher than those for a longeron with a constant radius and the same arc length. Furthermore, the first critical moment of the perfect longeron with the decreased radius was higher than that of the perfect longeron with a constant radius and $\alpha = 135°$, which has a 12% longer arc length. The second critical moment of the perfect longeron with the decreased radius was almost as high as that of the perfect longeron with a constant radius and $\alpha = 130°$. This means that by decreasing the radius at the edge of the flange, the longeron's stability is increased while its mass is decreased. Additionally, it was shown that decreasing the radius at the edge of the flange significantly increases the longeron's resistance to imperfections with an amplitude smaller than the amount by which the radius at the is decreased. The decreased radius also reduces the longeron's sensitivity to larger amplitude imperfections but the improvement is less significant.

A single example of a decreased radius at the edge of the longeron's flanges was presented. However, many other combinations of the flange subtended angle and the amount by which to decrease the radius at the edge of the flange are possible, and future work includes exploring these possibilities. It would also be interesting to study the effect of varying the flange radius while keeping the radius constant throughout the entire cross-section, since this could also have a significant influence on the longeron's stability, imperfection sensitivity and structural properties.

Chapter 5

EFFECTS OF VARYING LENGTH

5.1 Introduction

Thin-shell composite booms and structural members that are lightweight and can be tightly folded or coiled into a small volume for launch and then deploy once in space are increasingly being used for extremely large space structures, such as large area photovoltaic blankets, solar sails, and antennas [27, 29]. Buckling is known to be one of the main failure modes of these thin-shell structures, which are also very sensitive to geometric imperfections [6–8, 12, 15, 41, 44]. Therefore, it is important to study the effect of length on the stability and imperfection sensitivity of composite thin-shells in order to be able to design increasingly long structures that are robust to buckling failure.

An application of particular interest to this work is the Caltech Space Solar Power Project (SSPP), which aims to generate solar power in space and wirelessly transmit the energy to Earth [31]. The load-bearing structure of the SSPP spacecraft is formed by open cross-section, ultra-thin, composite, triangular rollable and collapsible (TRAC) [32] longerons. The longeron cross section consists of two circular arc flanges connected by a straight web region, which results in the flanges being about half the thickness of the web region. The longeron's flanges are less than 100 µm thick, and these extremely thin composite shells are highly imperfection sensitive and prone to local buckling, as has been shown in previous work.

In the SSPP structure, pairs of longerons are connected with transverse rods to create ladder-type strips, which support a tensioned membrane containing photovoltaic and power transmission elements. The strips are then arranged to create the square SSPP structure, as described in Ref. [31]. The goal for the final SSPP structure is to have a side length of 60 m in its deployed configuration [31], which requires 60 m long longerons. Bending is the main load expected for the SSPP spacecraft, and buckling of the portions of the longeron in compression is a major concern. Therefore, there is substantial interest in studying bending and buckling behavior of longerons with increasing length.

Two noteworthy studies on the stability of longerons with increasing length have previously been performed. In 2020, Leclerc and Pellegrino [38] numerically studied longerons loaded in pure bending with length varying from 0.3 m to 5 m. Leclerc and Pellegrino performed both linear and nonlinear buckling analyses and found that the linear buckling simulation predicted that the critical buckling load decreased with increasing length, while the nonlinear buckling simulation predicted that the buckling load remained almost constant with increasing length. In 2022, Royer and Pellegrino [36] studied the stability of ladder-type longeron strips under pressure loading, which created bending in the strip. Royer and Pellegrino performed numerical linear and nonlinear buckling analyses on strips with length varying from 1.8 m to 4.2 m, as well as a linear buckling analysis for lengths up to 12 m, and showed that in all cases, the critical buckling load decreased with increasing strip length. Since longerons are the main component of a strip, the discrepancy between the nonlinear buckling results in Ref. [36] and [38] is interesting because one would expect to see a similar trend with increasing length in both studies. This leaves an open question of whether the critical buckling load of longerons and longeron-based structures remains constant or decreases with increasing length.

Another relevant work is that of Kosztowny et al. [51] who experimentally measured the buckling response of a 30 m long composite TRAC boom loaded in bending with gravity offloading. Kosztowny et al. found that the most frequent failure mode was local elastic flange buckling, with four distinct local buckles being observed along the length of the flange in compression at the maximum loading. However, the results were not compared to those for shorter booms, so a trend of the buckling behavior with increasing length is not apparent. Additionally, the flange thickness for the boom studied by Kosztowny et al. was 250 µm, which is about three times that of the longerons used in the SSPP structure, and the cross-sectional parameters of the boom were also quite different from those of the longerons.

In the years since the studies in Ref. [36] and [38] were performed, the cross-sectional parameters of the longerons for the SSPP structure were modified to improve their structural properties. Additionally, a different type of carbon fiber, plain weave glass fiber and epoxy resin is currently used to manufacture the composite longerons, resulting in current experimental longerons having different material properties than those studied by Ref. [36, 38]. Therefore, the current work numerically studies longerons with the updated geometry and material properties with the goal of determining their buckling behavior and imperfection sensitivity with increasing length.

This work continues that of Leclerc and Pellegrino [38] by varying the length of a single longeron loaded in pure bending and studying the buckling behavior of the side in compression. In addition to measuring their critical buckling load, this work investigates the bending stiffness, post-buckling response and realistic buckled shapes of longerons with varying length. The effect of length on the longerons' imperfection sensitivity is also studied by modeling longerons with geometric imperfections based on the imperfections measured in experimental longerons. This has not yet been studied, since the work in Ref. [36, 38] focused on perfect longerons and used an eigenvalue analysis which does not show the loading response past the first bifurcation.

In this work, the longeron length is varied from 0.5 m to 5 m, to approximately span the range of lengths studied in Ref. [38]. The study was performed only numerically, because it is impractical to work with 5 m long structures in the current laboratory setting. At this time, experimental bending and buckling tests have only been performed on longerons less than 1 m long. This work, especially the study of realistic imperfect longerons, performs the preparatory steps required for future experimental studies of longer longerons and for finding a relationship between the longeron length and its bending and buckling behavior that can be extrapolated to significantly longer longerons.

The chapter begins by describing the numerical analysis methods used to model and measure the bending and buckling response of both perfect and imperfect longerons with varying length, in Section 5.2. Then, the results of the length study are presented in Section 5.3, and discussed and compared to those in literature in Section 5.4. Finally, the chapter is concluded in Section 5.5.

5.2 Numerical Analysis Methods

To study the effect of longeron length on its bending and buckling behavior, a longeron with length varying from $L = 0.5$ m to $L = 5$ m, loaded in pure bending, was modeled numerically using the Abaqus 2024 commercial finite element software. The same longeron cross-section, material properties, mesh, boundary conditions and all other analysis methods described below were used for all lengths. Both perfect longerons and more realistic longerons with a geometric imperfection were studied.

Numerical Model and Boundary Conditions

The longeron was modeled using a flange radius of 13.6 mm, flange subtended angle of 120°, and a web length of 8 mm. These cross-sectional parameters were chosen since they are the nominal parameters of the longerons currently used for the SSPP structure. The material properties of the current experimental composite longerons, whose flanges are 80 µm thick and web region is 185 µm thick, were used to model the numerical longeron. The properties of the composite flange and web materials were determined by conducting tensile and bending tests to compute the components of the generalized stiffness matrices, A-B-D, for both the flange and web. The longeron was modeled using 4-node shell elements with reduced integration and hourglass control (S4R). A quad-dominated mesh with a side length of 0.5 mm was used to model the longeron. This mesh size was determined by refining the mesh until the critical buckling bending moment of a 0.5 m long longeron converged.

The boundary conditions used in this work closely follow those used by Leclerc and Pellegrino [38] in the case of a bending moment about the vertical, y-axis. Multi-point beam constraints were used to connect the nodes in the first 1.5 mm at each end of the longeron to a reference point at the centroid of the longeron cross-section at each end, creating rigid end cross-sections. At the left end of the longeron, a rotational boundary condition, ϕ_y, about the vertical axis was applied to the reference point (RP-1) to create bending, as shown in Fig. 5.1. Translation along the x and z-axes at RP-1 was left free, while translation along the y-axis and rotation about the x and z-axes were constrained. At the right end of the longeron, the reference point (RP-2) was fixed in all degrees of freedom, creating a clamped boundary condition. Note that these boundary conditions are different from those used in Chapters 3 and 4, and the main difference is that axial twist was constrained at both ends of the longeron in this analysis.

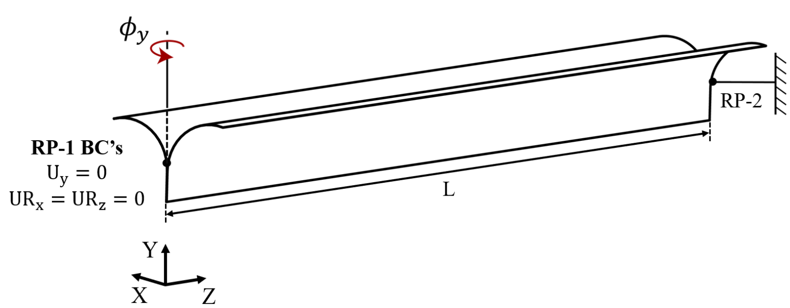

Figure 5.1: Schematic of a longeron showing the boundary conditions used in the numerical model.

Finite Element Analysis

The arc-length solver in Abaqus Standard (Static Riks) with nonlinear geometry was used to compute the longeron's bending and buckling behavior. The solver was set to use automatic incrementation with an initial arc-length increment of 0.05. The arc-length solver was used since it allows the structure's pre-buckling path, critical buckling load and post-buckling path to be computed in a single step, and clearly shows any bifurcations in the moment-rotation curve.

Initially, an iterative nonlinear eigenvalue analysis was used to compute the critical buckling load, and then the arc-length solver was used in a subsequent step to compute the post-buckling path, following the method described in Ref. [38]. However, it is preferable to compute the entire equilibrium curve at once, and the critical buckling load obtained using the arc-length solver was extremely close to that computed by the nonlinear eigenvalue analysis. Additionally, the buckled shapes computed by the arc-length solver are more realistic, compared to the buckled shape of experimental longerons, than the wave-like mode shapes predicted by the eigenvalue analysis. For these reasons, it was decided to use a single step with only the arc-length solver for all of the simulations performed in this work.

The drawback of using the arc-length solver is that it requires a slight imperfection be introduced in the perfect structure in order to achieve convergence past the first bifurcation. For this purpose, a very small bump imperfection with an amplitude of 5 µm (or 5% of the flange thickness) was created on the edge of the flange in compression, using the method described in the following Subsection. For all longeron lengths, the first critical buckling moment of the longeron with the small amplitude bump was within 5% of that of the perfect longeron, and the buckled shapes of the perfect and slightly imperfect longerons immediately after the first bifurcation were the same. Therefore, the slightly imperfect longerons were used in place of the perfect longerons, for which post-buckling convergence could not be achieved, throughout this work.

Model of Geometric Imperfection

To study the effect of length on the longeron's imperfection sensitivity, a bump imperfection was modeled on the edge of the longeron's flange that would be in compression once bending was applied. A bump was chosen since it was found to be one of the more detrimental imperfections, in Chapter 3, and the shape of the bump was similar to that of the manufacturing imperfections measured in the experimental longerons, in Chapter 2.

Two separate models, both with the same geometry, material properties and mesh were used to create a purely geometrical imperfection. In the first model, the imperfection was created by applying a displacement boundary condition to a semi-elliptical region at the edge of the flange where the bump was located and using Abaqus' static general solver to compute the shape of the imperfection. Then, the *Imperfection command in the second model's input file was used to import the nodal displacements from the first model into the second model. Since only the nodal displacements were imported into the second model, it had the geometry of the imperfection but no initial stress. The bending and buckling behavior of the imperfect longeron was then computed in the second model by applying the boundary conditions and using the arc-length solver as described in the previous sections.

In the first model's imperfection region, the displacement boundary condition was defined by a displacement field applied normal to the flange and described by a shape function, which approximated the shape of the imperfections observed experimentally. The shape function describing the bump imperfection was created in circumferential coordinates, where the radial displacement, Δr, was a function of the axial, z, and circumferential, θ, coordinates. The function was defined by a single period of a cosine wave surface in both the z and θ directions:

$$\Delta r(z,\theta) = 0.25A\left(\cos\left(\frac{2\pi(z-C_z)}{L_z}\right)+1\right)\left(\cos\left(\frac{2\pi R(\theta-C_\theta)}{L_\theta}\right)+1\right)$$
$$\text{for } z \in \left[C_z-\frac{L_z}{2}, C_z+\frac{L_z}{2}\right] \text{ and } \theta \in \left[C_\theta-\frac{L_\theta}{2R}, C_\theta+\frac{L_\theta}{2R}\right], \text{ with } \Delta r = 0 \text{ otherwise} \tag{5.1}$$

where A is the imperfection amplitude, C_z and C_θ are the coordinates of the center of the imperfection, L_z is the length of the imperfection in the z-direction, L_θ is the arc length in the θ-direction, and R is the flange radius.

The bump imperfection was axially centered on the longeron for all lengths, so $C_z = \frac{L}{2}$, and circumferentially centered on the edge of the flange, $C_\theta = \frac{2\pi}{3}$ rad, since it was shown in Chapter 3 that edge imperfections had the greatest effect on stability. The imperfection amplitude was $A = 0.5$ mm, the axial length of the imperfection was $L_z = 100$ mm and the circumferential arc length was $L_\theta = 20$ mm, which are approximately the mean values of these parameters for the imperfections measured in the experimental longerons, in Chapter 2. Since the bump was centered on the edge of the flange, it had a semi-elliptical footprint with only half its circumferential length actually on the flange, so the arc length of the bump that was on the flange was $\frac{L_\theta}{2} = 10$ mm.

5.3 Results

The behavior of both perfect and imperfect longerons loaded in pure bending with length varying from $L = 0.5$ m to $L = 5$ m was studied numerically using the methods described in Section 5.2. The bending moment-rotation curves for perfect longerons with varying length are shown in Fig. 5.2a. The general shape of these curves is similar for all lengths, in that the curves are all linear before the first bifurcation (which is denoted by the first local maximum in the bending moment). This is expected since the longerons behave linear elastically below the critical buckling load. Then, the longeron buckles and the bending moment decreases sharply, closely following the initial loading curve for all lengths. After decreasing to a local minimum, the longeron restabilizes and the moment and rotation increase again following a post-buckling path with lower bending stiffness than the initial loading curve, in all cases. Finally, a second bifurcation is reached (denoted by the second local maximum in the moment), after which the longerons cannot regain stability and the simulations can no longer converge.

One difference between the curves for different lengths is that the bending stiffness of the longerons decreases significantly with increasing length. This is expected since longer structures are more compliant. Another difference is that for shorter longerons, the critical buckling bending moment at the second bifurcation is greater than the critical moment at the first bifurcation, while for longerons longer than 2 m, the critical moment at the second bifurcation is less than that at the first bifurcation. This is an important difference since it means that buckling degrades the load carrying capacity of longer longerons more than shorter longerons, which can support moments significantly greater than the first critical moment in their post-buckling regime. Therefore, the stable post-buckling regime, which had been noted as a region where the shorter longerons could potentially be designed to operate, is not a good option for longer longerons.

Figure 5.2b shows the bending moment-rotation curves for imperfect longerons with varying length and a bump imperfection created using the method described in Section 5.2. The behavior of these imperfect longerons is expected to be similar to that of experimental longerons which have manufacturing imperfections. At all lengths, the curves for the imperfect longerons lack an initial linear region, and instead, closely follow the post-buckling path of the perfect longeron with the same respective length. This is because the imperfection decreases the first critical buckling load so much that a first bifurcation does not occur and the imperfect longeron immediately follows the perfect longeron's post-buckling path, as has been seen several times in literature for large amplitude imperfections [8, 9, 39, 44].

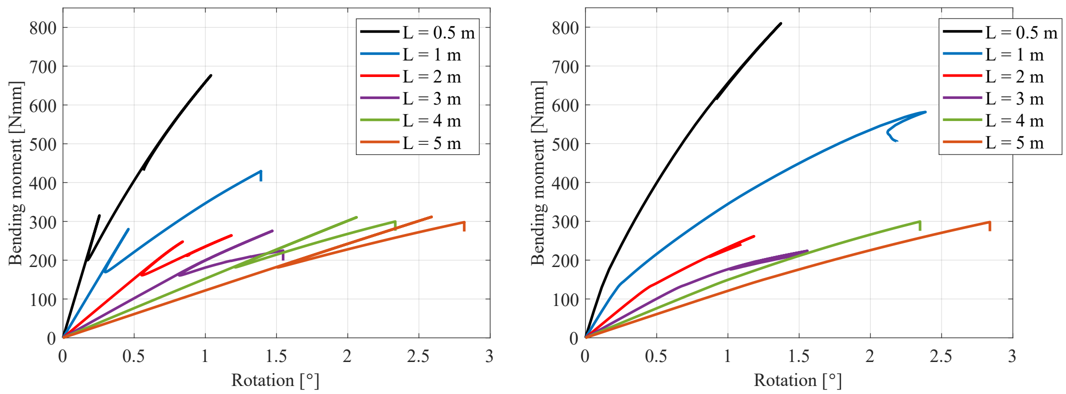

(a) Perfect longerons (b) Longerons with bump imperfection

Figure 5.2: Bending moment-rotation curves for perfect and imperfect longerons with varying length.

Interestingly, for the shortest 0.5 m and 1 m long longerons, the imperfect longerons have a higher second critical buckling moment than the perfect longerons of the same length. However, for lengths of 2 m and greater, the imperfect longerons have about the same second critical buckling moment as the perfect longerons with the same respective length. This suggests that the imperfection has a stabilizing effect in the post-buckling regime for the shorter longerons, which disappears at longer lengths when the longerons are more compliant. Overall, these results show that although the imperfection causes the longerons to lose their initial linear region and first bifurcation, which results in a lower bending stiffness at small applied rotations, the imperfection has relatively little effect on the longerons' post-buckling behavior and second critical buckling moment.

The bending stiffness of the perfect longerons was measured in the initial linear region before the first bifurcation for each length and is plotted as a function of length in Fig. 5.3a and listed in Table 5.1. As seen in Fig. 5.3a, the bending stiffness has an excellent fit to the function: $K = a\frac{1}{L}$ where K is the bending stiffness, L is the longeron length, and a is a fit parameter with a value of $a = 614,300$ Nmm^2/°. This fit has an R^2 value of 0.999, indicating that the fit is nearly perfect. The bending stiffness for linear elastic beams is $K = \frac{EI}{L}$, so it makes sense that this standard relation applies to longerons in their linear elastic regime as well. The imperfect longerons lack an initial linear region, making it difficult to quantify their bending stiffness. However, when comparing Fig. 5.2a and 5.2b, the imperfect longerons show the same qualitative trend of decreasing bending stiffness with increasing length that is seen for the perfect longerons.

The first and second critical buckling bending moments for the perfect longerons, as well as the second critical moments for the imperfect longerons, are plotted as a function of length in Fig. 5.3b and listed in Table 5.1. For the perfect longerons, the first critical moment (blue curve in Fig. 5.3b) decreases with increasing length, reaches a local minimum at $L = 2$ m, and then increases and remains fairly constant for lengths of 4 m and 5 m. However, in general, the variation in the first critical moment is quite small and it remains fairly constant at all lengths. The second critical moment for the perfect longerons (orange curve in Fig. 5.3b) decreases significantly with increasing length at shorter lengths, until it reaches a minimum at $L = 3$ m, after which the critical moment remains fairly constant for longer lengths. For the longerons with a bump imperfection, the second critical moment (green curve in Fig. 5.3b) follows the same trend with increasing length as the perfect longerons' second critical moment. This shows that the longerons' imperfection sensitivity is not affected by its length.

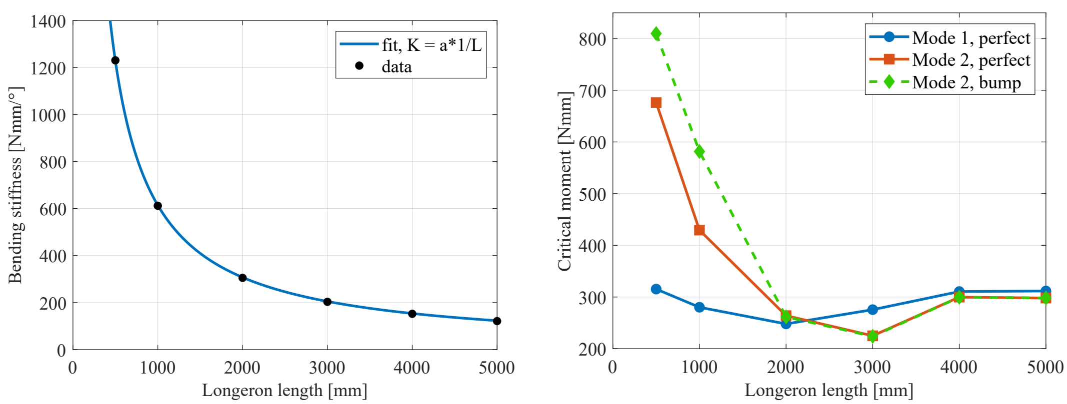

(a) (b)

Figure 5.3: (a) Bending stiffness of perfect longerons as a function of length.
(b) Critical buckling moments as a function of longeron length for both perfect and imperfect longerons.

The buckled shapes after the first bifurcation of the perfect longerons with varying length are shown in Fig. 5.4. For the shortest 0.5 m long longeron, a small local buckle formed near the center of the longeron after the first bifurcation. When the length was increased to $L = 1$ m, the amplitude and length of the buckle increased. At a length of 2 m, the buckled shape was global, with the buckle spanning more than half the length of the longeron. There was also significant axial twist in the

Table 5.1: Bending Stiffness and Critical Buckling Moments of Perfect and Imperfect Longerons with Varying Length

	Perfect			Bump
Length [m]	Stiffness [Nmm/°]	1st Crit. Moment [Nmm]	2nd Crit. Moment [Nmm]	2nd Crit. Moment [Nmm]
0.5	1231	315	676	810
1	612	280	429	582
2	305	248	264	261
3	203	275	225	224
4	152	311	300	299
5	121	312	298	298

longeron's center region, which caused the flange in compression to rotate up and the flange in tension to rotate down. This transition from a local buckle to a global buckle with axial twist that occurs at $L = 2$ m suggests that there is interaction between local and global buckling modes, and may be why the 2 m long longeron had the lowest first critical moment. For the longer longerons, the buckled shape remained global and the axial twist increased with increasing length, with the 4 m long longeron having the greatest magnitude twist. Interestingly, the twist decreased for the 5 m long longeron, which had about the same magnitude twist as the 2 m long longeron.

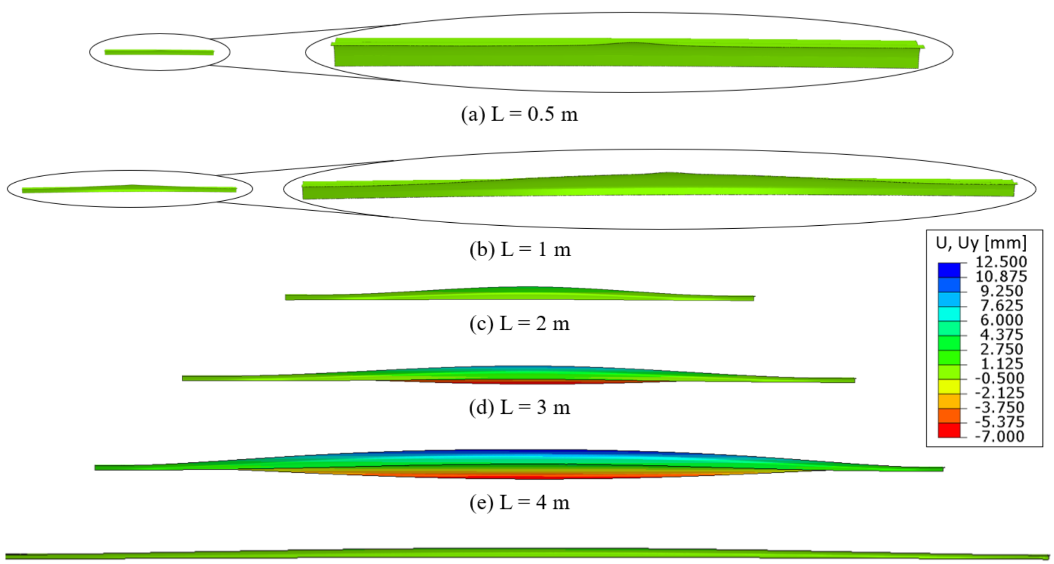

(a) L = 0.5 m

(b) L = 1 m

(c) L = 2 m

(d) L = 3 m

(e) L = 4 m

(f) L = 5 m

Figure 5.4: Comparison of the buckled shapes after the 1st bifurcation for perfect longerons with varying length. The deformation is magnified 25x, and the color scale shows vertical displacement. The lengths are to scale relative to each other, except for selected enlargements for the shortest longerons.

The buckled shapes of the perfect longerons after the second bifurcation, shown in Fig.5.5, are about the same for all lengths, with a large amplitude buckle near the center of the longeron. For the shorter 0.5 m and 1 m long longerons, the buckle that formed after the first bifurcation simply grew until it reached a maximum amplitude after the second bifurcation, with the 1 m long longeron having the largest amplitude buckle. At a length of 2 m, the axial twist seen after the first bifurcation disappeared in the post-buckling regime and the buckle localized, resulting in a large amplitude local buckle with no twist after the second bifurcation. For the longer 3 to 5 m longerons, the twist seen after the first bifurcation disappeared and the buckle localized in the post-buckling regime, similar to the 2 m longeron. Then, after the second bifurcation, the amplitude of the buckle increased and axial twist formed in the central region of the longeron in the opposite sense of the twist seen after the first bifurcation, i.e the flange in compression rotated down and the flange in tension rotated up. The magnitude of the twist after the second bifurcation increased with increasing longeron length, while the amplitude of the vertical buckle decreased with increasing length, with the 5 m longeron having the greatest magnitude twist and the smallest amplitude vertical buckle. Since this twist first occurred at a length of 3 m, interaction between the large amplitude vertical buckle and the axial twist could be why the 3 m long longeron has the lowest second critical moment. The shapes after the second bifurcation for the longerons with the bump imperfection are very similar to those of the perfect longerons at all lengths and are thus not shown.

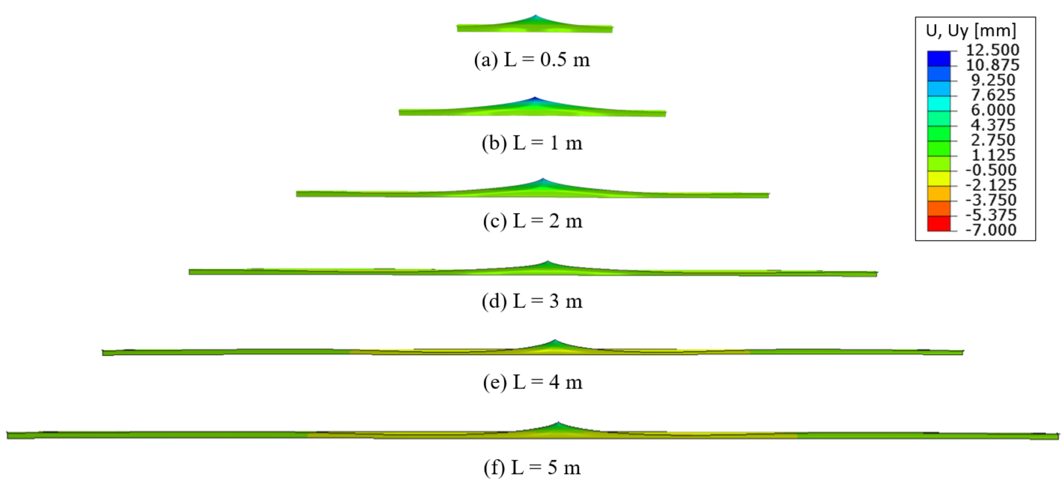

(a) L = 0.5 m

(b) L = 1 m

(c) L = 2 m

(d) L = 3 m

(e) L = 4 m

(f) L = 5 m

Figure 5.5: Comparison of the buckled shapes after the 2nd bifurcation for perfect longerons with varying length. The deformation is magnified 5x, and the color scale shows vertical displacement.

5.4 Discussion and Comparison to Literature

The critical buckling moment results in the present study can readily be compared to those in Leclerc and Pellegrino [38] for bending about the y-axis, since both study a single longeron loaded in pure bending with the same boundary conditions. The linear and nonlinear buckling analyses performed by Leclerc and Pellegrino predict the longeron's first critical buckling moment, since results in the post-buckling regime are not obtained using this method. The present study included nonlinear geometry in the finite element analysis, which is more realistic since large deformations occur when the longeron is bent, even at relatively small moments well below the critical buckling moment. Thus, the plot of the first critical buckling moment for the perfect longeron as a function of length (blue curve in Fig. 5.3b) is comparable to the equivalent plot for nonlinear buckling and moment about the y-axis shown in Fig. 12c of Ref. [38].

The values of the first critical buckling moment are higher in the present results than in Ref. [38] due to the updated cross-sectional geometry and material properties used to model the longerons in the current work. However, the trend with length in the present results and Ref. [38] are quite similar. In both plots, the first critical buckling moment decreases and fluctuates somewhat for shorter longerons below 3 m long. Then, for lengths of 3 m and above, the critical moment remains fairly constant with increasing length. The agreement between these two works helps validate their results, produced using different numerical solvers, and shows that the longerons' first critical moment indeed remains constant with increasing length.

At lengths above 2 m, the plots of the second critical buckling moment as a function of length for both perfect and imperfect longerons (orange and green curves in Fig. 5.3b) follow a trend similar to that of the first critical moment and remain nearly constant with increasing length. This is an even more important result than the first critical moment remaining constant with length, since the second bifurcation is what leads to the longerons' buckling failure. Additionally, the imperfect longerons lack a first bifurcation and only have a second critical moment. This makes the second critical moment more meaningful because experimental longerons will realistically always have manufacturing imperfections, and thus, will likely lack a first bifurcation similar to the numerical imperfect longerons studied in this work. Therefore, the results for the imperfect longerons' second critical moment suggest that the critical moment for experimental longerons will also remain almost constant with increasing length.

5.5 Conclusion

This work numerically studied the bending and buckling behavior of composite longerons with length varying from 0.5 m to 5 m, establishing the foundation for future experimental studies of longer longerons. The arc-length solver in Abaqus was used to compute the longerons' complete equilibrium curves, from which the bending stiffness and critical buckling bending moments as a function of length were determined. The effect of length on the longeron's imperfection sensitivity was also studied by modeling longerons with a bump imperfection similar to the manufacturing imperfections measured in experimental longerons.

At all lengths, the perfect longerons restabilized in the post-buckling regime after the first bifurcation, and then buckling failure occurred after the second bifurcation. The bending stiffness of the perfect longerons decreased as a function of $\frac{1}{L}$ with increasing length, with a nearly perfect fit to the curve $K = (614,300 \text{ Nmm}^2/°)\frac{1}{L}$. This relationship could be used to predict the stiffness of even longer longerons, such as the 60 m long longerons proposed for the SSPP structures.

At longer lengths, the first critical buckling moment for the perfect longeron was shown to remain constant with increasing length, in agreement with the results in Leclerc and Pellegrino [38]. The second critical moment for both the perfect and imperfect longerons also remained almost constant with increasing length for longer longerons, though it was lower than the first critical moment. The agreement between the second critical moment for the perfect and imperfect longerons shows that length does not change the longeron's imperfection sensitivity. Additionally, the results for the imperfect longerons suggest that experimental longerons containing manufacturing imperfections will also have a fairly constant second critical moment with increasing length, which is promising for the future SSPP structures.

The buckled shape of the perfect longerons after the first bifurcation had a small local buckle for the shorter longerons. Then, for longer longerons, the buckled shape became global and had significant axial twist in the central portion of the longeron. This significant change in buckled shape suggests that there is interaction between the local and global buckling modes. The buckled shape after the second bifurcation had a large amplitude buckle near the center of the longeron at all lengths, though the longer longerons also had axial twist in the central region of the longeron. In future work, it would be interesting to further investigate the interaction between buckling modes after both bifurcations and its effect on the critical buckling moment at different lengths.

Chapter 6

CONCLUSION

6.1 Summary and Contributions

The primary objective of this thesis was to better understand the buckling behavior and imperfection sensitivity of open cross-section, ultra-thin composite shells, using longerons as a case study. To address this objective, this thesis performed detailed, quantitative measurements of the manufacturing imperfections present in composite longerons. Then, the effects of these imperfections on the longeron's buckling behavior and critical buckling load were investigated in numerical and experimental studies of longerons loaded in bending. The final portions of this work used the findings from the imperfection measurements and imperfection sensitivity studies to explore variations in the longeron cross-section that could improve its stability and study the effect of increasing the longeron's length. Beyond their application to the SSPP structures, the longerons studied in this work can also be used to support other space systems where low mass and small packaged volume are important considerations. It is the author's hope that this work will help inform the design of more stable deployable space structures, made using thin composite shells that inevitably contain initial imperfections.

Chapter 2 presented an analysis method for characterizing the geometric imperfections existing in thin-shell composite structures. The method was used to measure the imperfections of a total of eight longerons made using two different manufacturing processes, revealing the types of defects most commonly introduced during manufacturing. This method can be generalized to characterize the imperfections of other thin-shell structures that contain large imperfections, which make analyzing the shape measurement data challenging.

Global imperfections such as variations in the longerons' cross-sectional parameters and axial twist were measured for completeness, though local imperfections are more interesting with respect to stability. Significant local radial imperfections in the longerons' flanges were measured, and four types of imperfections were identified: bumps, dimples, ridges and valleys. The mean imperfection amplitude ranged from six to ten times the flange thickness and the mean length ranged from about 130 mm to 240 mm in the z-direction, and 18 mm to 21 mm in the θ-direction for bumps and dimples. Notably, all of the measured local imperfections were quite different from the wave-like eigenmode shapes that are often used to model imperfections. Additionally, the longerons manufactured using the two-cure process have fewer imperfections and smaller amplitude imperfections than the longerons made using the one-cure process, leading to the conclusion that the two-cure process produces higher quality longerons.

Chapter 3 presented a numerical and experimental characterization of the effects of imperfections on the buckling behavior of longerons loaded in pure bending. The numerical analysis studied a single dominant imperfection on the longeron's flange with varying parameters, modeled using a simple shape function that approximated the shape of the imperfections measured experimentally in Chapter 2. The perfect longeron restabilized in the post-buckling regime after the first bifurcation, while longerons with large amplitude imperfections lacked a first bifurcation and immediately followed the perfect longeron's post-buckling path, which had a lower bending stiffness than the initial loading curve. The effect of the four different types of imperfections found in the experimental longerons was investigated, and ridge and valley imperfections, which span the entire circumferential width of the flange, were found to have a more detrimental effect on the longeron's knockdown factor and bending stiffness than more localized bumps and dimples. Additionally, bump imperfections were shown to have a greater effect on the longeron's stability than dimple imperfections with the same amplitude and size, since bumps are in the direction in which the longerons naturally buckle.

The bending and buckling experiments tested longerons that had random manufacturing imperfections, which were measured using the method from Chapter 2. Both the experimental and numerical results showed that longerons with greater amplitude imperfections had a significantly lower knockdown factor and bending stiffness. This is consistent with the trend seen in the published literature for various different thin-shell structures [8, 9, 15, 17, 18, 44]. However, unlike cylinders and spheres, open cross-section shells have an unsupported free edge, and in both experiments and simulations all buckles formed on the edge of the flange, regardless of the imperfections. Furthermore, the numerical study showed that imperfections on the edge of the flanges are more detrimental than imperfections in the center of the flanges.

In the last part of Chapter 3, excellent agreement was achieved when comparing the experimental and numerical results for a particular two-cure longeron, which had only one dominant imperfection with moderate amplitude on each flange. However, results showed that when multiple large amplitude imperfections are present, the method of modeling the imperfections with simplified shape functions breaks down and a high fidelity model must be used. Based on the measurements of larger amplitude and more frequent imperfections in the one-cure longerons shown in Chapter 2 and the detrimental effect of these imperfections shown in Chapter 3, it has been decided that the higher quality two-cure manufacturing process will be the preferred choice for making future longerons. Therefore, the numerical model, which was validated for the two-cure longeron, can reliably be used in future studies to predict the longerons' knockdown factor. These studies can focus on ridge and valley imperfections and large amplitude bumps which were found to be the most detrimental to the longeron's stability. Accurate predictions of the knockdown factor will enable the design of structures using longerons that avoid buckling failure, while minimizing their mass by avoiding over-designing.

Chapter 4 studied the effect of varying the cross-sectional geometry of longerons loaded in bending on their critical buckling load, imperfection sensitivity and bending stiffness. Since the edges of the flanges were shown to be the most susceptible to buckling, variations to the longeron cross-section focused on changing the location of the edge. A numerical analysis was performed to measure the bending and buckling behavior of both perfect and imperfect longerons with a wide range of varying flange subtended angles. The numerical analysis was complemented by experimental bending and buckling tests of longerons with three different flange subtended angles. Both the experimental and numerical results showed that the longeron's bending stiffness and critical buckling moment increase significantly with increasing flange subtended angle. Therefore, the optimal subtended angle is the maximum angle where the longeron does not exceed the mass limit for a given application or the limit of strain where the longeron can still be flattened and coiled without damage. Then, based on the promising results of increasing the flange subtended angle, the radius at the edge of the flange was decreased, which was shown to provide significant improvements in the longeron's stability and imperfection sensitivity without increasing its mass. Informed by the results of this study, the flange subtended angle of the longerons used in the SSPP structures was increased from 105° to 120° to increase their stability and bending stiffness. This is a good example of how a better understanding of a structure's buckling behavior can be used to inform the design of space structures with improved stability.

In Chapter 5, the complete equilibrium curves of longerons loaded in bending with length varying from 0.5 m to 5 m was numerically modeled. At all lengths, the perfect longerons were shown to restabilize in the post-buckling regime after the first bifurcation, and then buckling failure occurred after the second bifurcation, as was seen in Chapter 3 for the 0.5 m long longeron. The bending stiffness of the perfect longerons was shown to decrease as a function of $\frac{1}{L}$ with increasing length. This relationship could be used to predict the stiffness of even longer longerons, such as the 60 m long longerons proposed for the SSPP structures. At longer lengths, the first critical buckling moment for the perfect longeron was shown to remain constant with increasing length, in agreement with the results in Leclerc and Pellegrino [38]. The effect of length on the longeron's imperfection sensitivity was also studied by modeling longerons with a bump imperfection approximating the shape of the imperfections experimentally measured in Chapter 2. The second critical moment for both the perfect and imperfect longerons also remained almost constant with increasing length for longer longerons. The agreement between the second critical moment for the perfect and imperfect longerons shows that the longeron's imperfection sensitivity does not change with length. Additionally, the results for the imperfect longerons suggest that experimental longerons containing manufacturing imperfections will also have about the same stability at longer lengths. This work establishes the foundation for future experimental studies of longer longerons to validate the numerical results. Furthermore, these results are promising for future SSPP structures and other large space structures designed using longerons.

6.2 Future Research Directions

This section identifies several next steps in this research to reduce the manufacturing imperfections, improve the stability and imperfection sensitivity, and more fully understand the buckling behavior of open cross-section composite structures.

To address the significant manufacturing imperfections measured in the composite longerons in Chapter 2, one direction for future work is to experiment with using composite molds instead of the aluminum molds that are currently used to manufacture the longerons. It is suspected that thermal expansion mismatch between the laminate and metal mold during curing introduces stresses that are one cause of the local imperfections, and using composite molds that have a lower coefficient of thermal expansion would mitigate this issue. To confirm this hypothesis, the imperfections in longerons manufactured using composite molds could be measured and compared to the results presented in Chapter 2.

A single example of a decreased radius at the edge of the longeron's flanges was presented in Chapter 4. However, many other combinations of the flange subtended angle and the amount by which to decrease the radius at the edge of the flange are possible. Future work includes performing an optimization study to find the optimal subtended angles of both the original constant radius flange and the smaller radius arc, as well as the optimal radius of the smaller arc, that maximizes the longeron's stability and resistance to imperfections while minimizing its mass and making sure that it can still be flattened and coiled. This is important because the longerons will inevitably contain geometric imperfections, which significantly decrease the stability of the longerons with the current design, as has been shown in this work. Therefore, modifying the longerons' cross section is necessary to make them reliably stable despite the imperfections. As an alternative to optimization, if the critical buckling load and stiffness required for a particular application are known, then the flange subtended angle and amount by which to decrease the radius at the edge of the flange could be chosen accordingly to provide sufficient stability and stiffness. In either case, once a few promising cross-sectional geometries have been identified, the bending and buckling behavior of longerons with those geometries can be experimentally measured, and the ability of the longerons to be flattened and coiled can be experimentally verified. Another interesting modification to the current longeron design could be to slightly increase the thickness of the composite laminate at the edge of the flanges. This would reinforce the edges, which are the most prone to buckling, without affecting the ability of the flanges to be flattened.

Another avenue of future work includes continuing the work presented in Chapter 5 by experimentally studying the stability of longerons with varying length. Currently, bending and buckling experiments have only been performed on longerons less than 1 m long. It would be very interesting to see if the critical moment remains constant with increasing length as it does in the numerical results. It would also be interesting to see if the axial twist seen in the numerical buckled shapes exists experimentally as well. Once the numerical results are validated, longerons longer than 5 m can be modeled and a relationship between the longeron length and critical buckling moment can be found and extrapolated to significantly longer longerons, including the 60 m long longerons planned for use in the SSPP structures. A potential issue that may need to be considered at these extremely long lengths is the interaction between shell and column buckling, which could be very interesting to investigate.

Lastly, the work presented in this thesis to understand the buckling behavior of a single longeron can be extended to study the stability and imperfection sensitivity of the ladder-type strips that form the SSPP structure. Eventually this work can also be extended to a quadrant of the SSPP structure, which is currently formed by eight longerons with different lengths. It will interesting to study the buckling behavior of these more complex structures and to see how the rest of the structure reacts when one of the longerons buckles. Another interesting direction for future work is to study the effect that other elements in the SSPP structure attached to the longerons, such as hinges between the strips that are used to control the structure's deployment, might have on the longerons' buckling behavior. By expanding the understanding of the behavior of a single longeron, the present research has laid the foundation for such studies of more complex structures.

BIBLIOGRAPHY

[1] Hutchinson, J. W., and Koiter, W. T., "Postbuckling Theory," *Applied Mechanics Reviews*, Vol. 23, 1970, pp. 1353–1366.

[2] Brush, D. O., and Almroth, B. O., *Buckling of Bars, Plates, and Shells*, McGraw-Hill, New York, 1975.

[3] Teng, J. G., "Buckling of Thin Shells: Recent Advances and Trends," *Applied Mechanics Reviews*, Vol. 49, No. 4, 1996, pp. 263–274. https://doi.org/10.1115/1.3101927.

[4] Singer, J., Arbocz, J., and Weller, T., *Buckling Experiments: Experimental Methods in Buckling of Thin-Walled Structures*, Vol. 2, John Wiley and Sons, Inc., New York, 2002.

[5] Bushnell, D., "Shell Buckling," 2026. URL https://shellbuckling.com/index.php.

[6] Von Karman, T., and Tsien, H. S., "The Buckling of Thin Cylindrical Shells Under Axial Compression," *Journal of the Aeronautical Sciences*, Vol. 8, No. 8, 1941, pp. 303–312. https://doi.org/10.2514/8.10722.

[7] Koiter, W. T., *On the Stability of Elastic Equilibrium*, H. J. Paris, Amsterdam, Holland, 1945, Chap. 8, pp. 201–213.

[8] Donnell, L. H., and Wan, C. C., "Effect of Imperfections on Buckling of Thin Cylinders and Columns Under Axial Compression," *Journal of Applied Mechanics*, Vol. 17, No. 1, 1950, pp. 73–83. https://doi.org/10.1115/1.4010060.

[9] van der Neut, A., "The Interaction of Local Buckling and Column Failure of Thin-Walled Compression Members," *Applied Mechanics. International Union of Theoretical and Applied Mechanics*, edited by M. Hetényi and W. G. Vincenti, Springer-Verlag, Berlin, Heidelberg, 1969, pp. 389–399. https://doi.org/10.1007/978-3-642-85640-2_31.

[10] Babcock, C. D., "The Buckling of Cylindrical Shells with an Initial Imperfection Under Axial Compression Loading," Ph.D. thesis, Caltech, 1962.

[11] Arbocz, J., and Babcock, C. D., "The Effect of General Imperfections on the Buckling of Cylindrical Shells," *Journal of Applied Mechanics*, Vol. 36, No. 1, 1969, pp. 28–38. https://doi.org/10.1115/1.3564582.

[12] Hilburger, M. W., "Buckling of Thin-Walled Circular Cylinders," NASA/SP-8007-2020/REV 2, NASA Langley Research Center, Hampton, VA, 2020.

[13] Weingarten, V. I., Seide, P., and Peterson, J. P., "Buckling of Thin-Walled Circular Cylinders," NASA Space Vehicle Design Criteria, NASA SP-8007, 1968.

[14] Babcock, C. D., "Experiments in Shell Buckling," *Thin-Shell Structures: Theory, Experiment, and Design*, edited by Y. C. Fung and E. E. Sechler, Englewood Cliffs, New Jersey: Prentice-Hall, 1974, pp. 345–369.

[15] Gerasimidis, S., Virot, E., Hutchinson, J. W., and Rubinstein, S. M., "On Establishing Buckling Knockdowns for Imperfection-Sensitive Shell Structures," *Journal of Applied Mechanics*, Vol. 85, 2018. https://doi.org/10.1115/1.4040455.

[16] Fan, H., "Critical Buckling Load Prediction of Axially Compressed Cylindrical Shell Based on Non-Destructive Probing Method," *Journal of Thin-Walled Structures*, Vol. 139, 2019, pp. 91–104. https://doi.org/10.1016/j.tws.2019.02.034.

[17] Lee, A., Jimenez, F. L., Marthelot, J., Hutchinson, J. W., and Reis, P. M., "The Geometric Role of Precisely Engineered Imperfections on the Critical Buckling Load of Spherical Elastic Shells," *Journal of Applied Mechanics*, Vol. 83, No. 11, 2016. https://doi.org/10.1115/1.4034431.

[18] Abbasi, A., Derveni, F., and Reis, P. M., "Comparing the Buckling Strength of Spherical Shells With Dimpled Versus Bumpy Defects," *Journal of Applied Mechanics*, Vol. 90, No. 6, 2023. https://doi.org/10.1115/1.4056801.

[19] Derveni, F., Gueissaz, W., Yan, D., and Reis, P. M., "Probabilistic Buckling of Imperfect Hemispherical Shells Containing a Distribution of Defects," *Philosophical Transactions of the Royal Society A*, Vol. 381, 2023. https://doi.org/10.1098/rsta.2022.0298.

[20] Bowman, A., "Deployable Composite Booms (DCB)," *NASA*, 2023. URL https://www.nasa.gov/centers-and-facilities/langley/deployable-composite-booms-dcb.

[21] Leipold, M., Runge, H., and Sickinger, C., "Large SAR Membrane Antennas with Lightweight Deployable Booms," *28th ESA Antenna Workshop on Space Antenna Systems and Technologies, ESA/ESTEC*, 2005.

[22] Fernandez, J. M., "Advanced Deployable Shell-Based Composite Booms For Small Satellite Structural Applications Including Solar Sails," *International Symposium on Solar Sailing 2017*, 2017.

[23] Cox, K., and Medina, K., "Scalability of Triangular Rollable and Collapsible Booms," *AIAA SciTech 2019 Forum*, 2019. https://doi.org/10.2514/6.2019-2026.

[24] Stohlman, O. R., Zander, M. E., and Fernandez, J. M., "Characterization and Modeling of Large Collapsible Tubular Mast Booms," *AIAA SciTech 2021 Forum*, 2021. https://doi.org/10.2514/6.2021-0903.

[25] Arya, M., Hodges, R., Sauder, J. F., Horst, S., Mobrem, M., Pedivellano, A., Wen, A., Truong, A., and Pellegrino, S., "Lightweight Composite Reflectarray that can be Flattened, Folded, and Coiled for Compact Stowage," *AIAA SciTech 2022 Forum*, 2022. https://doi.org/10.2514/6.2022-1886.

[26] Nguyen, L., Medina, K., McConnel, Z., and Lake, M. S., "Solar Cruiser TRAC Boom Development," *AIAA SciTech 2023 Forum*, 2023. https://doi.org/10.2514/6.2023-1507.

[27] Banik, J., Kiefer, S., LaPointe, M., and LaCorte, P., "On-Orbit Validation of the Roll-Out Solar Array," *2018 IEEE Aerospace Conference*, 2018. https://doi.org/10.1109/AERO.2018.8396390.

[28] Patel, S., "Impact Story: Roll-Out Solar Arrays," *NASA*, 2024. URL https://www.nasa.gov/directorates/stmd/impact-story-roll-out-solar-arrays.

[29] Wilkie, W. K., Fernandez, J. M., Stohlman, O. R., Schneider, N. R., Dean, G. D., Kang, J. H., Warren, J. E., Cook, S. M., Brown, P. L., Denkins, T. C., Horner, S. D., Tapio, E. D., Straubel, M., Richter, M., and Heiligers, J., "Overview of the NASA Advanced Composite Solar Sail System (ACS3) Technology Demonstration Project," *AIAA SciTech 2021 Forum*, 2021. https://doi.org/10.2514/6.2021-1260.

[30] Bowman, A., and Figliozzi, G., "What is the Advanced Composite Solar Sail System?" *NASA*, 2026. URL https://www.nasa.gov/smallspacecraft/what-is-acs3.

[31] Arya, M., Lee, N., and Pellegrino, S., "Ultralight Structures for Space Solar Power Satellites," *AIAA SciTech 2016 Forum*, 2016. https://doi.org/10.2514/6.2016-1950.

[32] Banik, J. A., and Murphey, T. W., "Performance Validation of the Triangular Rollable and Collapsible Mast," *Proceedings of the 24th Annual AIAA/USU Conference on Small Satellites*, AIAA, Logan, UT, 2010.

[33] Murphey, T., and Banik, J., "Triangular Rollable and Collapsible Boom," *US Patent 7,895,795*, 2011.

[34] Gdoutos, E., Sommer, C. F., Truong, A., Wen, A., Pedivellano, A., Ubamanyu, K., Madonna, R., and Pellegrino, S., "Development of the Deployable On-Orbit Ultra-Light Composite Experiment (DOLCE) for the Space Solar Power Project Demonstration Mission," *AIAA SciTech 2022 Forum*, 2022. https://doi.org/10.2514/6.2022-1266.

[35] Sommer, C. F., Gdoutos, E., Truong, A., Wen, A., Sauder, J. F., Madonna, R., and Pellegrino, S., "On-Orbit Demonstration of the Deployable On-Orbit Ultra-Light Composite Experiment (DOLCE) on the Caltech Space Solar Power Demonstration 1 (SSPD-1) Mission," *AIAA SciTech 2025 Forum*, 2025. https://doi.org/10.2514/6.2025-1007.

[36] Royer, F., and Pellegrino, S., "Probing the Stability of Ladder-Type Coilable Space Structures," *AIAA Journal*, Vol. 60, No. 4, 2022, pp. 2000–2012. https://doi.org/10.2514/1.J060820.

[37] Murphey, T. W., Turse, D., and Adams, L., "TRAC Boom Structural Mechanics," *4th AIAA Spacecraft Structures Conference*, 2017. https://doi.org/10.2514/6.2017-0171.

[38] Leclerc, C., and Pellegrino, S., "Nonlinear Elastic Buckling of Ultra-Thin Coilable Booms," *International Journal of Solids and Structures*, Vol. 203, 2020, pp. 46–56. https://doi.org/10.1016/j.ijsolstr.2020.06.042.

[39] Leclerc, C., Wilson, L. L., Bessa, M. A., and Pellegrino, S., "Characterization of Ultra-Thin Composite Triangular Rollable and Collapsible Booms," *4th AIAA Spacecraft Structures Conference*, 2017. https://doi.org/10.2514/6.2017-0172.

[40] Fathi, A., and Royer, F., "The Effect of Localized Imperfection Geometry on Thin-Shell Buckling: Imperfection Width Controls Stability, Imperfection Direction Governs Spatial Sensitivity," *AIAA SciTech 2026 Forum*, 2026. https://doi.org/10.2514/6.2026-1044.

[41] Degenhardt, R., Bethge, A., Kling, A., Zimmermann, R., Rohwer, K., Klein, H., Tessmer, J., and Calvi, A., "Probabilistic Approach for Improved Buckling Knock-Down Factors of CFRP Cylindrical Shells," *Proceeding of 18th Engineering Mechanics Division Conference*, European Air and Space Conference, 2007.

[42] Royer, F., "Probing the Buckling of Thin-Shell Space Structures," Ph.D. thesis, Caltech, 2021.

[43] "fmincon," *The MathWorks, Inc., Matlab Help Center*, Accessed 4 November 2024. URL https://www.mathworks.com/help/optim/ug/fmincon.html?s_tid=doc_ta.

[44] Wullschleger, L., "Numerical Investigation of the Buckling Behaviour of Axially Compressed Circular Cylinders Having Parametric Initial Dimple Imperfections," Ph.D. thesis, ETH, Zurich, Switzerland, 2006.

[45] Royer, F., and Pellegrino, S., "Experimentally Probing the Stability of Thin-Shell Structures Under Pure Bending," *Philosophical Transactions of the Royal Society A*, Vol. 381, No. 2244, 2023. https://doi.org/10.1098/rsta.2022.0024.

[46] Reddy, N. H., "Folding and Dynamic Deployment of Ultralight Thin-Shell Space Structures," Ph.D. thesis, Caltech, 2023.

[47] Crisfield, M., "A Fast Incremental/Iterative Solution Procedure that Handles 'Snap-Through'," *Computers and Structures*, Vol. 13, No. 1, 1981, pp. 55–62. https://doi.org/10.1016/0045-7949(81)90108-5.

[48] Kechri, M., Mallikarachchi, H. M. Y. C., Sauder, J. F., and Pellegrino, S., "Design and Testing of an Elastically Foldable Flat Structure With Prestressed Diagonals," *AIAA SciTech 2026 Forum*, 2026. https://doi.org/10.2514/6.2026-1043.

[49] Bessa, M., and Pellegrino, S., "Design of Ultra-Thin Shell Structures in the Stochastic Post-Buckling Range Using Bayesian Machine Learning and Optimization," *International Journal of Solids and Structures*, Vol. 139-140, 2018, pp. 174–188. https://doi.org/10.1016/j.ijsolstr.2018.01.035.

[50] Leclerc, C., "Mechanics of Ultra-Thin Composite Coilable Structures," Ph.D. thesis, Caltech, 2020.

[51] Kosztowny, C. J. R., Mennu, M. M., Dean, G. D., and Larson, R. A., "Experimental Testing of a 30-meter Triangular, Rollable, and Collapsible Composite Deployable Boom," *AIAA SciTech 2026 Forum*, 2026. https://doi.org/10.2514/6.2026-1858.

Appendix A

SUPPLEMENTARY MATERIALS

A.1 Chapter 2: Detailed Results for Local Imperfection Measurements

This Appendix shows the full set of results from the local radial imperfection measurements described in Chapter 2. Figure A.1 shows the local radial deviations from the mean flange radius and Fig. A.2 shows the shape functions fitted to the flange data overlaid on the radial deviations for all flanges in both sets. Note that in Fig. A.1 and A.2, the color scale is different for Set 1 and Set 2. Tables A.1 and A.2 provide the fit parameters of the shape function in Eq. 2.3, and the R^2 value of the fit for the dominant imperfections of each flange in Set 1 and Set 2, respectively. Table A.3 lists the bounds of the windows that gave the best fit for the exceptions when the window size differed from λ_z by $\frac{\lambda_\theta}{2R}$ for bumps and dimples, and λ_z by θ_e for ridges and valleys. Finally, the amplitude and lengths of the dominant imperfections for each longeron in Set 1 and Set 2 are shown in Tables A.4 and A.5, respectively.

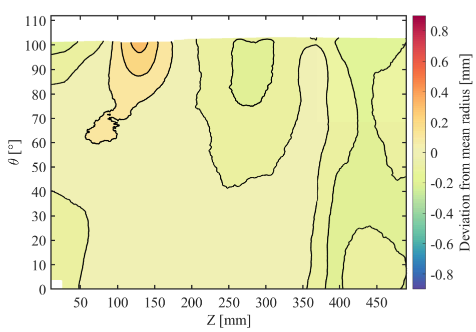

(a) Front flange, Set 1, α = 105°

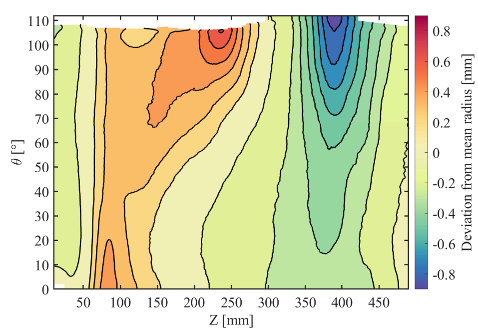

(b) Back flange, Set 1, α = 105°

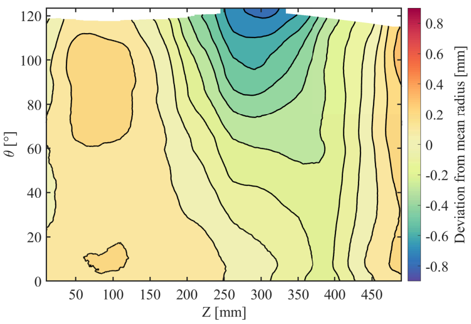

(c) Front flange, Set 1, $\alpha = 120°$

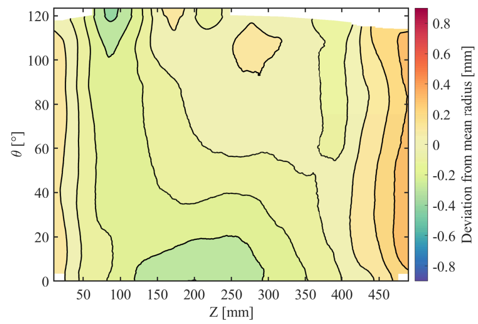

(d) Back flange, Set 1, $\alpha = 120°$

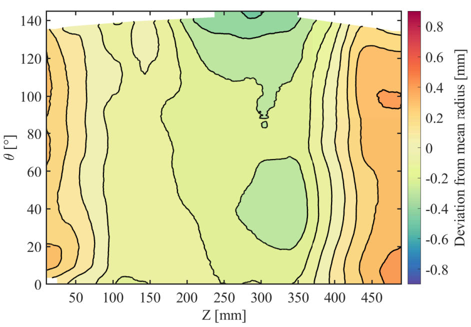

(e) Front flange, Set 1, $\alpha = 135°$

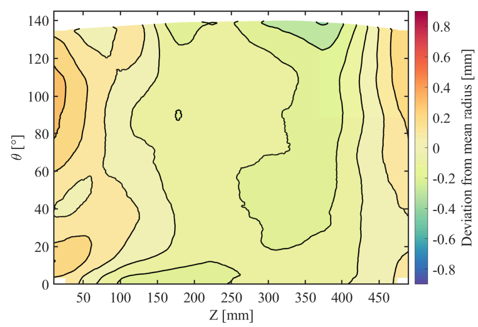

(f) Back flange, Set 1, $\alpha = 135°$

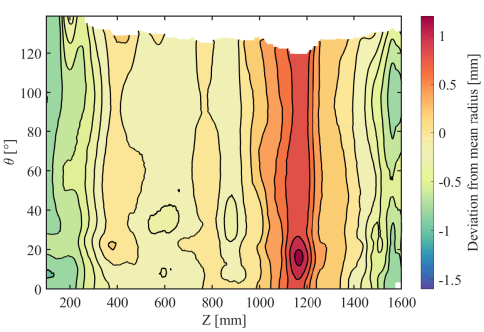

(g) Front flange, Set 2, Sample 1

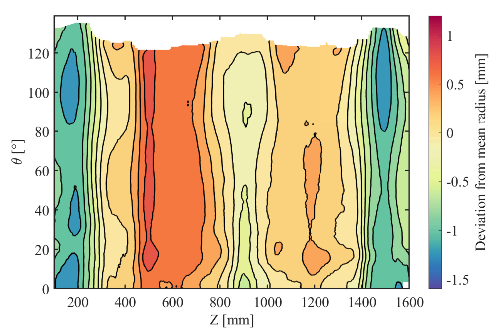

(h) Back flange, Set 2, Sample 1

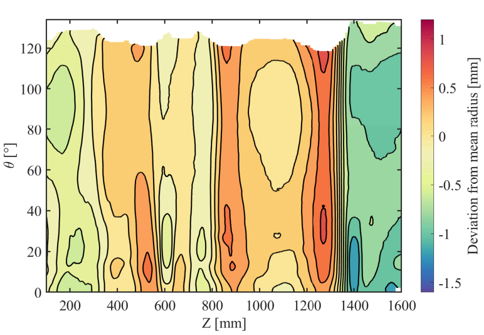

(i) Front flange, Set 2, Sample 2

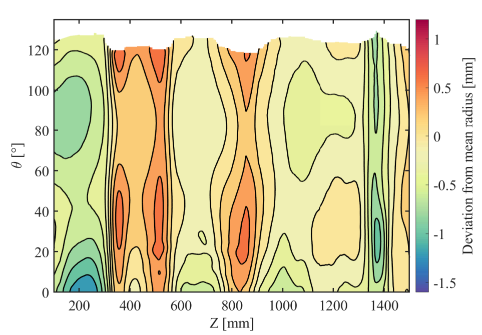

(j) Back flange, Set 2, Sample 2

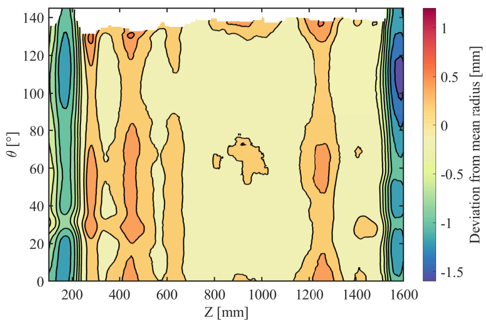

(k) Front flange, Set 2, Sample 3

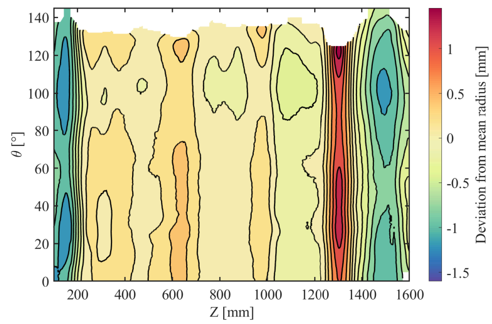

(l) Back flange, Set 2, Sample 3

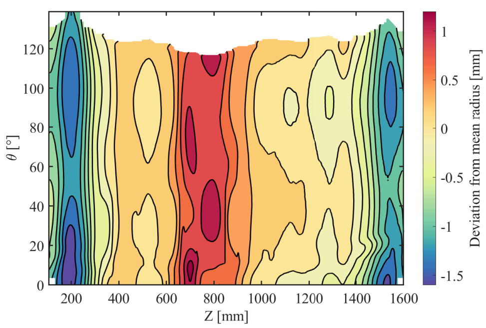

(m) Front flange, Set 2, Sample 4

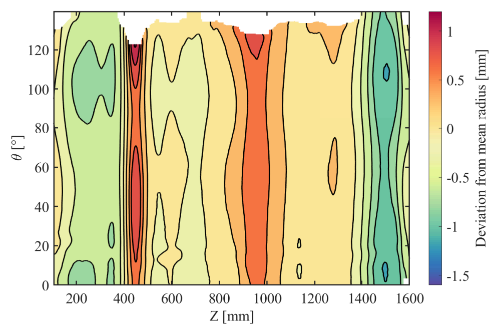

(n) Back flange, Set 2, Sample 4

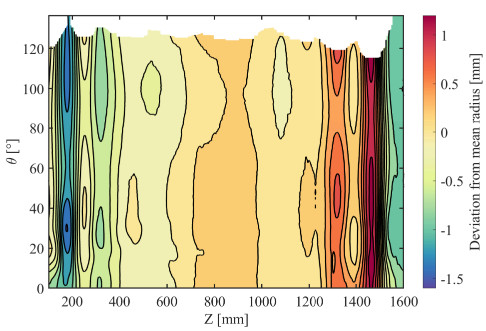

(o) Front flange, Set 2, Sample 5

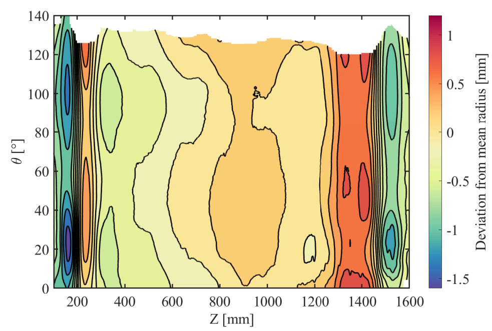

(p) Back flange, Set 2, Sample 5

Figure A.1: Local radial deviations from the mean flange radius. Positive deviations indicate outward imperfections (bumps or ridges) and negative deviations indicate inward imperfections (dimples or valleys).

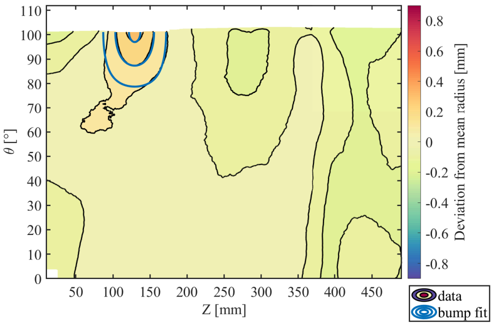

(a) Front flange, Set 1, α = 105°

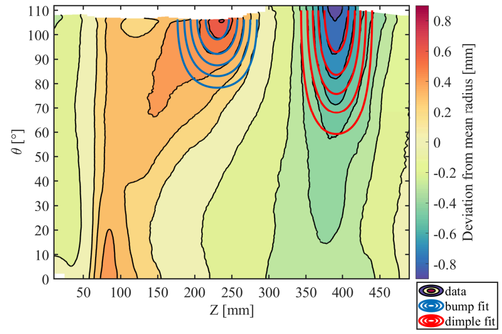

(b) Back flange, Set 1, α = 105°

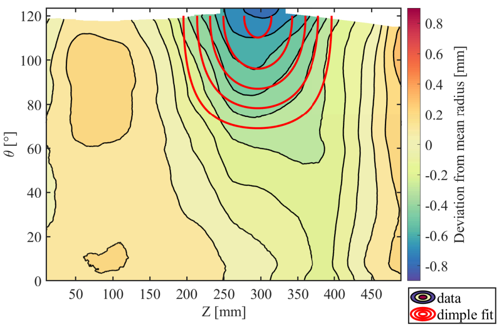

(c) Front flange, Set 1, α = 120°

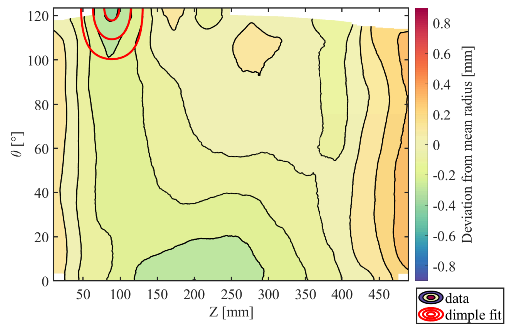

(d) Back flange, Set 1, α = 120°

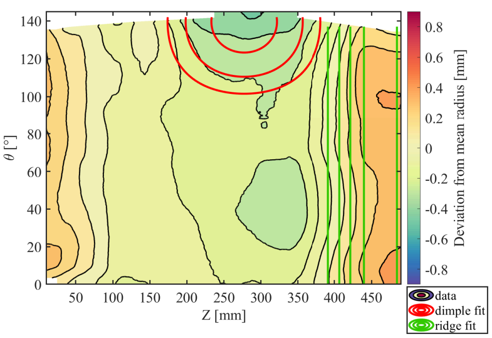

(e) Front flange, Set 1, α = 135°

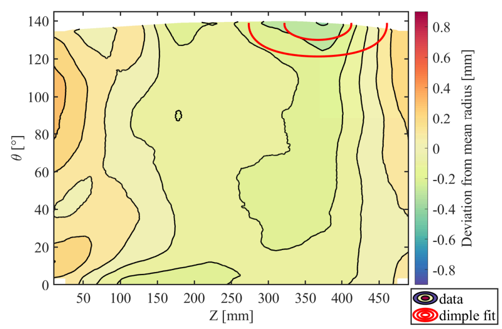

(f) Back flange, Set 1, α = 135°

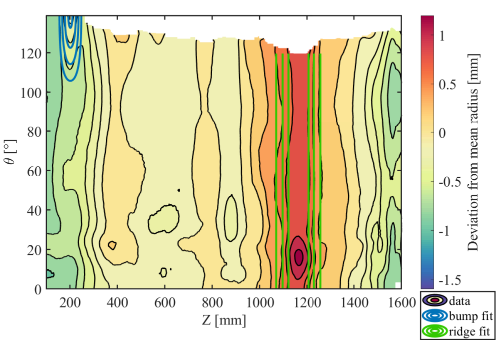

(g) Front flange, Set 2, Sample 1

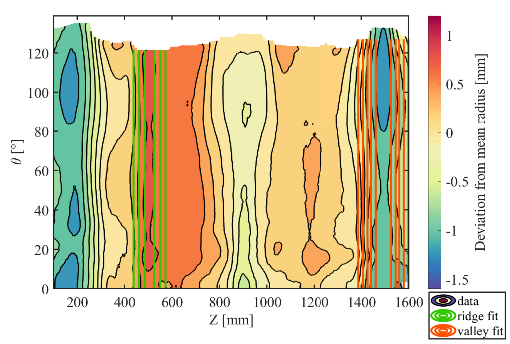

(h) Back flange, Set 2, Sample 1

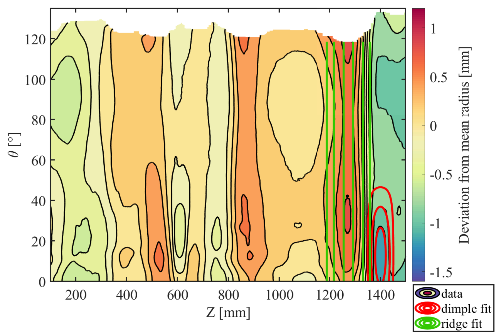

(i) Front flange, Set 2, Sample 2

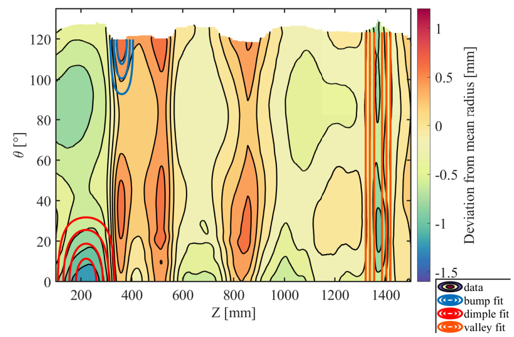

(j) Back flange, Set 2, Sample 2

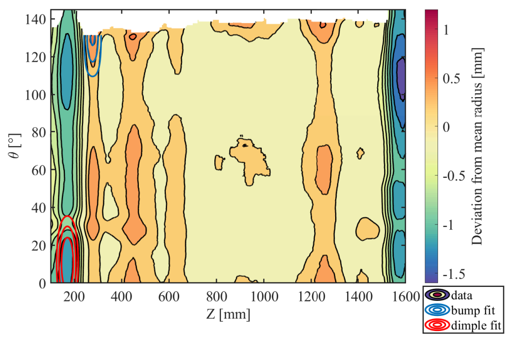

(k) Front flange, Set 2, Sample 3

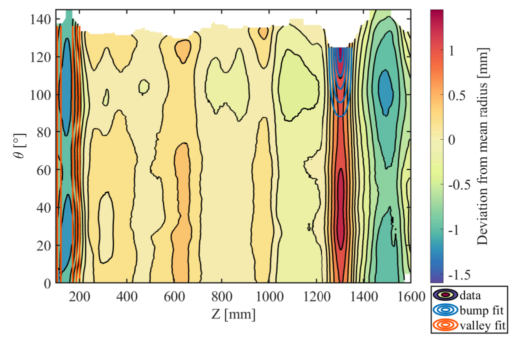

(l) Back flange, Set 2, Sample 3

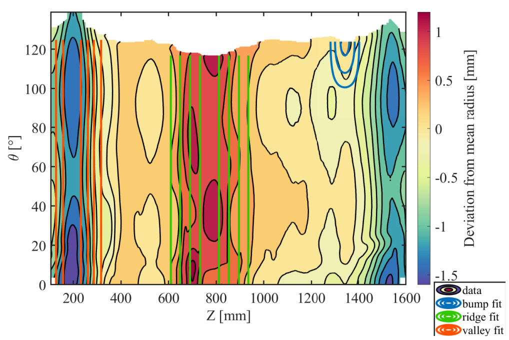

(m) Front flange, Set 2, Sample 4

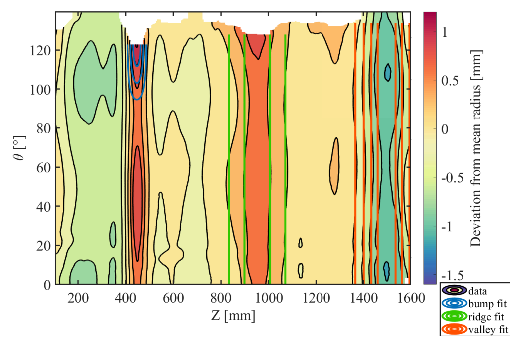

(n) Back flange, Set 2, Sample 4

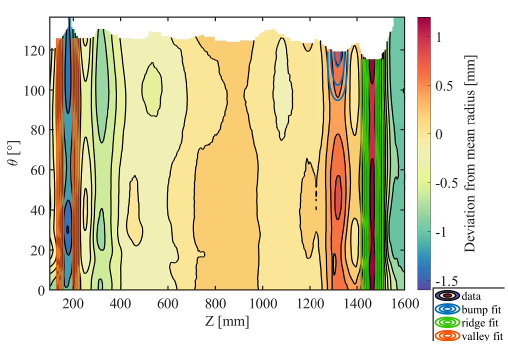

(o) Front flange, Set 2, Sample 5

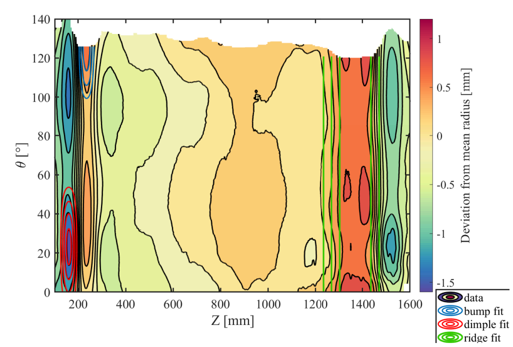

(p) Back flange, Set 2, Sample 5

Figure A.2: Shape functions fitted to the dominant imperfections for all flanges.

Table A.1: Parameters of Shape Functions for Dominant Imperfections for Set 1

Sample	Type	A [mm]	λ_z [mm]	λ_θ [mm]	b [mm]	C_z [mm]	C_θ [°]	R^2
Front flange, α = 105°	Bump	0.25	118.4	15.05	0.05	129.3	101.1	0.98
Back flange, α = 105°	Bump	0.60	159.3	19.40	0.05	230.3	106.3	0.99
	Dimple	0.58	132.7	32.41	-0.20	391.5	112.0	0.99
Front flange, α = 120°	Dimple	0.50	268.3	31.94	-0.15	295.7	123.5	0.94
Back flange, α = 120°	Dimple	0.28	120.9	15.88	-0.02	88.8	123.5	0.97
Front flange, α = 135°	Dimple	0.44	371.5	19.94	0.09	277.4	142.3	0.96
	Ridge	0.46	212.7	∞	-0.12	462.0	N/A	0.94
Back flange, α = 135°	Dimple	0.23	328.8	13.84	-0.03	367.1	139.3	0.91

Table A.2: Parameters of Shape Function for Dominant Imperfections for Set 2

Sample	Type	A [mm]	λ_z [mm]	λ_θ [mm]	b [mm]	C_z [mm]	C_θ [°]	R^2
Front flange, Sample 1	Bump	0.58	135.2	21.90	-0.78	201.7	139.0	0.99
	Ridge	0.66	247.2	∞	0.31	1,163.5	N/A	0.94
Back flange, Sample 1	Ridge	0.61	202.4	∞	0.22	504.9	N/A	0.96
	Valley	1.09	320.6	∞	0.08	1,492.9	N/A	0.93
Front flange, Sample 2	Dimple	0.49	115.7	17.71	-0.65	1,400.5	12.6	0.95
	Ridge	0.70	297.7	∞	0.13	1,274.2	N/A	0.93
Back flange, Sample 2	Bump	0.67	119.2	16.94	0.10	360.0	119.8	0.91
	Dimple	0.79	288.9	19.28	-0.35	219.7	0	0.93
	Valley	0.58	136.5	∞	-0.09	1,370.4	N/A	0.95
Front flange, Sample 3	Bump	0.53	98.7	12.58	0.11	277.3	131.4	0.98
	Dimple	1.04	160.0	18.69	-0.19	171.0	10.3	0.93
Back flange, Sample 3	Bump	1.44	137.8	22.80	0.08	1,301.9	124.9	0.99
	Valley	1.17	195.1	∞	0.14	146.8	N/A	0.95
Front flange, Sample 4	Bump	0.44	159.9	14.14	-0.18	1,343.0	123.9	0.91
	Ridge	0.66	328.0	∞	0.37	772.3	N/A	0.92
	Valley	1.20	315.2	∞	-0.06	194.24	N/A	0.95
Back flange, Sample 4	Bump	0.96	109.1	16.74	0.22	446.9	122.8	0.99
	Ridge	0.48	282.3	∞	0.27	952.7	N/A	0.95
	Valley	1.07	350.3	∞	0.15	1,498.3	N/A	0.97
Front flange, Sample 5	Bump	0.67	135.8	17.24	0.20	1,318.0	119.3	0.97
	Ridge	0.78	100.6	∞	0.42	1,462.0	N/A	0.92
	Valley	1.10	143.5	∞	-0.11	178.3	N/A	0.95
Back flange, Sample 5	Bump	0.86	105.2	19.86	-0.11	235.1	125.9	0.98
	Dimple	0.82	90.6	18.01	-0.68	160.1	23.2	0.97
	Ridge	0.83	422.4	∞	-0.04	1,269.4	N/A	0.91

Table A.3: Bounds of Windows with Highest R^2 Values

Set	Sample	Type	z_i [mm]	z_f [mm]	θ_i [°]	θ_f [°]
1	Front flange, $\alpha = 135°$	Dimple	174.0	381.0	101.6	145.0
		Ridge	355.7	490	0	136.0
	Back flange, $\alpha = 135°$	Dimple	255.0	460.5	109.4	139.3
2	Back flange, Sample 1	Valley	1,332.6	1,600	0	132.9
	Front flange, Sample 2	Dimple	1,342.7	1,458.3	0	51.2
	Back flange, Sample 2	Dimple	100	364.1	0	41.28
	Front flange, Sample 3	Dimple	100	251.0	0	54.6
	Back flange, Sample 3	Valley	100	244.35	0	145.0
	Front flange, Sample 4	Valley	100	351.8	0	139.0
	Back flange, Sample 4	Valley	1,323.1	1,600	0	139.0
	Back flange, Sample 5	Dimple	114.8	205.4	0	63.8
		Ridge	1,203.0	1,470.0	0	120.1

Table A.4: Amplitude and Length of Dominant Imperfections for Set 1

	Bump			**Dimple**			**Ridge**		**Valley**	
Sample	A [mm]	L_z [mm]	L_θ [mm]	A [mm]	L_z [mm]	L_θ [mm]	A [mm]	L_z [mm]	A [mm]	L_z [mm]
Front flange, $\alpha = 105°$	0.25	118.4	15.05	N/A	N/A	N/A	N/A	N/A	N/A	N/A
Back flange, $\alpha = 105°$	0.60	159.3	19.40	0.58	132.7	32.41	N/A	N/A	N/A	N/A
Front flange, $\alpha = 120°$	N/A	N/A	N/A	0.50	268.3	31.94	N/A	N/A	N/A	N/A
Back flange, $\alpha = 120°$	N/A	N/A	N/A	0.28	120.9	15.88	N/A	N/A	N/A	N/A
Front flange, $\alpha = 135°$	N/A	N/A	N/A	0.44	207.0	19.94	0.46	212.7	N/A	N/A
Back flange, $\alpha = 135°$	N/A	N/A	N/A	0.23	205.5	13.84	N/A	N/A	N/A	N/A
Set 1 Mean	0.43 ±0.25	138.9 ±28.9	17.22 ±1.54	0.41 ±0.15	186.9 ±60.6	22.80 ±4.42	0.46 ± 0	212.7 ± 0	N/A	N/A

Table A.5: Amplitude and Length of Dominant Imperfections for Set 2

	Bump			**Dimple**			**Ridge**		**Valley**	
Sample	A [mm]	L_z [mm]	L_θ [mm]	A [mm]	L_z [mm]	L_θ [mm]	A [mm]	L_z [mm]	A [mm]	L_z [mm]
Front flange, Sample 1	0.58	135.2	21.90	N/A	N/A	N/A	0.66	247.2	N/A	N/A
Back flange, Sample 1	N/A	N/A	N/A	N/A	N/A	N/A	0.61	202.4	1.09	320.6
Front flange, Sample 2	N/A	N/A	N/A	0.49	115.7	17.71	0.70	297.7	N/A	N/A
Back flange, Sample 2	0.67	119.2	16.94	0.79	288.9	19.28	N/A	N/A	0.58	136.5
Front flange, Sample 3	0.53	98.7	12.58	1.04	160.0	18.69	N/A	N/A	N/A	N/A
Back flange, Sample 3	1.44	137.8	22.80	N/A	N/A	N/A	N/A	N/A	1.17	195.1
Front flange, Sample 4	0.44	159.9	14.14	N/A	N/A	N/A	0.66	328.0	1.20	315.2
Back flange, Sample 4	0.96	109.1	16.74	N/A	N/A	N/A	0.48	282.3	1.07	350.3
Front flange, Sample 5	0.67	135.8	17.24	N/A	N/A	N/A	0.78	100.6	1.10	143.5
Back flange, Sample 5	0.86	105.2	19.86	0.82	90.6	18.01	0.83	267.0	N/A	N/A
Set 2 Mean	0.77 ±0.32	125.1 ±20.6	17.78 ±1.78	0.78 ±0.23	163.8 ±76.6	18.42 ±1.85	0.67 ±0.11	246.4 ±75.5	1.03 ±0.23	243.5 ±68.4
Overall Mean	0.70 ±0.33	127.9 ±21.4	17.67 ±1.66	0.58 ±0.26	176.6 ±65.7	20.85 ±3.33	0.65 ±0.13	242.2 ±80.4	1.03 ±0.23	243.5 ±68.4

A.2 Chapter 3: Additional Buckling Results

This Appendix shows additional buckling results obtained during the simulations and experiments of longerons loaded in pure bending, described in Chapter 3. Table A.6 lists the first critical buckling moments and rotations for numerical longerons that had a first bifurcation. Figure A.3 shows the buckled shapes of the experimental two-cure longeron after the second bifurcation, both when the front flange and when the back flange was in compression. Lastly, Fig. A.4 shows the buckled shapes of the experimental one-cure longerons after the second bifurcation.

Table A.6: Mode 1 Critical Moments and Rotations for Numerical Longerons

Imperfection Type	**Crit. Moment** [Nmm]	**Crit. Rotation** [°]	**Knockdown Factor**
Perfect	318	0.66	—
Bump, A = 0.01 mm	286	0.60	0.90
Dimple, A = 0.01 mm	321	0.67	1.01
Ridge, A = 0.01 mm	278	0.58	0.87
Valley, A = 0.01 mm	318	0.66	1.00
Dimple, A = 0.1 mm	215	0.45	0.68
Valley, L_z = 100 mm	219	0.47	0.69
Center bump	251	0.53	0.79

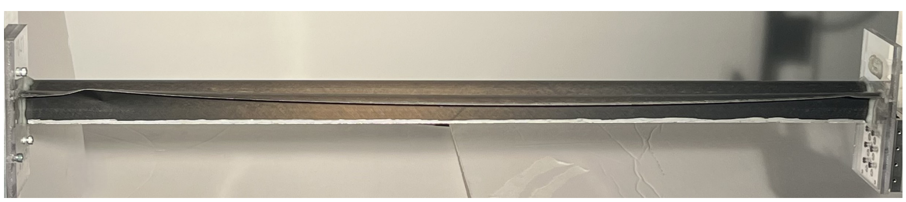

(a) Front flange in compression, two cures

(b) Back flange in compression, two cures

Figure A.3: Buckled shape of experimental two-cure longeron after 2nd bifurcation.

(a) Front flange in compression, Sample 1

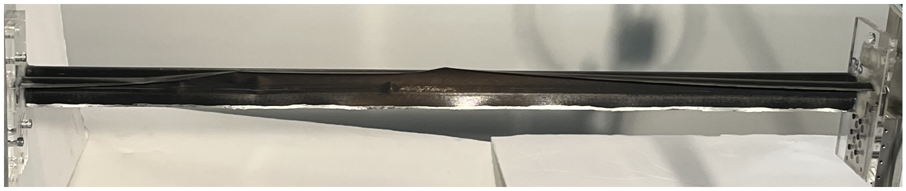

(b) Back flange in compression, Sample 1

(c) Front flange in compression, Sample 2

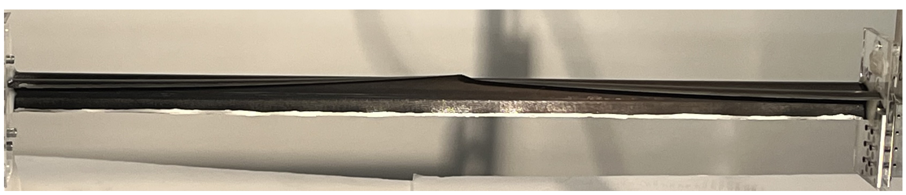

(d) Back flange in compression, Sample 2

(e) Front flange in compression, Sample 3

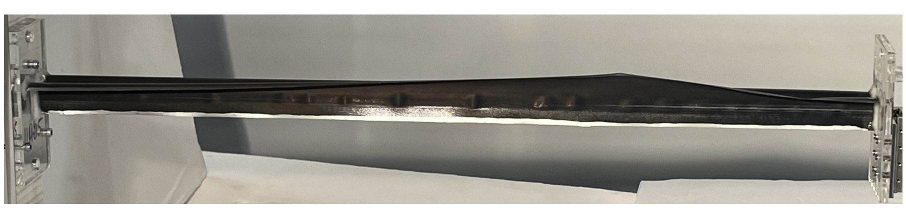

(f) Back flange in compression, Sample 3

Figure A.4: Buckled shape of experimental one-cure longerons after 2nd bifurcation.

A.3 Chapter 4: Detailed Experimental Results

Figure A.5 shows the bending moment-rotation curves for all trials for the experimental longerons with varying flange subtended angle, obtained using the procedure described in Chapter 4.

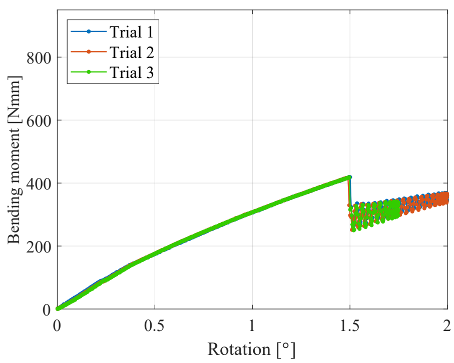

(a) Front flange in compression, $\alpha = 105°$

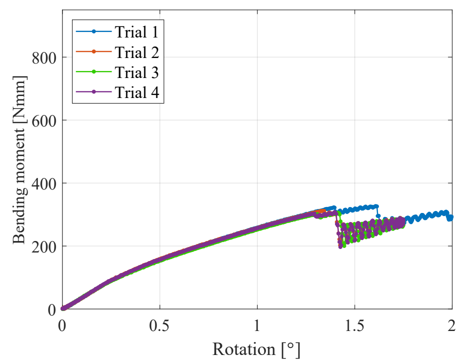

(b) Back flange in compression, $\alpha = 105°$

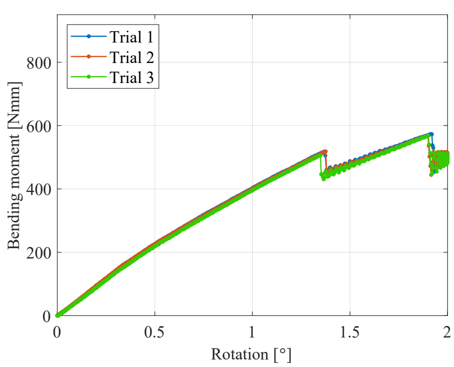

(c) Front flange in compression, $\alpha = 120°$

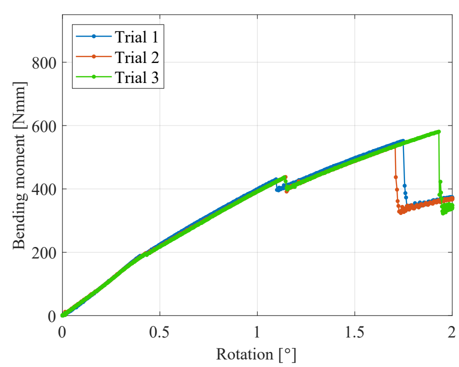

(d) Back flange in compression, $\alpha = 120°$

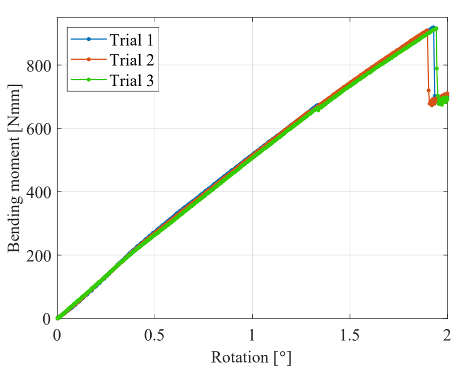

(e) Front flange in compression, $\alpha = 135°$

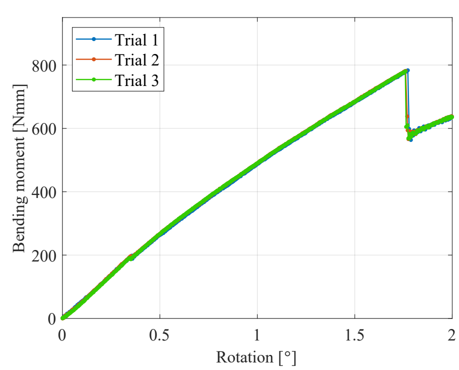

(f) Back flange in compression, $\alpha = 135°$

Figure A.5: Magnitude of bending moment-rotation curves for all trials for experimental longerons with varying flange subtended angle.